

# Phase-Resolved Ferromagnetic Resonance Studies of Thin Film Ferromagnets

Submitted by **Max Ken Marcham** to the University of Exeter as a thesis for the degree of Doctor of Philosophy in Physics, August 2012.

This thesis is available for library use on the understanding that it is copyright material and that no quotation from the thesis may be published without proper acknowledgement.

I certify that all material in this thesis which is not my own work has been identified and that no material has previously been submitted and approved for the award of a degree by this or any other university.



*To biggly*

## **Abstract**

Precessional dynamics are exploited in the operation of high frequency magnetic devices such as magnetic disk drives, non reciprocal microwave devices and spin transfer oscillators. The trajectory of the precession and its damping are of crucial importance. This thesis presents the characterisation of a variety of magnetic thin film structures performed with a range of phase sensitive techniques.

It is possible to obtain new insight by utilising the chemical and site specificity of X-ray Magnetic Circular Dichroism (XMCD) to isolate the precession in different chemical species or at distinct sites in the crystal structure of a chosen material. X-ray Ferromagnetic Resonance (XFMR) combines XMCD and Ferromagnetic Resonance (FMR) phenomena in a technique capable of measuring the FMR response of an alloy or multilayer with both chemical and site specificity.

To complement the XFMR technique a low temperature Time-Resolved Magneto Optical Kerr Effect (TR-MOKE) setup has been developed. This allowed for the characterisation of samples at temperatures in the range 4 K to room temperature. A frequency swept Vector Network Analyser FMR (VNA-FMR) setup was developed to allow for a fast method for determining the resonance condition and damping of a range of ferromagnetic thin film samples.

In addition a TR-X-ray Photoemission Electron Microscopy (TR-XPEEM) setup has been established which allows images to be obtained with magnetic contrast.

The combination of the above techniques has lead to studies on rare earth capped spin valve free layers and the measurement of spin pumping in industrially relevant spin valves.

## Acknowledgments

I would like to thank my supervisor Rob Hicken for giving me the opportunity to study for a PhD in physics under him. I respect Rob's knowledge of practical matters in the lab and his knowledge of physics. His pragmatic nature has made him an easy guy to work for, cheers Rob.

I thank Paul Keatley, Andreas Neudert and Stuart Cavill for helping provide the starting point for the synchrotron based techniques discussed in this thesis that occurred during the 1<sup>st</sup> year of my PhD. I thank Jeff Childress and Jordan Katine for providing the interesting samples that I have measured during my PhD. I also thank Gerrit van der Laan who always had the time to talk and joke with a lowly student such as myself despite all that he has done in science.

I thank the support staff at Diamond, the ALS and Exeter that have helped me during my PhD. Particular thanks go to the "can do attitude" at the ALS and the "come back after tea" attitude of Russell Edge (only joking mate!).

Thanks to my mentor Peter Winlove who kindly found the time to talk to me and made the process a lot more fun than just filling out forms no one reads.

A special thanks goes to Padraic Shafer and Leigh Shelford who I learnt a great deal from and who always approached our work logically and with good humour despite the tiredness that often comes with beamtime. I also thank Elke Arenholz and Sarnjeet Dhesi, as well as all those who work under them, for letting me use their beamlines.

Thanks to Rob, Leigh, Yat-Yin Au, Prim, Stuart and Alex for proof reading parts of this thesis and spotting my many mistakes. Those that remain are my own.

Whilst university has been quite different to what I imagined I have been lucky to meet some funny, like minded people. Thanks to Prim, Russ, English Tom, Leigh and Freddy for making me laugh during my PhD. I also enjoyed talking with the down to earth guys in the workshop.

I particularly thank my good friend Toby – two guys at the back, one with a hat, 4<sup>th</sup> chair in from the right. It is refreshing to compare notes with someone who has what I would call common sense and the same sense of humour. He was also one of the few

undergraduates I found that cared as much as I did about learning rather than passing exams for the sake of it. “Any tips for the *exam?!?*”

I thank GP Srivastava whose lectures have been the highlight of my 7 years in Exeter.

A final thanks goes to my brother Alex, who I have had many interesting conversations with about physics, history and the sorry state of pro wrestling. Without his input this thesis would not have been completed. He is the smartest guy I know.

# Table of contents

|   |           |
|---|-----------|
| <b>Title page</b> .....   | <b>1</b>  |
| <b>Abstract</b> .....   | <b>3</b>  |
| <b>Acknowledgements</b> .....   | <b>4</b>  |
| <b>List of contents</b> .....   | <b>6</b>  |
| <b>List of publications</b> .....   | <b>8</b>  |
| <b>List of figures</b> .....  | <b>9</b>  |
| <b>Declaration</b> .....  | <b>16</b> |
| <b>Chapter 1: Introduction</b> .....  | <b>20</b> |
| <b>Chapter 2: Background theory</b> .....   | <b>23</b> |
| 2.1 Historical background of ferromagnetism .....                                 | 23        |
| 2.2 Energy terms in ferromagnetic systems.....                                    | 24        |
| 2.3 The equation of motion in ferromagnetic systems.....                          | 27        |
| 2.4 The Kittel formula.....   | 29        |
| 2.5 X-ray Magnetic Circular Dichroism (XMCD) .....                                | 30        |
| 2.6 Magneto Optical Kerr Effect (MOKE) .....                                      | 36        |
| <b>Chapter 3: Experimental development</b> .....                                  | <b>39</b> |
| 3.1 Experimental development of phase-resolved XFMR in fluorescence .....         | 39        |
| 3.2 Experimental development of phase-resolved XFMR in luminescence.....          | 48        |
| 3.3 Experimental development of phase-resolved VNA-FMR .....                      | 50        |
| 3.4 Experimental development low temperature Time-Resolved MOKE.....              | 55        |
| 3.5 Experimental development of Time-Resolved XPEEM.....                          | 60        |
| <b>Chapter 4: FMR characterisation of CoFe/NiFe</b> .....                         | <b>66</b> |
| 4.1 Phase-resolved XFMR in fluorescence – measurements to prove the concept ..... | 66        |
| 4.1.1. Motivation and geometry .....  | 66        |
| 4.1.2. Field sweeps .....   | 68        |
| 4.1.3. Delay scans .....  | 70        |
| 4.1.4. Dynamic XMCD spectra.....  | 71        |
| 4.1.5. An aside on the XMCD sum rules .....                                       | 74        |
| 4.1.6. Conclusions - XFMR.....  | 75        |
| 4.2 How to make frequency swept phase-resolved VNA-FMR measurements.....          | 76        |
| 4.2.1. Motivation.....  | 76        |
| 4.2.2. Non phase-resolved VNA-FMR.....  | 76        |
| 4.2.3. Phase-resolved VNA-FMR .....   | 79        |

|  |            |
|--|------------|
| 4.2.4. Conclusions VNA-FMR.....  | 80         |
| <b>Chapter 5: Enhanced damping in spin valve free layers due to the addition of Dy capping layers.....</b> | <b>81</b>  |
| 5.1 Motivation .....   | 81         |
| 5.2 Experimental setup details.....  | 81         |
| 5.3 Experimental results.....  | 83         |
| 5.4 Conclusion .....   | 91         |
| <b>Chapter 6: Phase-resolved XFMR measurements of spin pumping in spin valves.....</b>                     | <b>92</b>  |
| 6.1 Historical development of spin pumping studies.....  | 92         |
| 6.2 Experimental details.....  | 93         |
| 6.3 Spin pumping theory .....  | 95         |
| 6.4 Experimental results.....  | 97         |
| 6.5 Modelling discussion .....   | 103        |
| 6.6 Conclusion .....   | 105        |
| <b>Chapter 7: Establishing TR-XPEEM at the Diamond Light Source .....</b>                                  | <b>106</b> |
| 7.1 Motivation and sample details.....   | 106        |
| 7.2 Initial characterization with TRSKM .....  | 107        |
| 7.3 Examples of static XPEEM imaging.....  | 111        |
| 7.4 Demonstration of a working TR-XPEEM setup.....   | 113        |
| 7.5 Conclusion .....   | 116        |
| <b>Chapter 8: Progress towards establishing phase-resolved XFMR in luminescence .....</b>                  | <b>117</b> |
| 8.1 Sample details and experimental setup .....  | 117        |
| 8.2 Field sweeps .....   | 119        |
| 8.3 Dynamic XMCD spectra .....   | 120        |
| 8.4 Delay scans .....  | 122        |
| 8.5 Conclusion .....   | 127        |
| <b>Chapter 9: Conclusions and future work .....</b>  | <b>128</b> |
| 9.1 Conclusions.....   | 128        |
| 9.2 Future work .....  | 130        |
| <b>List of commonly used acronyms.....</b>   | <b>132</b> |
| <b>Appendix 1: Spin-orbit phase lag formula .....</b>  | <b>134</b> |
| <b>Appendix 2: Ferromagnetic Resonance in the limit of heavy damping.....</b>                              | <b>138</b> |
| <b>Appendix 3: Equations for the AC magnetic susceptibility in the case of spin-pumping .....</b>          | <b>140</b> |
| <b>Bibliography .....</b>  | <b>146</b> |

## List of publications

1. “Phase-resolved x-ray ferromagnetic resonance measurements in fluorescence yield” M. K. Marcham, P. S. Keatley, A. Neudert, R. J. Hicken, S. A. Cavill, L. R. Shelford, G. van der Laan, N. D. Telling, J. R. Childress, J. A. Katine, P. Shafer, and E. Arenholz, *J. Appl. Phys.* **109**, 07D353 (2011).
2. “Enhanced damping in spin valve free layers due to the addition of Dy capping layers” M.K. Marcham, P.S. Keatley, W. Yu, R.J. Hicken, L.R. Shelford, S.A. Cavill, P. Shafer, H. Qing, A. Neudert, G. van der Laan, J.R. Childress, J.A. Katine, E. Arenholz, and N.D. Telling (Manuscript in preparation for submission to *Applied Physics Letters*)
3. “Phase-resolved X-ray Ferromagnetic Resonance (XFMR) measurements of spin pumping in spin valves” M.K. Marcham, L.R. Shelford, S.A. Cavill, R.J. Hicken, P.S. Keatley, W. Yu, P. Shafer, A. Neudert, G. van der Laan, J.R. Childress, J.A. Katine, E. Arenholz, and N.D. Telling (Manuscript in preparation for submission to *Physical Review Letters*)

## List of figures

FIG. 2.3.1. A schematic diagram showing the torque terms described by the LLG equation that act upon the magnetisation. The magnetisation precesses about the direction of the effective field whilst the Gilbert damping term attempts to force the magnetisation to lie along the equilibrium direction.

FIG. 2.5.1. A schematic showing the occupation of the spin-split 2p core states for the case of the 3d transition metals.

FIG. 2.5.2. A schematic illustrating the key features of the spin resolved density states for a hypothetical 3d transition metal. The states above the Fermi level are unoccupied and have a net spin polarisation. The states showing strong energy dependence are of d character whereas those showing a flat energy dependence are of s,p character. The magnetic moment in the 3d transition metal ferromagnets comes chiefly from the d states.

FIG. 2.5.3. An example XAS spectrum from Ni. The sense of the photon helicity is fixed and the saturation direction flipped along the beam axis. The resulting difference spectrum (XMCD spectrum) contains information about the spin and orbital components of the magnetisation.

Fig. 2.5.4. The probabilities of the  $2p \rightarrow 3d$  transitions are shown in schematic form for the case of left circular polarised light ( $l = +1$ ) and the values of the total angular momentum magnetic moment given. The thickness of the lines from initial to final states represent the transition probability, the thicker the line the more likely the transition. The transitions from the 2p sub-bands are spin dependent.

Fig. 2.5.5. The integral of a Ni XMCD spectrum obtained in fluorescence yield is shown marked with the values of the integral that enter into equation 2.5.1.

FIG. 2.6.1 The geometry used to define the terms used in the equations for the Fresnel coefficients at the air – magnetic material interface (equations 2.6.1 – 2.6.4). The z-axis lies normal to the interface and the x-axis lies parallel to the interface. The y-axis is out-of-plane. (Taken from reference 32).

FIG.3.1.1. The experimental geometry for phase-resolved XFMR. The magnetization  $\mathbf{M}$  is forced into a state of steady precession about the applied bias field  $\mathbf{H}$  by an in-plane Radio Frequency (RF) magnetic field  $\mathbf{h}(t)$ . The x-rays are incident at a shallow grazing angle to detect the in-plane phase dependent component of the magnetisation.

FIG. 3.1.2. A scale drawing of the devices used to make XFMR measurements. Sample elements are fabricated on the central track of a Coplanar Waveguide (CPW) of  $50 \Omega$  characteristic impedance.

FIG. 3.1.3. A photograph of the sample holder used for XFMR experiments. It comprises a copper body, vacuum compatible SMA cabling, an interconnecting PCB waveguide and a large area UV photodiode. The photodiode faces the sample and measures the x-ray fluorescence. A thin film Al filter suspended between photodiode and sample blocks photoelectrons from striking the active area.

FIG. 3.1.4. (a) A photograph of the POMS set up on beamline I06 at Diamond. For best signal-to-noise ratio the lock-in amplifier and comb generator were separated by several metres. (b) A close up photograph of the POMS chamber. The dotted lines are guides to the eye for the 6-way cross around which the 8-pole magnetic is assembled.

FIG. 3.1.5. (a) A block diagram of the RF equipment used for XFMR measurements. A fixed phase relationship between pump and probe is obtained by using a custom comb generator system that accepts the synchrotron master oscillator as its input. The pump-probe delay is adjusted with a programmable delay generator and the photodiode signal is recovered by audio frequency lock-in detection. (b) Schematic of the principle of  $180^\circ$  phase modulation – the lock-in amplifier measures the difference between the two orange dots on the precession cycle. (c) Schematic of the principle of amplitude modulation. The lock-in amplifier measures the difference between the orange dot on the precession cycle and the orange dot that represents the equilibrium direction.

Fig. 3.2.1. A photograph of the sample stick used for XFMR experiments in luminescence yield. It comprises a Cu body, vacuum compatible SMA cabling, an interconnecting PCB waveguide and a large area UV photodiode. The photodiode sits facing the back surface of the sapphire substrate to measure the luminescence. The dashed white line highlights where the sample would be mounted.

FIG. 3.3.1 (a) A scale drawing of the  $50\ \mu\text{m}$  CPW devices originally designed for TR MOKE measurements that were later modified for use with VNA-FMR. (b) The devices were modified by removing the wide straight section shown in (a) to enable VNA-FMR measurements to be made. (c) A schematic of the high frequency microwave probes (picoprobes) used to make electrical connections to the sample CPW in VNA-FMR. (d) Schematics of the picoprobe landed on a short, open and  $50\ \Omega$  load as part of a calibration.

FIG. 3.3.2. Photographs of the experimental setup used to make VNA-FMR measurements. (a) The dipole electromagnet mounted on a slewing ring (stage removed). (b) The stage mounted above the electromagnet. A picoprobe is mounted on an X,Y,Z stage allowing it to be positioned onto the sample waveguide which sits in the depression in the stage so that it is between the pole pieces of the electromagnet.

FIG. 3.3.3 (a) A photograph of the PTFE sample block used to make VNA-FMR measurements on coupons. The stage has been offset above the pole pieces for clarity. (Inset) A side view of the PTFE block. The electrical connections to the CPW are made by attaching an SMA edge launcher to each end for a transmission geometry. (b) Scale drawing of the PCB CPW made from high frequency board. The central track width is  $500\ \mu\text{m}$ .

FIG. 3.4.2 Optical access at normal incidence is obtained through a low Verdet constant optical window allowing the polar Kerr effect to be measured. (Inset) Photograph of the experimental setup used to realise

an FMR geometry in the He flow cryostat. The cryostat is mounted on a three legged variable height platform and is suspended through the yoke of an electromagnet.

FIG. 3.4.3 (a) A photograph and (b) a schematic diagram of the pump-probe setup used to make low temperature TR-MOKE measurements. Magnetisation dynamics are excited by an RF magnetic field which is phase locked to an ultrafast pulsed laser system. The laser beam is incident on the sample surface at normal incidence so as to detect the polar Kerr effect. The pump-probe delay time is adjusted by delaying the probe beam with an optical delay line.

FIG. 3.4.4. Schematic of the cryostat cooling setup used to perform TR-MOKE measurements in the temperature range (4 K – room temperature). A He dewar is connected to the cryostat via a transfer line and the liquid He drawn through by pumping on the transfer line. The rate of the resulting flow can be controlled by a flow meter. A heater inside the cryostat cold finger helps set and regulate the temperature.

FIG. 3.5.1. (a) A photograph of the Elmitec XPEEM microscope on beamline I06 at Diamond. (b) Samples are placed in the load lock before being attached to the long manipulator under vacuum. They are then fed through the prep chamber before slotting into a holder in the PEEM ready for measurement.

FIG. 3.5.2. (a) To allow dynamics to be excited the sample elements were deposited onto the central track of a CPW which is shown in schematic form. (b & c) Photographs of the cartridge body inspired by the original Elmitec design and later modified to accommodate a macor cross on which the sample sat. (d & e) To collect the emitted photoelectrons a ring shaped cap is centred on the sample CPW and a voltage applied between the cap and the base, and the PEEM objective lens.

FIG. 3.5.3. (colour online) (a) A schematic diagram of the timing arrangement used to make TR-XPEEM measurements on beamline I06. (b) A schematic of the hybrid bunch filling structure illustrating that measurements were made only with the larger flux single bunch.

FIG. 4.1.1.1. A schematic representation of the experimental geometry used to make phase-resolved XFMR measurements. The magnetization ( $\mathbf{M}$ ) is forced into a state of steady precession about the externally applied static bias magnetic field ( $\mathbf{H}$ ) by an in-plane Continuous Wave (CW) RF magnetic field ( $\mathbf{h}(t)$ ). The probe beam is at a shallow grazing angle to detect the larger in-plane phase dependent component of magnetisation.

FIG. 4.1.2.1. (a) The  $Re$  and  $Im$  components of  $\chi_{yy}$  measured for Ni and (b) for Fe in a  $\text{Co}_{50}\text{Fe}_{50}(0.7)/\text{Ni}_{90}\text{Fe}_{10}(5)$  thin film sample by phase-resolved XFMR. Each curve is taken by sweeping the applied bias field (high to low) at fixed pump probe delay. FIG. 4.1.3.1. Delay scans are taken by sweeping the pump probe delay with the value of the applied bias field fixed. Measurements taken at the resonance field of  $\text{Co}_{50}\text{Fe}_{50}(0.7)/\text{Ni}_{90}\text{Fe}_{10}(5)$  show that the Ni and Fe moments precess in phase with one another.

FIG. 4.1.4.1. Dynamic Ni XMCD spectra acquired with fixed circular x-ray polarisation through one 4 GHz precessional cycle. The XMCD signal scales as the scalar product of the x-ray wave vector (fixed) and the local magnetisation (precessing).

FIG. 4.1.4.2. The lineshape of dynamic XMCD spectra are identical to that of conventional static XMCD spectra, proving that the XFMR setup is working correctly.

FIG. 4.1.5.1 (a) Integrals with respect to beam energy of the dynamic XMCD spectra shown in Fig. 4.1.4.1. are shown. (b) The sum rules were applied to A negative value for the ratio of the spin and orbital moments is obtained for nearly all delay values. A reasonable fit to the data is obtained by assuming a 40° angle between the spin and orbital moments.

FIG. 4.2.2.1. (a) A VNA-FMR measurement at an applied bias field of 310 Oe showing the magnitude of the reflected power as a function of excitation frequency before any background subtractions. (b) By subtracting a spectrum taken at a higher bias field value (in this case 800 Oe) it is possible to remove a lot of the spurious non magnetic signal. (c) The noise can be further reduced by calibrating out artefacts due to the RF cabling using a set of mechanical standards.

Fig. 4.2.2.2. (a) Scale drawing showing the section of the sample CPW that was removed to make VNA-FMR measurements. (inset) the unmodified sample CPW where the wide straight section of the CPW is present. (b) An attempt at measuring the magnitude of the FMR response. If the wide straight section of the sample waveguide is not removed then there is a field dependent distortion of the lineshape of similar magnitude to the FMR signal. The curves have been offset for clarity.

FIG. 4.2.3.1. To measure the purely *Re* and *Im* components of  $\chi_{yy}$  the length of the RF path outside of the VNA must be accurately accounted for. Here mechanical standards have been used to account for the cable, but not picoprobe, path lengths. A mixing of the two components is seen for two orthogonal RF phases (a & b). A spectrum taken with an 800 Oe bias field has been subtracted from each curve.

FIG. 4.2.3.2. The *Re* and *Im* components of  $\chi_{yy}$  can be measured when the affect of the path length of the picoprobes is calibrated out with a calibration substrate. A non magnetic spectrum taken with the bias field applied along the direction of the excitation field has been subtracted.

FIG. 5.2.1. A schematic diagram of the experimental geometry used to make TRSKM and phase-resolved XFMR measurements. The magnetization ( $\mathbf{M}$ ) is forced into a state of steady precession about the externally applied static magnetic field ( $\mathbf{H}$ ) by an in-plane continuous wave microwave magnetic field ( $\mathbf{h}(t)$ ). For TRSKM measurements the probe beam is at normal incidence and the polar Kerr effect is used to detect the out-of-plane component of the magnetization. For XFMR the probe beam is at grazing incidence to detect the larger in-plane oscillatory component of magnetisation.

FIG. 5.3.1. (a) Room temperature pulsed field polar Kerr measurements on  $\text{Co}_{50}\text{Fe}_{50}(0.7)/\text{Ni}_{90}\text{Fe}_{10}(5)/\text{Ru}(3)$  are noticeably more lightly damped than equivalent measurements (b) taken with the addition of a Dy capping layer. Field sweeps acquired in the presence of a 5 GHz CW excitation (c) and (d) yield the real and imaginary components of the magnetic susceptibility with the presence of Dy (d) noticeably broadening the line width and therefore enhancing the damping.

FIG. 5.3.2. (a) *Im* FMR curves were measured, with a measurable signal occurring over the whole range of temperatures (10 – 250 K), for the control sample. (b) With the addition of a Dy capping layer the line width is broadened at room temperature and broadened further at low temperature. Dynamics become too

heavily damped to be resolved below 140 K. (c) Lorentzian fitting was used to extract the resonance field, (d) line width and (e) amplitude for both samples. Cooling was performed at remanence for all measurements.

FIG. 5.3.3. (a) Dy XMCD spectra in fluorescence yield measured as a function of temperature, cooling was performed at remanence. The strong monotonic increase in the area under the Dy  $M_5$  peak indicates an increased ferromagnetic ordering of the Dy cap. (b) Dy  $M_5$  and (c) Ni  $L_3$  hysteresis loops taken after cooling in a 5 kOe cooling field directed along the x-ray wave vector show there is a net parallel alignment between the ferromagnetically ordered Dy and ferromagnetically ordered Ni moments. The loops also show that no exchange bias could be induced.

FIG. 5.3.4. Phase-resolved XFMR measurements combine the chemical sensitivity of XMCD with picosecond temporal resolution. Room temperature measurements on the Dy capped sample confirm that the Ni, Fe and Co precess in phase with one another.

Fig. 5.3.5 (a) VSM measurements on the control sample show an increase of approximately 10% in the magnetisation, for the range of fields measured with FMR, when the sample is cooled from room temperature to 100 K. (b) No appreciable change is seen in the magnetisation of the Dy capped sample when it is cooled from room temperature to 100 K.

FIG. 6.2.1 A schematic of the experimental geometry used to make phase-resolved XFMR measurements. The magnetisation ( $\mathbf{M}$ ) is forced into a state of steady precession about the applied bias field ( $\mathbf{H}$ ) by an in-plane continuous wave RF magnetic field ( $\mathbf{h}(t)$ ). The probe beam is at grazing incidence to detect the large in-plane oscillatory component of the magnetisation.

FIG. 6.3.1 A vector diagram showing the terms acting on the fixed layer magnetisation ( $\mathbf{m}_2$ ) for cases where the applied field is above, and below the free layer resonance field respectively. (Inset) The reorientation of the spin-pumping term causes a change in the phase of the fixed layer as a function of applied field.

FIG. 6.4.1 Hysteresis loops measured with longitudinal MOKE after x-ray irradiation during XFMR measurements for (a) the valve with Cu spacer (b) the control sample with Cu/Ta/Cu spacer. Both samples had an exchange bias field of 600 Oe before x-ray irradiation.

FIG. 6.4.2 (a) The  $Im$  component of the AC magnetic susceptibility component  $\chi_{yy}$  from the free layer (spin pump) of the valve with Cu spacer and (b) for the control sample. The linewidth is determined by the combined effect of intrinsic Gilbert damping ( $\alpha^{(0)}_l$ ) and the additional Gilbert-like damping term due to spin pumping ( $\alpha^{SP}_l$ ).

FIG. 6.4.3 (colour online) (a) Fixed layer (spin sink) delay scans (7 GHz excitation) at different applied bias fields for the valve with Cu spacer. A strong variation in the phase is seen for different applied bias field values. The amplitude is also seen to increase near to the free layer resonance field (530 Oe) as shown in (c). (b) Fixed layer (spin sink) delay scans (5 GHz excitation) at different applied bias fields for the control sample. No such variation in the phase (or amplitude (d)) is seen for different bias field values.

Red lines are sinusoidal fits to the data where the period is constrained to be equal to that of the RF excitation.

FIG. 6.4.4 (colour online) (a) The experimental and modelled phase relative to the driving field of the response of the free layer and fixed layers are shown for the valve with Cu spacer. The fixed layer phase shows a bipolar response about the free layer resonance field indicative of STT coupling as predicted from (Fig. 6.3.1) The peak-to-peak width of the bipolar feature matches the FWHM of the free layer resonance (50 Oe). (b) The experimental and modelled phase relative to the driving field of the response of the free layer and fixed layers are shown for the control sample. The fixed layer phase shows no deviation at the free layer resonance field from its broad sigmoidal response that is indicative of very heavily damped SHO. In both (a) & (b) the following modelling parameters were used;  $\alpha^{SP}_1 = 0.0050$  and  $\alpha^{SP}_2 = 0.0034$ .

FIG. 7.1.1. A schematic diagram of the sample CPW used for TR-XPEEM measurements. The sample elements are deposited onto the central track of a CPW waveguide so they experience an in-plane excitation field. The CPW is terminated by a 50  $\Omega$  thin film resistor to prevent back reflections.

FIG. 7.2.1. A schematic of the TRSKM. A Ti: sapphire ultrafast laser system probes the magnetisation dynamics induced in micro and nano scale elements by an in-plane pulsed field. Time resolution is obtained by shifting the pump-probe delay by sending the probe pulse through an optical delay line.

FIG. 7.2.2. A schematic diagram defining the polar Kerr geometry and the Kerr rotation ( $\theta_K$ ) and ellipticity ( $\epsilon_K$ ) that arise from the reflection of linearly polarised light from a magnetic material. The case of s-polarised light is shown.

FIG. 7.2.3 (a) The response of a 5  $\mu\text{m}$   $\text{Ni}_{81}\text{Fe}_{19}$  square element to an in-plane pulsed field. Zero time delay is defined as the time at which pulsed field reaches 10% of its maximum value. (b) An intensity image of the 5  $\mu\text{m}$  square. (c) By setting the pump-probe delay to the first negative anti node in the pulsed field response it is possible to obtain a spatial map of the dynamic polar Kerr signal. (d) & (e) The dynamic contrast is seen to reverse at successive anti nodes.

FIG. 7.3.1. (a) XPEEM images of flux closure states within 10  $\mu\text{m}$  circle and square elements. (b) Landau states with the same sense of circulation are shown for a pair of 2  $\mu\text{m}$  square elements separated by a 100 nm gap that has not been resolved. SEM images of (c) a 10  $\mu\text{m}$  circle (d) a 10  $\mu\text{m}$  square and (e) a pair of 2  $\mu\text{m}$  squares separated by 100 nm.

FIG. 7.4.1 The pulse profile acquired from an APD as measured by a 50 GHz oscilloscope. Zero time delay is defined as the point at which the pulse height reaches 10% of its maximum value.

FIG. 7.4.2. (a) A intensity image taken with the PEEM of several 2  $\mu\text{m}$  elements before the arrival of the pulsed magnetic field (negative time delay). (b) When the pulsed field and the x-ray pulses arrive at the same time the intensity contrast from the sample elements is seen to washout in the same direction for each sample due to the deflection of photoelectrons caused by the presence of the pulsed field.

FIG. 7.4.3. A TR image series of a pair of well separated 2  $\mu\text{m}$  square elements subject to an in-plane pulsed field excitation. Magnetic contrast is seen in all images but the resolution of the TR-XPEEM setup

is not yet sufficient for precession or vortex gyration to be clearly seen throughout the image series. (Inset) The direction of the pulsed field and x-ray wave vector are shown relative to the sample elements. FIG. 8.1.1. Ni XMCD spectra in luminescence at angles at a range of angles of incidence; (a) 70°, (b) 45° and (c) 30°. (Inset) A schematic defines the angle of incidence relative to the sample normal. The cleanest signal is obtained for a 45° angle of incidence.

FIG. 8.1.2. The experimental geometry used to make luminescence measurements is the same as that detailed previously for fluorescence, but with the angle of incidence changed reduced to 45°. The magnetisation  $\mathbf{M}$  is forced into a state of steady precession about the applied bias field  $\mathbf{H}$  by an in-plane Radio Frequency (RF) magnetic field  $\mathbf{h}(t)$ . The x-rays measure a mixture of the in- and out-of-plane components of the magnetisation.

FIG. 8.2.1. The *Re* and *Im* components of  $\chi_{(yx)y}$  measured for Ni in a Ni<sub>80</sub>Fe<sub>20</sub>(5) thin film sample by XFMR in luminescence yield. Both curves were taken by sweeping the bias field (high to low) at a fixed pump-probe delay.

FIG. 8.3.1. (a) Dynamic XMCD spectra for Ni obtained in luminescence with XFMR at resonance from a Ni<sub>80</sub>Fe<sub>20</sub>(5) thin film sample at the ALS (b) Dynamic XMCD spectra obtained for Ni in a Co<sub>50</sub>Fe<sub>50</sub>(0.7)/Ni<sub>90</sub>Fe<sub>10</sub>(5) thin film sample at resonance in fluorescence yield at the ALS are shown for comparison. The same amount of averaging was performed for both (a) and (b).

FIG. 8.4.1. Delay scans taken at both the Ni L<sub>3</sub> and L<sub>2</sub> edges from in a Ni<sub>80</sub>Fe<sub>20</sub>(5) thin film sample by XFMR in luminescence yield by sweeping the pump probe delay at the resonance field. Note the surprising departure from a  $\pi$  phase shift between the two curves.

FIG. 8.4.2. Delay scans taken at both the Ni L<sub>3</sub> and L<sub>2</sub> edges from a Ni<sub>80</sub>Fe<sub>20</sub>(5) thin film sample by XFMR in luminescence yield (shown previously in Fig. 8.4.1.) are overlaid with a scan taken on the Ni pre-edge (840 eV) where no dichroism is present.

FIG.8.4.3. Delay scans were taken at different applied bias fields and x-ray beam energies to characterise the oscillatory background present in the luminescence setup. The phase and amplitude from each delay scan were extracted with sinusoidal fitting and tabulated. The amplitude and  $X_c$  are also defined.

FIG. A2.1. The geometry used: the magnetisation lies in the sample plane and is saturated by an in-plane static field. An RF magnetic field is applied to the sample causing the magnetisation to enter a state of steady precession. FIG. A2.2 The temporal profile of the x-ray pulses are modelled as a top-hat function with unit area, centred on ( $t' = t$ ).

## **Declaration**

The work presented in this thesis was carried out in collaboration with colleagues from the Magnetic Materials group in Exeter as well as a number of colleagues from further afield. I take this opportunity to acknowledge their input on a chapter by chapter basis.

Firstly I acknowledge, for brevity, the input of my supervisor Rob Hicken who contributed to all areas of the work presented in this thesis.

## **Chapter 1: Introduction**

The introductory chapter broadly describes the content of this thesis and is my own work.

## **Chapter 2: Background theory**

The background concepts that are necessary to understand the later chapters of this thesis were written by myself after a survey of the existing body of literature. My sources have been referenced throughout.

## **Chapter 3: Experimental development**

The main experimental technique used in this thesis is phase-resolved X-ray Ferromagnetic Resonance (XFMR) in fluorescence yield. The first experimental setup was developed at the Diamond Light Source with Andreas Neudert, Paul Keatley and Stuart Cavill during the 1<sup>st</sup> year of my PhD. From the 2<sup>nd</sup> year of my PhD onwards I made the project my own and oversaw all subsequent experimental modifications as well as establishing the technique at the Advanced Light Source. This was done in conjunction with Padraic Shafer, Elke Arenholz and Leigh Shelford, who have provided me with many useful ideas as well as helping greatly in the development of phase-resolved XFMR in luminescence.

The Time-Resolved X-ray Photoemission Electron Microscopy (TR-XPEEM) setup was developed with Paul Keatley, Andreas Neudert, Stuart Cavill and with useful input from Sarnjeet Dhesi.

The low temperature TR-MOKE setup was built by myself and Russell Edge with useful input from Leigh Shelford – from whose earlier experiments we inherited the

bulk of the low temperature equipment that we needed. The ultrasfast laser, detection scheme and timing electronics were established in Exeter long before the start of my PhD.

The phase-resolved Vector Network Analyser-Ferromagnetic Resonance (VNA-FMR) came from me playing around in the lab one day and some useful chats with Yat-Yin Au about his previous work. I was fortunate to inherit the electromagnet/probe station and some of the RF pieces from a TR-MOKE setup built several years earlier by Paul Keatley.

I was assisted by the mechanical workshop in the development of all of these experiments.

## **Chapter 4: FMR characterisation of CoFe/NiFe**

The XFMR results were the work of several people, all of whom are co-authors on the following paper:

“Phase-resolved x-ray ferromagnetic resonance measurements in fluorescence yield” J. Appl. Phys. **109**, 07D353 (2011). Max Marcham, Paul Keatley, Andreas Neudert, Rob Hicken, Stuart Cavill, Leigh Shelford, Gerrit van der Laan, Neil Telling, Padraic Shafer and Elke Arenholz all contributed to the development of the XFMR technique and to taking the data presented. Jeff Childress and Jordan Katine fabricated the samples that were measured.

The VNA-FMR results are my own work. The samples were fabricated by Jeff Childress and Jordan Katine.

## **Chapter 5: Enhanced damping in spin valve free layers due to the addition of Dy capping layers**

The room temperature TR-MOKE data is the work of Paul Keatley. The low temperature MOKE measurements are the work of myself and Wei Yu with valuable input from Leigh Shelford and Russell Edge. The temperature dependent XMCD spectra were taken by myself, Leigh Shelford, Padraic Shafer, Elke Arenholz and Qing He at the ALS. The XFMR data was taken by myself, Leigh Shelford, Padraic Shafer and Elke Arenholz. This work built upon work done earlier at Diamond and so all those mentioned in the acknowledgements to chapter 4 that I have not yet mentioned here also

deserve an honourable mention. The samples were fabricated by Jeff Childress and Jordan Katine.

## **Chapter 6: Phase-resolved XFMR measurements of spin pumping in spin valves**

The XFMR data shown in this chapter was taken by myself, Leigh Shelford and Stuart Cavill at the Diamond Light Source. Earlier attempts to characterise the samples with XFMR were made in conjunction with the above people as well as Paul Keatley, Andreas Neudert, Elke Arenholz and Padraic Shafer. The Matlab code used to model the observed dynamics was written by Rob Hicken who later showed me how to use it. The underlying algebra was proofed by Padraic Shafer. The modelled curves shown were produced by myself as a result of frequent discussion with Rob Hicken. The samples were fabricated by Jeff Childress and Jordan Katine. Hysteresis loops were measured with MOKE by myself, Paul Keatley and Wei Yu. Some initial TR-MOKE characterisation was performed by Prim Gangmei.

## **Chapter 7: Establishing TR-XPEEM at the Diamond Light Source**

The TR-XPEEM setup was developed at the Diamond Light Source by myself, Stuart Cavill, Paul Keatley and Andreas Neudert with valuable input from Sarnjeet Dhesi. The TRMOKE data was taken by myself and Prim Gangmei with valuable input from Paul Keatley, who had already developed the experimental setup. Jeff Childress and Jordan Katine fabricated the samples measured.

## **Chapter 8: Progress towards establishing phase-resolved XFMR in luminescence**

The work on developing XFMR in luminescence yield was carried out by myself, Leigh Shelford, Padraic Shafer and Elke Arenholz at the ALS. The work built upon the experience gained from developing the fluorescence yield setup. Jeff Childress and Jordan Katine fabricated the samples measured.

## **Chapter 9: Conclusions and future work**

The conclusion is my own work. The proposals for future work stemming from this thesis comes from numerous discussions with collaborators during the course my PhD, in particular the frequent discussions I have had with Rob Hicken. Work that is already

ongoing using the techniques developed during this PhD project are mentioned in brief and will no doubt be discussed in detail by future users of these experiments.

## **Appendices**

The mathematics and Matlab coding are the work of Rob Hicken, who showed me how to use it and guided how I employed it.

## Introduction

This thesis is concerned largely with the experimental study of the magnetisation dynamics that occur in thin film ferromagnets on picosecond time scales.

To realise this goal a number of time/phase-resolved techniques have been developed. Phase-resolved X-ray Ferromagnetic Resonance (XFMR) in fluorescence yield exploits the inherent timing structure of synchrotron radiation to make chemically resolved FMR measurements on samples that are opaque in the soft x-ray regime. In addition progress has also been made towards developing a phase-resolved XFMR setup which detects the substrate luminescence which occurs when soft x-rays are absorbed by substrate materials such as sapphire or MgO. A low temperature time resolved Magneto Optical Kerr Effect (MOKE) setup was developed to allow the dynamic characterisation of thin films down at temperatures as low as 4 K. A phase-resolved Vector Network Analyser-Ferromagnetic Resonance (VNA-FMR) setup was built to allow for high quality characterisation of the resonance condition and damping of a large number of samples prior to more in depth synchrotron based studies. In addition to these various FMR setups a Time-Resolved X-ray Photoemission Electron Microscopy (TR-XPEEM) setup was constructed to allow magnetisation dynamics to be imaged with chemical sensitivity and magnetic contrast. This extends the MOKE based imaging already established in Exeter before the start of this PhD project. The development of all of these experimental techniques is detailed in Chapter 3.

Chapter 4 shows already published results obtained from the XFMR setup demonstrating its suitability for making chemically resolved FMR measurements with a timing resolution of just a few picoseconds. VNA-FMR measurements are also shown.

Chapter 5 combines a variety of experimental techniques to learn more about the dynamic properties of  $\text{Co}_{50}\text{Fe}_{50}$  (0.7 nm)/ $\text{Ni}_{90}\text{Fe}_{10}$  (5 nm)/Dy (1 nm) – a stack representative of the the free layers in high density recording heads currently used in industry. The Dy capping layer was added to enhance the damping. TR-MOKE measurements show an enhanced damping of the dynamics in the CoFe/NiFe at room temperature as a result of the addition of the Dy cap. Low Temperature MOKE measurements show that the dynamics become further enhanced with decreasing temperature whilst no such trend is observed in a control sample where the Dy cap is

not present. Dy XMCD spectra show that magnetic order within the Dy ordering increases with decreasing temperature and that a net Dy moment is seen even at room temperature, whereas bulk Dy is paramagnetic. For all temperatures the Dy and Ni moments projected along the x-ray wave vector were seen to align antiparallel with one another. Possible explanations for the trends seen in the FMR data are then discussed and tested experimentally.

Chapter 6 uses XFMR to study spin pumping in industrially relevant spin valve stacks with lateral dimensions of hundreds of microns. Previous studies in this area have used either cavity based FMR or depth selective TR-MOKE. Here the chemical sensitivity of XFMR is used to completely separate the dynamic signal coming from the free and fixed layers by tuning the x-ray energy to a absorption edge of an element present in only the free layer, or only the fixed layer. The existing body of literature on spin pumping is discussed and the signatures of the effect detailed. Clear evidence of spin pumping was observed in a valve whose spacer layer lies in the spin ballistic regime by setting the free layer to resonance and measuring the dynamics induced in the fixed layer. A control sample with a highly spin diffusive spacer was also measured and no dynamics induced in the fixed layer as a result of spin pumping were observed. A macrospin model based on the Landau-Liftshitz-Gilbert-Slonczewski equation was used to model the observed dynamics. The model is detailed in an appendix.

Chapter 7 details the progress made towards establishing TR-XPEEM at the Diamond Light Source. The sample suitability was determined by TR-MOKE measurements, the results of which are shown. Static XMCD images with magnetic contrast were obtained from a range of micro magnets. The first TR-XPEEM image series obtained with the experimental setup is then shown.

Chapter 8 details the progress made to date in developing phase-resolved XFMR in luminescence. The dynamic measurements obtained previously in fluorescence yield were replicated and are shown in this chapter. A background whose phase is field dependent was found to be present in this experimental setup and it is detailed for future reference.

Chapter 9 brings together the key conclusions from this thesis. The chapter then goes on to outline the prospects for future work stemming from this thesis. This includes both extensions to the studies presented in this thesis as well as ways in which the

experimental setups developed during this PhD project could be used to study systems which have received little dynamic characterisation to date, and so offer the possibility of discovering new and exciting physics.

## Chapter 2: Background theory

This chapter introduces the underlying theoretical concepts necessary to understand the experimental studies presented in this thesis. The first part gives an overview of the key concepts of ferromagnetism, with particular emphasis on Ferromagnetic Resonance (FMR) as this is the main phenomenon studied in this thesis. The second part introduces the effects utilised to study FMR in this thesis; X-ray Magnetic Circular Dichroism (XMCD) and the Magneto Optical Kerr Effect (MOKE). The formulae presented in this chapter are written exclusively in cgs units as this is the most widely used system of units in the field of magnetism.

### 2.1 Historical background of ferromagnetism

While it has been known for several millennia that materials such as lodestone possess magnetic properties, it was not until relatively recently that our collective understanding of magnetism and the large number of ways in which it manifests itself received intensive study. The first quantitative theory of paramagnetism, an effect where the randomly orientated magnetic moments in a material order so as to give a net alignment along the direction of an applied magnetic field, was developed by Langevin<sup>1</sup>. For a paramagnetic material the field induced ordering ceases when the applied magnetic field is removed. There is however a class of materials where the magnetic ordering remains, these are known as ferromagnetic materials. The first attempt at a quantitative description of ferromagnetism was carried out by Weiss<sup>2</sup>, who postulated the existence of an internal magnetic field (the Weiss molecular field) that was sufficiently large to strongly order the magnetic dipoles within ferromagnetic materials. Although a step forward in the understanding of ferromagnetism the Weiss field was an *ad hoc* solution, for which no experimental evidence or strong theoretical justification was found. With the advent of quantum mechanics it was later shown by Heisenberg<sup>3</sup>, amongst others, that the Weiss field was in fact a simplified representation of a far more subtle concept with no classical analogue which originates in the interplay between the Pauli Exclusion Principle and electrostatics, the exchange interaction. While the exchange interaction in itself does not provide a complete description of ferromagnetism, other effects such as the magnetic dipole interaction and system dependent anisotropies must all be taken into account. These will be discussed in greater detail later in this chapter. The interplay

between these various different interactions was first captured quantitatively by Landau and Lifshitz<sup>4</sup> who developed a phenomenological description of both the static and dynamic properties of ferromagnetic materials that was based on the variational principle. According to their pioneering work the ground state of any magnetic system is a minimum of the total free energy of that system. After defining the magnetisation  $\mathbf{M}$ , and an effective field  $\mathbf{H}_{\text{eff}}$  which contains the contributions from the exchange, magnetic dipole and anisotropies, equilibrium occurs when the effective field lies parallel to the magnetisation and so exerts no torque upon it<sup>5</sup>

$$\mathbf{M} \times \mathbf{H}_{\text{eff}} = 0 \quad (2.1.1)$$

where  $\mathbf{H}_{\text{eff}}$  is defined as the functional derivative with respect to magnetisation of the free energy density  $w_{\text{free}}$

$$\mathbf{H}_{\text{eff}} = - \frac{\delta w_{\text{free}}}{\delta \mathbf{M}} \quad (2.1.2)$$

## 2.2 Energy terms in ferromagnetic systems

Now that the effective field has been defined it is necessary to look in more detail at its constituent interactions.

First of all there is the exchange interaction, which is responsible for the parallel ordering of the magnetic moments of neighbouring atoms in a ferromagnetic material even in the absence of an external field. It is the dominant interaction on length scales of 5 – 10 nm and is isotropic. The energy between neighbouring spins  $i$  and  $j$  can be written as<sup>6</sup>

$$E_{\text{ex}} = - \sum_{i \neq j} J_{ij} \mathbf{S}_i \cdot \mathbf{S}_j \quad (2.2.1)$$

where  $J_{ij}$  is the exchange integral. It should be noted that ferromagnetism is a temperature dependent phenomenon. The exchange interaction is competing against the thermally induced kinetic energy of the atomic magnetic moments which seeks to disorder the magnetic system. The temperature at which the exchange interaction is overcome, and the material becomes paramagnetic, is known as the Curie temperature<sup>7</sup>. The transition temperature for antiferromagnetic materials is known as the Néel temperature.

Whilst the exchange interaction is responsible for ferromagnetic materials exhibiting a net magnetisation in zero field, not every ferromagnetic body will necessarily exhibit

such behaviour. This apparent road block in our understanding of ferromagnetism is readily explained by the presence of magnetic domains<sup>8</sup>, an idea first postulated by Weiss. A magnetic domain is a region of a magnetic body in which the magnetic moments are all aligned parallel. It is not the case however that the net moments in neighbouring domains align parallel with one another. As a result they are separated from one another by domain walls, in which the magnetisation reorients. The precise alignment of the domains depends upon the local field history, resulting in magnetic hysteresis<sup>9</sup>. To fully understand these effects it is necessary to look at more interactions than just the isotropic exchange interaction.

Firstly, there is the magnetic dipole interaction. Each magnetic moment can be pictured as a circulating current loop, a system which produces the same magnetostatic field distribution as a pair of spatially separated fictitious magnetic charges of opposite sign – hence the use of the term magnetic dipole. Although the magnetic dipole interaction is several orders of magnitude weaker than the exchange interaction its long range makes it a vital constituent of a complete description of a ferromagnetic system. The associated energy density can be written as

$$w_{\text{dipole}} = -\frac{1}{2} \mathbf{M} \cdot \mathbf{H}_d \quad (2.2.2)$$

where  $\mathbf{H}_d$  is the demagnetising field: the part of the magnetic dipole field which is inside the ferromagnetic body. It seeks to lower the energy cost of the external magnetic dipole field and can be written as the gradient of the associated magnetic scalar potential. In the case of a uniformly magnetised body the demagnetising field will not necessarily be spatially uniform, and can be written as

$$\mathbf{H}_d(\mathbf{r}) = -\mathbf{N}(\mathbf{r}) \cdot \mathbf{M} \quad (2.2.3)$$

where  $\mathbf{N}(\mathbf{r})$  is known as the demagnetising tensor. In the special case of an ellipsoidal sample that is uniformly magnetised the demagnetising field is spatially uniform<sup>10</sup>. As a result micromagnetic studies of nanomagnets often make the simplifying assumption that the shape can be approximated as an ellipsoid.

Secondly there are various different types of anisotropy that one must consider as the isotropic exchange interaction cannot explain the observation of spatially non uniform magnetisation distributions – domains and domain walls. Firstly there is the Magneto Crystalline Anisotropy<sup>11</sup> (MCA) which describes the observation that the magnetisation

will preferentially align along, or at set angles relative to, particular crystallographic axes of a given material. The exact form of the MCA then depends strongly on the symmetry and lattice structure of the material. The axis along which the magnetisation preferentially aligns is referred to as the Easy Axis (EA). For suitably thick 3d transition metal thin films the EA will lie in the plane of the film due to the large magnetic dipole energy that is generated when the magnetisation is saturated out-of-plane. There are however systems in which the EA lies perpendicular to the plane of the thin film, such materials are then said to exhibit perpendicular anisotropy<sup>12</sup>. The most common form of MCA is uniaxial anisotropy, for which the energy density term can be written as

$$w_{uni} = -K_2(\hat{\mathbf{m}} \cdot \hat{\mathbf{E}})^2 \quad (2.2.4)$$

where the unit vectors  $\hat{\mathbf{m}}$  and  $\hat{\mathbf{E}}$  point along the magnetisation and the uniaxial anisotropy EA respectively and  $K_2$  is the uniaxial anisotropy constant. The reader is referred elsewhere<sup>13</sup> for more details on MCA.

There are then the surface and shape anisotropies that stem from the magnetic dipole energy and play a crucial role in determining the spatial variation of the demagnetising field. Each have a  $(\hat{\mathbf{m}} \cdot \hat{\mathbf{n}})^2$  dependence for the case of a thin film, where  $\hat{\mathbf{n}}$  is the surface normal unit vector, and so are often hard to distinguish from one another. They can be written as a single energy density of the form<sup>14</sup>

$$w_{\text{surface}} + w_{\text{shape}} = 2 \left( \pi M^2 - \frac{K_{\text{surface}}}{d} \right) (\hat{\mathbf{m}} \cdot \hat{\mathbf{n}})^2 \quad (2.2.5)$$

$$w_{\text{eff}} = (2\pi M_{\text{eff}}^2) (\hat{\mathbf{m}} \cdot \hat{\mathbf{n}})^2 \quad (2.2.6)$$

where  $w_{\text{surface}}$ ,  $w_{\text{shape}}$  and  $w_{\text{eff}}$  are the surface, shape and effective energy densities respectively,  $d$  is the thickness of the thin film, and  $M_{\text{eff}}$  is the effective sample magnetisation which contains the surface anisotropy constant  $K_{\text{surface}}$ .

In addition to the exchange, magnetic dipole and anisotropy energy densities one must also consider the energy of interaction between the magnetic moments in a body and an externally applied magnetic field. This energy density term is named after its discoverer, Zeeman, and takes the form

$$w_{\text{Zeeman}} = -\mathbf{M} \cdot \mathbf{H}_{\text{external}} \quad (2.2.7)$$

where  $\mathbf{H}_{\text{external}}$  is the external field which could be static, time varying – either harmonic or pulsed, or the result of exchange bias due to interfacial coupling with an

antiferromagnetic material which results in a unidirectional anisotropy, often represented by an exchange bias field,  $\mathbf{H}_{\text{exb}}$ . The detailed origins of exchange bias have received much attention due to both fundamental interest and device applications but at the time of writing are still not fully understood. For a review of the work undertaken in this area the reader is referred elsewhere<sup>15</sup>.

To summarise the above discussion of the various energy terms in ferromagnetic thin films one can write the total energy density,  $w_{\text{total}}$  in the following form

$$w_{\text{total}} = w_{\text{exchange}} + w_{\text{dipole}} + w_{\text{anisotropy}} + w_{\text{Zeeman}} \quad (2.2.8)$$

where  $w_{\text{anisotropy}}$  contains all of the anisotropy terms of the system under investigation.

### 2.3 The equation of motion for ferromagnetic systems

Dynamic magnetisation processes, and associated relaxation, are described phenomenologically by the Landau-Lifshitz-Gilbert equation<sup>16</sup> (LLG) in the regime where the magnitude of the magnetisation is a constant of motion. The LLG equation takes the form

$$\frac{\partial \mathbf{M}}{\partial t} = -\gamma[\mathbf{M} \times \mathbf{H}_{\text{eff}}] + \frac{\alpha}{M} \left[ \mathbf{M} \times \frac{\partial \mathbf{M}}{\partial t} \right] \quad (2.3.1)$$

where  $\gamma$  is the gyromagnetic ratio and  $\alpha$  is the dimensionless phenomenological Gilbert damping parameter. Equation 2.3.1 states that in the absence of damping the magnetisation will precess indefinitely about the effective field. In the presence of damping energy is dissipated causing the magnetisation to follow a spiral trajectory which will eventually end with it returning to lie along the direction of the effective field. If the energy loss due to damping is offset by the energy supplied by a driving force then the magnetisation will precess about the effective field in a state of steady precession. The amplitude and phase relative to the driving field of the precessing magnetisation will be determined by a combination of the amplitude of the driving force and the resonance condition of the magnetic system. In the presence of a time dependent driving field it is convenient to separate the time independent and dependent effective fields into separate torque terms. One can then draw the torque terms that act upon the magnetisation as shown below in Fig. 2.3.1.

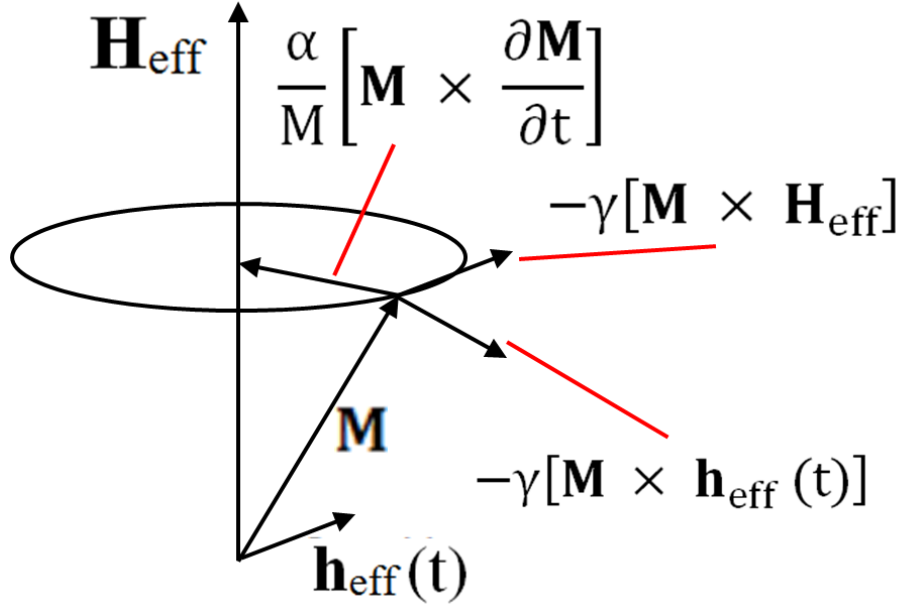


FIG. 2.3.1. A schematic diagram showing the torque terms described by the LLG equation that act upon the magnetisation. The magnetisation precesses about the direction of the effective field while the Gilbert damping term attempts to force the magnetisation to lie along the equilibrium direction. The term due to the driving field acts to open up the cone angle.

As well as being excited by pulsed and harmonic magnetic fields the magnetisation can also be driven by Spin Transfer Torque (STT) effects. STT involves the absorption of a flow of spin angular momentum (spin current) by a ferromagnetic system. As the spin current and sample magnetisation are not necessarily polarised along the same direction the absorption of the spin current generates a torque which can reorient the magnetisation. The spin current may be supplied in one of two ways. Firstly, by passing an electrical current with a net spin polarisation into a ferromagnetic structure, as in the case of a Current Perpendicular to the Plane (CCP) spin valve. This effect was predicted independently by Slonczewski<sup>17</sup> and Berger<sup>18</sup>. The resulting dynamics are described phenomenologically by a modified LLG equation known as the Landau-Lifshitz-Gilbert-Slonczewski (LGGs) equation<sup>19</sup>. Secondly a pure spin current (a spin current that is not accompanied by a charge current) can be pumped into a normal metal (NM) layer that is in direct contact with a ferromagnetic layer (FM) by the precessing magnetisation of the FM, the prediction of which is generally attributed to Tserkovnyak<sup>20</sup>. For further details on the theory of spin pumping and its historical development the reader is referred to the experimental work on pure spin current driven dynamics in Chapter 6 of this thesis.

In general the magnetisation distribution is spatially inhomogeneous, in which case the partial derivatives in equation 2.3.1 would need to be replaced by total derivatives so that changes in the magnetic system are considered as both a function of time and as function of position. A complete description of spatially non uniform magnetisation dynamics requires the concept of a spin wave – a spatially periodic and time dependent disorder of the magnetic system. Two of the most common forms of spin wave are the Damon-Eschbach<sup>21</sup> spin wave where the static magnetisation lies in the sample plane and is orthogonal to the in-plane wave vector, and the backward volume spin wave<sup>22</sup> where the static magnetisation and the in-plane wave vector lie parallel to one another. The term “backward volume” is used as such spin waves have a negative group velocity. By considering spatially uniform dynamics one arrives at an equation that is of central importance to the FMR studies presented later in this thesis.

## 2.4 The Kittel Formula

As demonstrated by Landau and Lifshitz, the magnetisation of a body precesses about the net effective field. A quantity of particular interest is the resonant precessional frequency of the magnetisation and how this depends on the static and dynamic effective fields. Consider an ellipsoid (uniformly magnetised) along one of its principle axes by an external field, which is spatially uniform and non varying in time. It is possible to greatly simplify the problem by diagonalising the demagnetisation tensor, giving a spatially uniform demagnetising field. For a thin film that is magnetised in plane and has an in plane EA one then obtains the famous Kittel equation<sup>23, 24</sup>

$$\frac{\omega}{\gamma} = \sqrt{(H_{\text{ext}} + H_{\text{uni}}) \left( H_{\text{ext}} + \left( 4\pi M - \frac{2K_{\perp}}{M} \right) \right)} \quad (2.4.1)$$

where  $\omega$  is the angular frequency,  $\gamma$  is the gyromagnetic ratio,  $H_{\text{ext}}$  is the external field,  $H_{\text{uni}}$  is the uniaxial anisotropy field,  $M$  is the magnetisation and  $K_{\perp}$  is the perpendicular anisotropy constant. It is noted that the precise form of anisotropy term(s) depends strongly on the crystallographic structure of the material under investigation. In the limit of weak anisotropy,  $H_{\text{anisotropy}} \ll H_{\text{ext}}$ , the Kittel equation can be reduced to

$$\frac{\omega}{\gamma} = \sqrt{H(H + 4\pi M)} \quad (2.4.2)$$

If a periodic perturbation is added to the effective field, for example the sample is subject to a harmonic excitation, the relationship between the magnetisation and effective field can be written as

(2.4.3)

$$\mathbf{M} = \mathbf{M}_0 + \mathbf{m}(t) = \mathbf{M}_0 + \chi_{ij} \mathbf{h}_j(t)$$

where  $\mathbf{m}(t)$  denotes the time varying component of the magnetisation,  $\mathbf{M}_0$  is the time independent component of the magnetisation and  $\chi_{ij}$  is a tensor known as the magnetic susceptibility. The specific component(s) of  $\chi_{ij}$  that are measured are then dependent upon the direction of the excitation and which magnetisation component is being detected in the experiment. When only the time varying component,  $\mathbf{m}(t)$ , is measured it is common to refer to  $\chi_{ij}$  as the AC magnetic susceptibility. As any resonance is described both by an amplitude and a phase relative to the driving field, each component of  $\chi_{ij}$  is a complex number. The *Re* part is said to be of dispersive character and goes to zero at the resonance field. The Lorentzian shaped *Im* part is related to the energy absorbed from the driving field by the magnetic system and is a maximum at the resonance field and is said to be of absorptive character.

The reader is referred to chapter 4 of this thesis for experimental measurements<sup>25</sup> of the AC magnetic susceptibility which show the lineshapes of the *Re* and *Im* parts of  $\chi_{ij}$  and discusses in more detail their significance and how they can be measured. A derivation of  $\chi_{ij}$  is given in Appendix 3.

It is possible to fix the external field and sweep the excitation frequency, although a large amount of noise is typically present in experiments due to frequency dependent impedance matching effects. For this reason it is more common to fix the excitation frequency and sweep the external field. Example experimental data is shown in chapter 4 for both methods.

## 2.5 X-ray Magnetic Circular Dichroism (XMCD)

X-ray Magnetic Circular Dichroism (XMCD) was discovered experimentally in 1987<sup>26</sup> and has since become a widely used technique for performing element specific characterisation of magnetic materials with synchrotron radiation. The purpose of the following discussion is to introduce the reader to the basic ideas underlying XMCD, which is used in the studies presented later in this thesis.

The following discussion will concentrate on the so called  $L_{2,3}$  absorption edges in the 3d transition metals as these are the materials most commonly studied in this thesis. The  $L_{2,3}$  absorption edges are defined as the energies for which transitions from the spin-split 2p core states to the vacant spin-split 3d states above the Fermi level ( $E_F$ ) occur. It is then clear that the absorption of x-rays by a 3d transition metal will be determined by two properties of the metal: the occupation of the 2p density of states (initial states), and the density of states of the unoccupied 3d states that lie above the Fermi level (final states)<sup>27</sup>. It is therefore instructive to look at the key properties of these initial and final states.

Firstly there are the spin-split 2p core states, where the presence of the spin-orbit interaction results in the formation of a pair of well separated 2p sub-bands<sup>27</sup>, the  $2p_{3/2}$  and the  $2p_{1/2}$  sub-bands which contain different numbers of electrons. The subscript gives the value of the total angular momentum quantum number,  $J$ , which is a good quantum number for such a system. The other good quantum numbers are the z-component total angular momentum number  $J_z$ , the spin quantum number  $s$ , and the orbital quantum number  $l$ . The difference in the occupation of the 2p sub bands is shown in schematic form in Fig. 2.5.1 below.

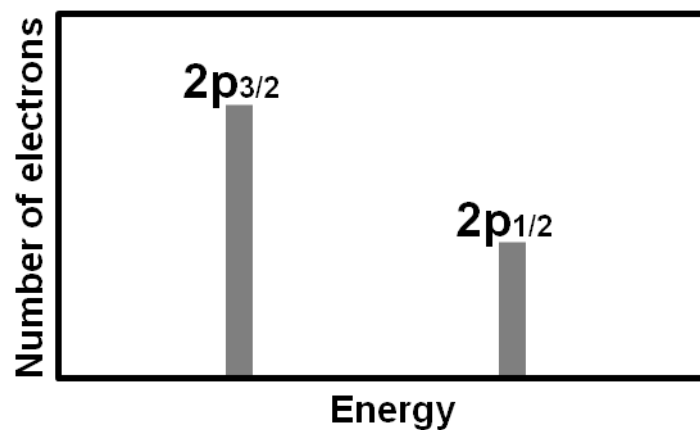


FIG. 2.5.1. A schematic showing the occupation of the spin-split 2p core states for the case of the 3d transition metals.

Next the density of states around the Fermi level must be considered. A schematic illustrating the key features for a hypothetical 3d transition metal is shown overleaf.

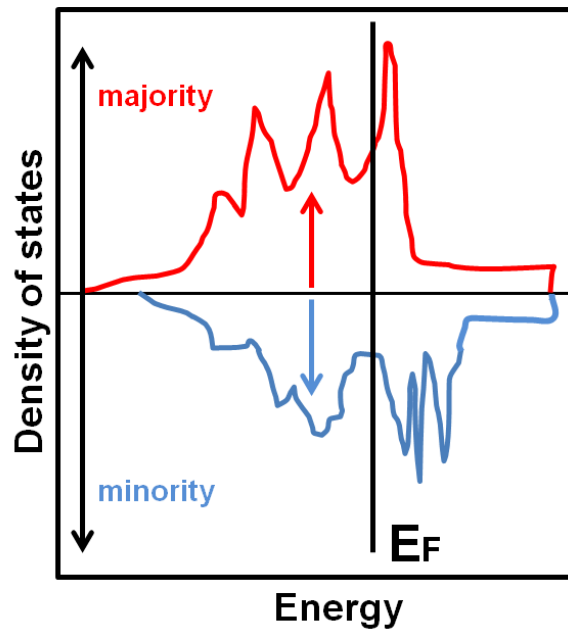


FIG. 2.5.2. A schematic illustrating the key features of the spin resolved density of states for a hypothetical 3d transition metal. There is difference in the occupation of the two possible spin states at the Fermi level. This results in the system having a net spin polarisation. The states showing strong energy dependence are of d character whereas those showing a flat energy dependence are of s,p character. The magnetic moment in the 3d transition metal ferromagnets comes chiefly from the d states.

There are several key features in Fig. 2.5.2. that should be highlighted. Firstly, the relatively flat energy dependence of the density of states that are of predominantly s and p character, where the use of “predominantly” acknowledges the presence of hybridisation. This is then in stark contrast to the density of states of the states that have predominately d character, chiefly responsible for the formation of the magnetic moment, for which sudden increases in the density of states are seen in the vicinity of the Fermi level. Secondly, the vacant states have a net spin polarisation.

An X-ray Absorption Spectrum (XAS) can then be obtained by taking the convolution of the initial and final states<sup>27</sup>, whilst also factoring in artefacts due to the energy resolution of the x-ray pulse (<1 eV for the studies presented in this thesis). The XAS lineshape and the energy range will be material specific. The XAS spectrum<sup>25</sup> of Ni is shown in Fig. 2.5.3.

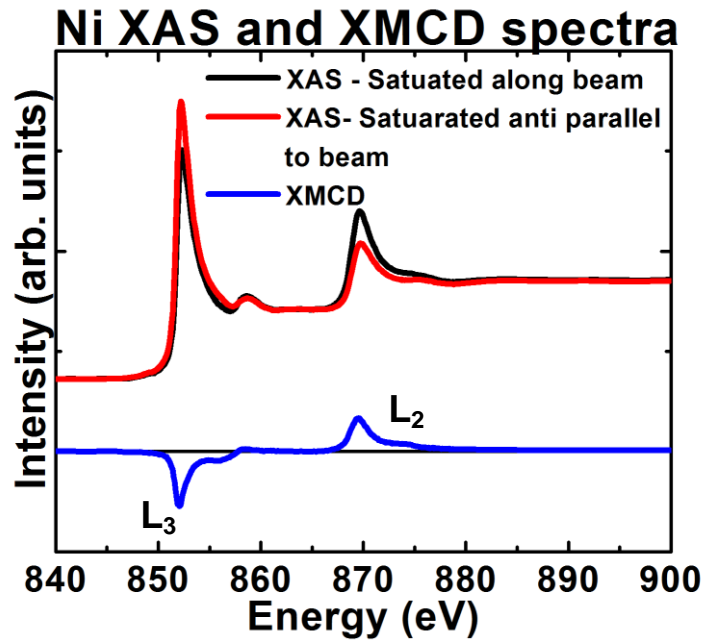


FIG. 2.5.3. An example XAS spectrum from Ni. The photon helicity is fixed and the saturation direction flipped along the beam axis. The resulting difference spectrum (XMCD spectrum) contains information about the spin and orbital components of the magnetisation.

The red and black curves in Fig. 2.5.3 are examples of Ni XAS spectra. Two well defined peaks are seen to be superimposed on top of a flat step-like background. The two peaks result from the resonant absorption of x-rays of sufficient energy to promote electrons from the 2p core states to vacant 3d states. That there are peaks for these transitions is a direct consequence of the sharp changes in the density of states for states of d character<sup>27</sup>. The step-like background which exhibits no strong energy dependence results from the promotion of electrons from the 2p core states to unoccupied states of predominately s,p character. Again the resulting shape stems from the shape of the unoccupied density of states.

It is then interesting to note that the 3d band is split by  $\sim 1$  eV by the exchange interaction which partially lifts the degeneracy of states in the 3d band, giving rise to a net spin polarisation. One must also consider the role of the excitation, namely the circularly polarised x-ray photon, the transfer of whose angular momentum to the excited valence electron is necessary to excite a  $2p \rightarrow 3d$  transition. The L edges are subject to selection rules<sup>28</sup> which govern the allowed transitions and the circularly polarised x-ray photon transfers its angular momentum to the orbital component of the valence electron momentum, so the transitions are spin conserving. As a result of all of

the above factors one sees a difference in absorption for left and right circularly polarised light – XMCD. The number of excited transitions is dependent on the projection of the spin in the transition metal onto the x-ray wave vector. The largest difference in absorption will then be seen when the two aforementioned vectors are changed from parallel to anti-parallel alignment, or vice versa, with an XAS spectrum taken for each alignment. This can be done by fixing the saturation direction of the magnetisation and flipping the photon helicity or by fixing the photon helicity and flipping the direction of saturation. For the data in Fig. 2.5.3. the later procedure was used. By subtracting the pair of XAS spectra one then arrives at a non-zero difference curve (blue curve Fig. 2.5.3.) known as an XMCD spectrum. The two peaks in the XMCD spectrum occur at the resonant energies of the transitions between the 2p core states and the unoccupied 3d states. Whilst the calculation of the transition probabilities between the initial and final states is beyond the scope of this chapter, some insight can be gained from the graphical representation of the transition probabilities given below in Fig. 2.5.4. for the case of left circular polarised light ( $l = +1$ ).

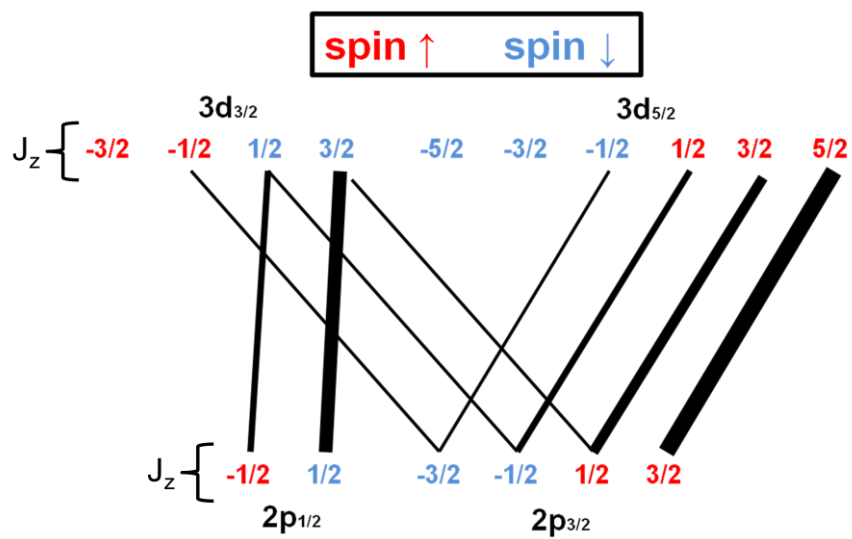


Fig. 2.5.4. The probabilities of the  $2p \rightarrow 3d$  transitions are shown in schematic form for the case of left circular polarised light ( $l = +1$ ) and the values of the total angular momentum magnetic moment given. The thickness of the lines from initial to final states represent the transition probability, the thicker the line the more likely the transition. The transitions from the 2p sub-bands are spin dependent.

The energy at which the  $2p_{1/2} \rightarrow 3d$  transitions have maximum probability is known as the  $L_2$  edge and the energy at which the  $2p_{3/2} \rightarrow 3d$  transitions have maximum probability is known as the  $L_3$  edge. Theoretical studies have concentrated on using the

XMCD spectrum to calculate absolute values for constituent spin and orbital parts of the magnetisation. This has resulted in a set of equations known as the XMCD sum rules that allow the user to estimate values for the spin and orbital moments. While this is a major motivation for many studies using the XMCD effect, it is not so for most of the work presented in this thesis where XMCD effect is utilised to make Ferromagnetic Resonance (FMR) measurements with element specificity. For this reason the sum rules are dealt with briefly below and the reader is referred elsewhere<sup>29, 30, 31</sup> for further details on the underlying theory.

To calculate absolute values for the spin and orbital moments it is necessary to know the number of 3d holes – itself an involved problem which has not yet been fully resolved in the literature. As the number of 3d holes appears in the sum rules for both spin and orbital moments, its calculation can be circumvented by estimating the ratio of the spin and orbital moments. Dropping the higher order dipole term in the spin sum rule, results in a sum rule of the form

$$\frac{m_{\text{orbital}}}{m_{\text{spin}}} = \frac{2q}{9p-6q} \quad (2.5.1)$$

where  $p$  is the value of the integral of the  $L_3$  peak in the XMCD spectrum, and  $q$  is the value to which the integral converges after the  $L_{2,3}$  edges of the XMCD spectrum have been integrated, as shown below in Fig. 2.5.5.

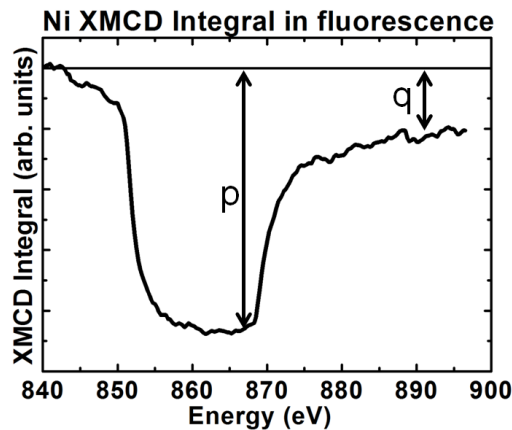


Fig. 2.5.5. The integral of a Ni XMCD spectrum obtained in fluorescence yield is shown marked with the values of the integral that enter into equation 2.5.1.

Equation 2.5.1. was applied in chapter 4 where the limitations of the approach are discussed alongside the experimental data.

## 2.6 Magneto Optical Kerr Effect (MOKE)

The Magneto Optical Kerr Effect (MOKE) is one of the phenomena most commonly utilised for the study of magnetic materials. When purely s- or p-polarised light is reflected from a non-magnetic material the polarisation state of the light will be unchanged. This is not so however, if s- or p-polarised light is reflected from a magnetic material. In this case the reflected light will be elliptically polarised such that the major axis of the ellipse is rotated with respect to the direction of polarisation of the linearly polarised incident light. This can be explained by picturing the spin-orbit interaction in the magnetic material as an effective magnetic field that reorients the axis of oscillation of the radiating dipoles within said material. Further insight can also be gained by considering the general form of the complex Fresnel coefficients at the air-magnetic material interface<sup>32</sup>.

$$r_{ss} = \frac{n_0 \cos \theta_0 - n_1 \cos \theta_1}{n_0 \cos \theta_0 + n_1 \cos \theta_1} \quad (2.6.1)$$

$$r_{pp} = \frac{n_1 \cos \theta_0 - n_0 \cos \theta_1}{n_1 \cos \theta_0 + n_0 \cos \theta_1} + \frac{2iQn_1n_0 \cos \theta_0 \sin \theta_1 m_y}{(n_1 \cos \theta_0 + n_0 \cos \theta_1)^2} \quad (2.6.2)$$

$$r_{ps} = \frac{iQn_0n_1 \cos \theta_0 (\sin \theta_1 m_x - \cos \theta_1 m_z)}{\cos \theta_1 (n_0 \cos \theta_0 + n_1 \cos \theta_1) (n_1 \cos \theta_0 + n_0 \cos \theta_1)} \quad (2.6.3)$$

$$r_{sp} = \frac{iQn_0n_1 \cos \theta_0 (\sin \theta_1 m_x + \cos \theta_1 m_z)}{\cos \theta_1 (n_0 \cos \theta_0 + n_1 \cos \theta_1) (n_1 \cos \theta_0 + n_0 \cos \theta_1)} \quad (2.6.4)$$

where  $\theta_0$  and  $\theta_1$  are the angle of incidence and angle of refraction respectively, as defined below in Fig. 2.6.1.  $n_0$ , is the refractive index of the air and  $n_1$  that of the magnetic material.  $Q$  is the Voigt constant and higher order terms in  $Q$  have been neglected. The coordinate system used is shown below in Fig. 2.6.1.

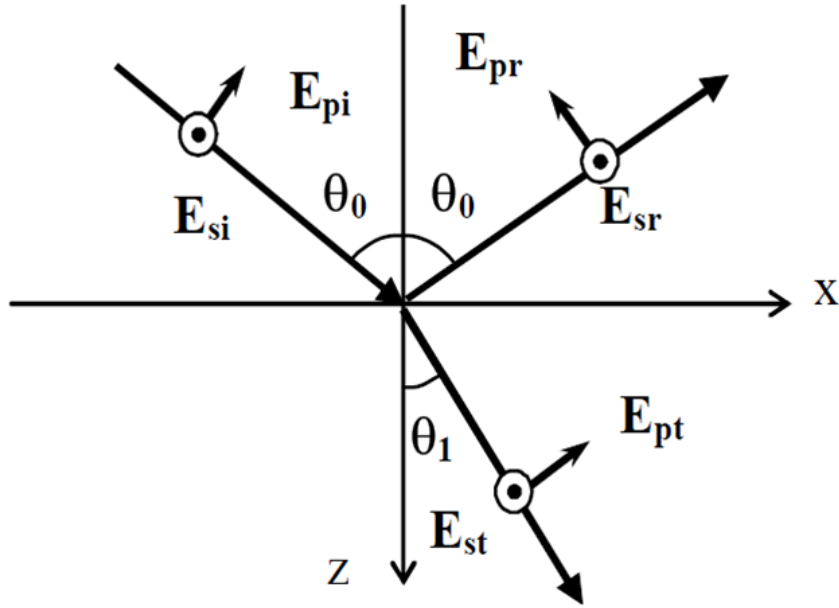


FIG. 2.6.1 The geometry used to define the terms used in the equations for the Fresnel coefficients at the air – magnetic material interface (equations 2.6.1 – 2.6.4). The z-axis lies normal to the interface and the x-axis lies parallel to the interface. The y-axis is out-of-plane. (Taken from reference 32).

The most striking aspect of equations (2.6.1 – 2.6.4) is that the coefficients  $r_{sp}$  and  $r_{ps}$  are non zero, meaning that some portion of s- or p-polarised light will be converted into p- or s-polarised light upon reflection from a magnetic material. That the coefficients  $r_{ss}$  and  $r_{pp}$  are not equal is also interesting as that tells us that only for the special case where the linearly polarised incident light is s- or p-polarised will the reflected light have the same polarisation, this is true even for the case of a non magnetic material. This is why s- or p-polarised light is used in magneto optical experiments. With reference to the Fresnel coefficients listed above, for the case of p-polarised incident light one can then define the Kerr rotation

$$\theta_K = -\text{Re} \left\{ \frac{r_{sp}}{r_{pp}} \right\} \quad (2.6.5)$$

and the ellipticity as

$$\eta_K = \text{Im} \left\{ \frac{r_{sp}}{r_{pp}} \right\} \quad (2.6.6)$$

respectively.

There are three geometries in which the MOKE can be measured: the longitudinal geometry, in which the component of the magnetisation that lies in the plane of incidence and plane of the sample is detected; the polar geometry, in which the component of the magnetisation that lies out of the plane of the sample and in the plane of incidence is detected; and the transverse geometry, in which a change in intensity rather than a Kerr rotation is observed, where the component of the magnetisation in the plane of the sample and normal to the plane of incidence is detected. Only p-polarised light can be used in the transverse geometry. In each case the measured effect is dependent on the angle of incidence and the wavelength of the incident light.

## Chapter 3: Experimental development

The purpose of this chapter is to detail the instrumentation employed in a variety of phase-resolved techniques that have been used during this PhD project.

A phase-resolved FMR setup that utilises the XMCD effect to make measurements with chemical specificity - XFMR - has been developed and is detailed in this chapter. To support the XFMR studies it was necessary to develop low temperature TR-MOKE and phase-resolved VNA-FMR setups, both of which are detailed in this chapter. Finally, a TR-XPEEM setup that utilises the XMCD effect to take images with magnetic contrast has been developed and is detailed in this chapter.

### 3.1 Experimental development of phase-resolved XFMR in fluorescence

This section will detail the experimental setup that has been developed to combine the chemical and site specificity of X-ray Magnetic Circular Dichroism (XMCD) with phase-resolved Ferromagnetic Resonance (FMR), resulting in a technique known as X-ray Ferromagnetic Resonance (XFMR). The XMCD signal scales as the scalar product of the x-ray wave vector and the magnetisation. The XFMR<sup>25</sup> setup detailed within this chapter exploits the inherent timing structure of synchrotron radiation to make phase-resolved measurements of magnetisation precession in ferromagnetic thin film samples with a resolution of  $\sim 1$  ps.

Precessional dynamics are exploited in the operation of high frequency magnetic devices such as magnetic disk drives, non-reciprocal microwave devices, and spin transfer oscillators. Such systems have already received extensive study by well established measurement techniques such as Time Resolved Scanning Kerr Microscopy<sup>33,34</sup> (TRSKM) and Brillouin Light Scattering<sup>35,36</sup> (BLS). The XFMR technique has an advantage over the aforementioned techniques in that it allows for the chemical and site specific measurement of magnetisation dynamics by means of XMCD. New insight may then be obtained by isolating the precession of different chemical species or at distinct sites in the crystal structure of a chosen material.

Previous XFMR studies can be divided into two distinct categories; phase-resolved measurements<sup>37,38,39</sup> and time-averaged measurements<sup>40,41,42</sup>. Both types of measurements are generally performed in transmission, although an earlier phase resolved study was performed in reflection at grazing incidence<sup>43</sup>. Transmission measurements are usually limited to samples grown on substrates such as  $\text{Si}_3\text{N}_4$  that are transparent in the soft x-ray regime and can be very fragile. For this reason an XFMR setup that can be used to make phase resolved measurements on samples on substrates which are opaque in the soft x-ray regime has been developed. This prevents measurement of transmission through the sample stack and leaves a choice between either measuring the photoelectrons emitted from the sample surface or the concurrent x-ray fluorescence. As the path of the photoelectrons will be strongly dependent on magnetic field one must instead measure the x-ray fluorescence that is emitted from the sample when an excited photoelectron falls back down to the 2p core states from the Fermi level for the case of the 3d transition metals.

To enable phase-resolved measurements to be made the experimental geometry shown in schematic form in Fig. 3.1.1 was adopted.

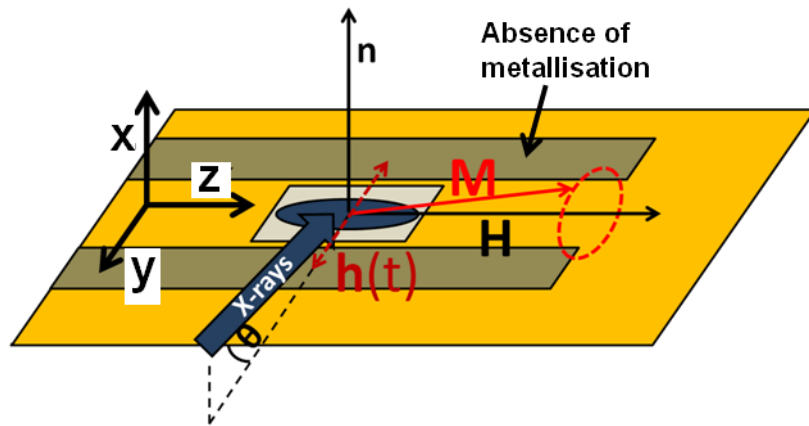


FIG.3.1.1. The experimental geometry for phase-resolved XFMR. The magnetization  $\mathbf{M}$  is forced into a state of steady precession about the applied bias field  $\mathbf{H}$  by an in-plane Radio Frequency (RF) magnetic field  $\mathbf{h}(t)$ . The x-rays are incident at a shallow grazing angle to detect the in-plane phase dependent component of the magnetisation.

A bias field,  $\mathbf{H}$ , is applied to saturate the magnetisation perpendicular to the plane of incidence, along the z-direction. A Radio Frequency (RF) magnetic field,  $\mathbf{h}(t)$ , lies perpendicular to the waveguide and in the plane of the sample. The RF field forces the magnetisation to precess about the effective internal field. The XMCD signal is

proportional to the component of the magnetisation along the x-ray wave vector. This then allows an XMCD signal to be recovered from the in-plane phase dependent y-component of the magnetisation at a fixed x-ray helicity, as well as a smaller projection onto the x-component. The signal is recovered by means of audio frequency lock-in detection. If for example square wave amplitude modulation is used then the RF excitation is being turned on and off periodically at a specific audio frequency. This means the lock-in amplifier measures the difference in the x-ray absorption between the magnetisation lying along the equilibrium direction and a chosen point on the precessional cycle. Static measurements (X-ray Absorption Spectra (XAS)) were made on the same device by fixing the x-ray helicity and saturating the magnetisation along both y-directions in turn. Due to the strong out-of-plane demagnetising field and the shallow grazing angle this is virtually the same as saturating parallel and anti-parallel to the x-ray wave vector. All measurements were performed in vacuum (of the order  $10^{-7}$  mbar) as the soft x-ray probe is strongly attenuated in air due to absorption by water molecules.

To generate an RF magnetic field the samples were fabricated on integrated Coplanar Waveguide (CPW) structures. A scale drawing of the device is shown below in Fig. 3.1.2.

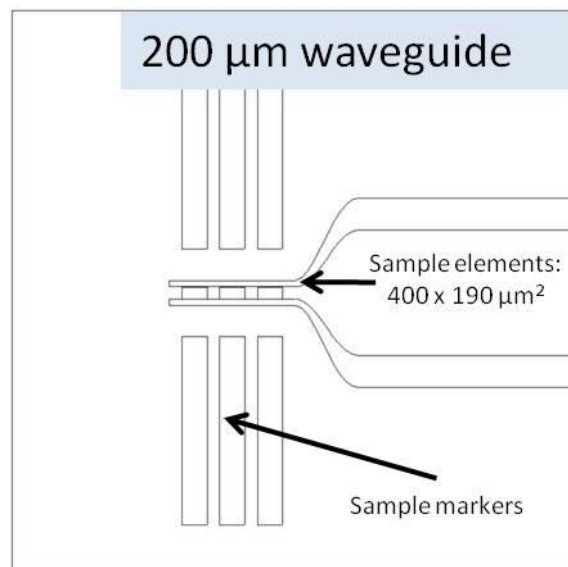


FIG. 3.1.2. A scale drawing of the devices used to make XFMR measurements. Sample elements are fabricated on the central track of a Coplanar Waveguide (CPW) of  $50 \Omega$  characteristic impedance.

The sample devices were fabricated at the Hitachi Global Storage Technologies San Jose Research Centre. A multilayer stack of the form; Ta(5)/[Cu(25)/Ta(3)]<sub>3</sub>/Magnetic Material/Cap (thicknesses in nm) was magnetron sputtered onto an insulating sapphire wafer of 500  $\mu\text{m}$  thickness. Sapphire was chosen as the substrate material as it has a suitably low loss characteristic at frequencies of several GHz (Dielectric constant at 10 GHz  $\sim 10$ ). The sapphire was chosen to be suitably thick so that penetration of the evanescent electric field through the back surface of the substrate was negligible. The purpose of the Ta/Cu multilayer is to produce a smooth underlayer in which to define the CPW. The waveguide and samples were defined in the wafer stack by a two stage masking process. Elements with lateral dimensions of 190  $\mu\text{m}$  x 400  $\mu\text{m}$  were formed on the thick Cu underlayer by electron-beam lithography and ion beam milling. The aspect ratio of the elements is sufficient to avoid any sizable inhomogeneous dynamics due to edge effects. Photolithography was then used to pattern the exposed Cu into a CPW structure of 50  $\Omega$  characteristic impedance and 200  $\mu\text{m}$  central track width. The CPW was shorted at one end to produce a current antinode at the position of the short so as to guarantee a non-zero RF magnetic field amplitude at the sample position. A 5  $\mu\text{m}$  border was left between the edge of the samples and the edge of the central track to avoid any sizable out-of-plane excitation. Multiple samples elements were fabricated on a given CPW in case of surface damage due to the intense x-ray pulses. This is important as after several days of x-ray irradiation the sample surface was observed to be heavily blackened. It is believed that this discolouration is due to carbonisation of residual acetone that was not removed by Isopropanol (IPA) during cleaning of the sample surface prior to measurement. No evidence of signal degradation was found. Markers consisting of the same magnetic material were added to the ground planes to facilitate landing the x-ray spot on a chosen sample element.

When deciding the size of CPW there are several factors that need to be taken into account. Firstly the width of the central track of the CPW determines the size of the RF magnetic field that will be generated by a given RF current propagating in the CPW. The RF magnetic field amplitude scales linearly with the current density. Reducing the central track width would allow for the excitation of larger in-plane cone angles for a given RF current, therefore producing a larger phase-dependent magnetisation component. However, the size and stability of the x-ray spot must also be considered. XFMR was performed on two different beamlines each having different sized x-ray spots. At I06 at the Diamond Light Source where the XFMR measurements described in

this chapter were first developed the x-ray spot is highly elliptical, measuring  $\sim (200 \mu\text{m} \times 20 \mu\text{m})$ . At BL 4.0.2 at the Advanced Light Source (ALS) the x-ray spot is circular with a diameter of  $\sim 100 \mu\text{m}$ . The major axis of the elliptical spot at Diamond was parallel to the symmetry axis of the CPW. Due to the requirement that as much x-ray flux strikes the sample as possible so as to maximise the signal size, 500  $\mu\text{m}$  wide CPWs were originally used during the early stages of the experimental development. By increasing the spatial stability of the experiment it was later possible to use 200  $\mu\text{m}$  wide CPWs such as that shown above in Figure 3.1.2. It is noted that if the central track width is continuously reduced then eventually the current density will be large enough to cause significant Joule heating and that this may cause outgassing, increasing the pressure in the measurement chamber. Excessive heating of the sample could be countered by flooding the vacuum chamber with a low pressure inert exchange gas such as Nitrogen or Argon. No evidence of unwanted heating effects was observed during the studies presented in this thesis.

To realise the experimental geometry shown in Fig. 3.1.1, a bespoke sample holder, shown below in Figure 3.1.3, was designed and machined in Exeter.

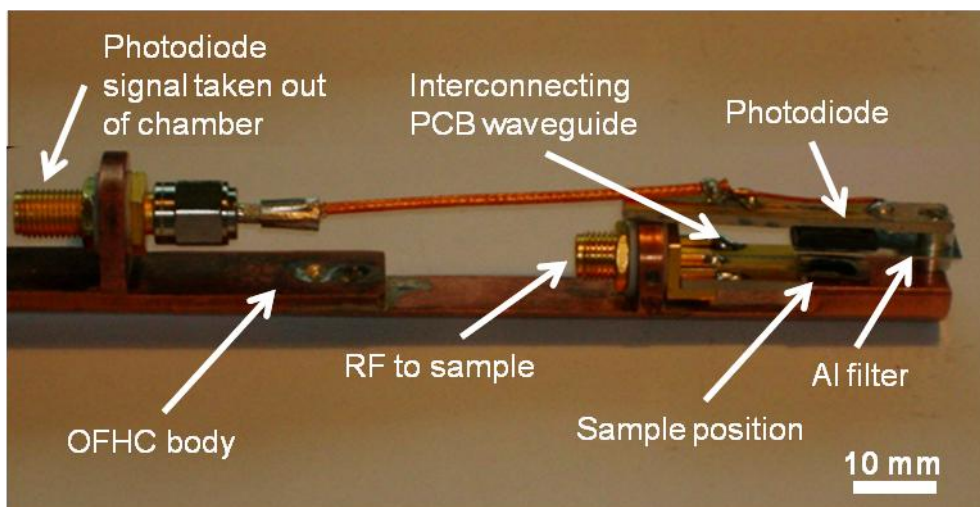


FIG. 3.1.3. A photograph of the sample holder used for XFMR experiments. It comprises a copper body, vacuum compatible SMA cabling, an interconnecting PCB waveguide and a large area UV photodiode. The photodiode faces the sample and measures the x-ray fluorescence. A thin film Al filter suspended between photodiode and sample blocks photoelectrons from striking the active area.

The sample stick body is milled from a rod of Oxygen Free High Conductivity (OFHC) copper. The RF excitation is passed along  $\sim 1 \text{ m}$  of low loss vacuum compatible SMA cable (Atlantic Microwave: ASF-086 semi-flexible cable) which then terminates onto an

SMA edge launcher (Digikey) that is bolted to a bulkhead on the copper body and electrically isolated from it with PTFE inserts. The edge launcher is vacuum soldered (Stay-Brite Silver Solder) to an interconnecting PCB CPW of 2 mm central track width (Trackwise) made from high frequency material (ARLON 1000, Dielectric constant of 10 at 10 GHz). Electrical connections were made between the interconnecting CPW and the sample CPW with Ag paint (Electrolube). The sample waveguide was held firmly in place by applying either Ag paint or Carbon tape (Ted Pella: Double coated Carbon Tape) to the backside of the sapphire substrate. A large area (5.5 mm diameter) UV photodiode (International Radiation Detectors: AXUV20A) was mounted on a PCB directly above the sample elements such that the sample surface and the photodiode's active area are separated by 3 – 4 mm. This allowed a maximum grazing angle of 25°. The active area of the photodiode occupied a solid angle of  $\sim \pi$  steradians. Typically measurements were performed with a 10° – 20° grazing angle. If photoelectrons were to strike the active area of the photodiode they would cause an unwanted field dependent background. To avoid this a 200 nm thick Al foil was suspended on a bespoke 0.25 mm thick Al frame (Lebow Company) in front of the photodiode's active area. A thickness of 200 nm was found to be sufficient to stop photoelectrons whilst still allowing the x-ray fluorescence to be measured. The frame fitted under the body of the photodiode and did not reduce the available range of grazing angles. The Al foil was deposited so as not to be taut to make it more robust and the frame did not create any trapped volume between it and the photodiode body. For early XFMR experiments the photodiode was mounted on a long PCB waveguide. This was then later replaced with a length of vacuum compatible SMA cable to reduce electrical pickup at the modulation frequency.

All XFMR measurements must be performed under vacuum due to the strong attenuation of soft x-rays in air. The vacuum systems used for all XFMR measurements shown in this thesis are the Portable Octupole Magnet System (POMS) on beamline I06 at the Diamond Light Source and the Vector Magnetometer (VMM) on beamline 4.0.2 at the ALS. Both are vacuum chambers capable of reaching vacuum of the order  $10^{-7}$  mbar and consist of a 6-way cross. The 6-way cross is then centred in an Octupole magnet allowing an external magnetic field of  $\sim 1$ T to be applied in any direction. SMA coaxial feedthroughs allow the RF excitation and photodiode signal to enter and exit the vacuum chamber respectively. Photographs of the POMS chamber set up on beamline I06 at Diamond are shown below.

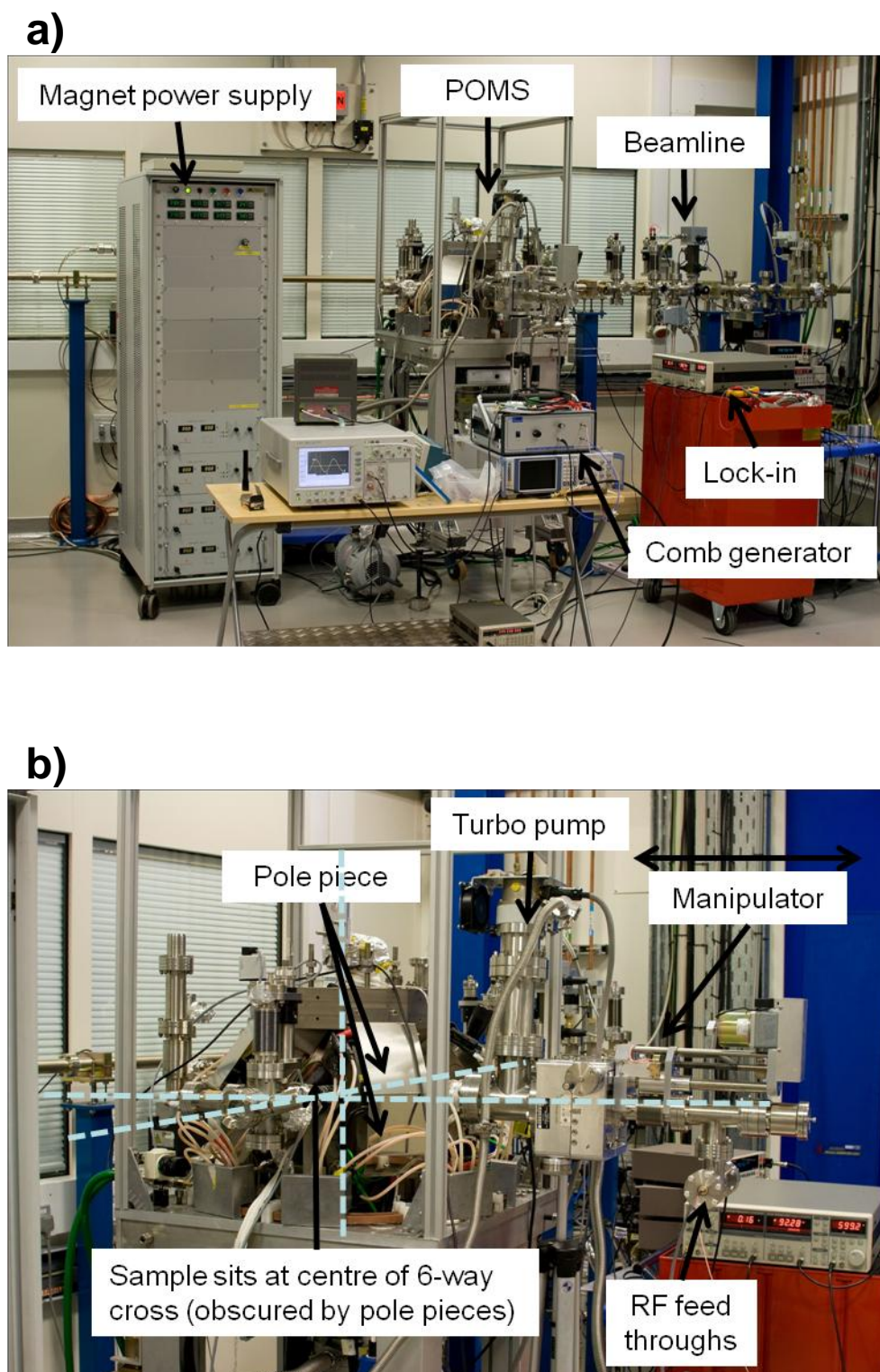


FIG. 3.1.4. (a) A photograph of the POMS set up on beamline I06 at Diamond. For best signal-to-noise ratio the lock-in amplifier and comb generator were separated by several metres. (b) A close up photograph of the POMS chamber. The dotted lines are guides to the eye for the 6-way cross around which the 8-pole magnet is assembled.

Since XFMR is a stroboscopic technique there must be a fixed phase relation between the pump and probe. This means that the RF excitation frequency must be an integer multiple of the repetition rate of the x-ray pulses. The repetition rate of the x-rays is governed by the temporal separation of neighbouring electron bunches in the synchrotron's storage ring ( $\sim 2$  ns) and is controlled by the master oscillator of the synchrotron. This means that the RF excitation must be derived from the master oscillator. It should be noted that the repetition rate of the x-rays is not exactly 500 MHz, but instead 499.99 MHz (2 dp) for both Diamond and the ALS. Microwave synthesisers typically phase lock to a 10 MHz input with a tolerance of  $\pm 3$  ppm, this meant that it was not possible to divide the master oscillator signal by 50 and use it to drive a microwave synthesiser. Instead a custom made comb generator system was designed in conjunction with Atlantic Microwave. The comb generator takes the master oscillator signal as an input and outputs a frequency that is a phase locked integer multiple of the input frequency. The input is turned into a frequency comb by a Step Recovery Diode (SRD). Each tooth in the comb is an integer multiple of the input frequency. The frequency comb is then passed to a fixed filter bank allowing the user to manually select an output frequency of; 4, 5, 6, 7, 8 or 10 GHz on the comb generator front panel. The output power for all frequencies is nominally +25 dBm. The x-ray pulse FWHM at Diamond and the ALS were found to be 30 ps and 70 ps respectively. At the ALS it was found that it was not possible to measure dynamics with RF excitation frequencies  $> 4$  GHz. No such limitation was found at Diamond with measurements up to 7 GHz proving successful. The chosen output RF signal from the comb generator is then passed to a programmable mechanical delay line capable of 0.5 ps step resolution (Colby Instruments PDL-100A). This allows the pump-probe delay to be adjusted by delaying the excitation relative to the pump. Although the insertion loss per nanosecond of delay is low ( $< 1$  dB), the order of the comb and delay generators can be reversed to avoid reducing the RF output. High frequency SMA cabling then takes the RF signal into the chamber via an SMA coaxial feedthrough. The timing jitter on the RF output from the comb generator is approximately 1 ps meaning that the phase of the comb generator output accurately follows the phase of its input. A block diagram in Fig. 3.1.5. (a) shows the RF equipment involved in the XFMR measurement setup.

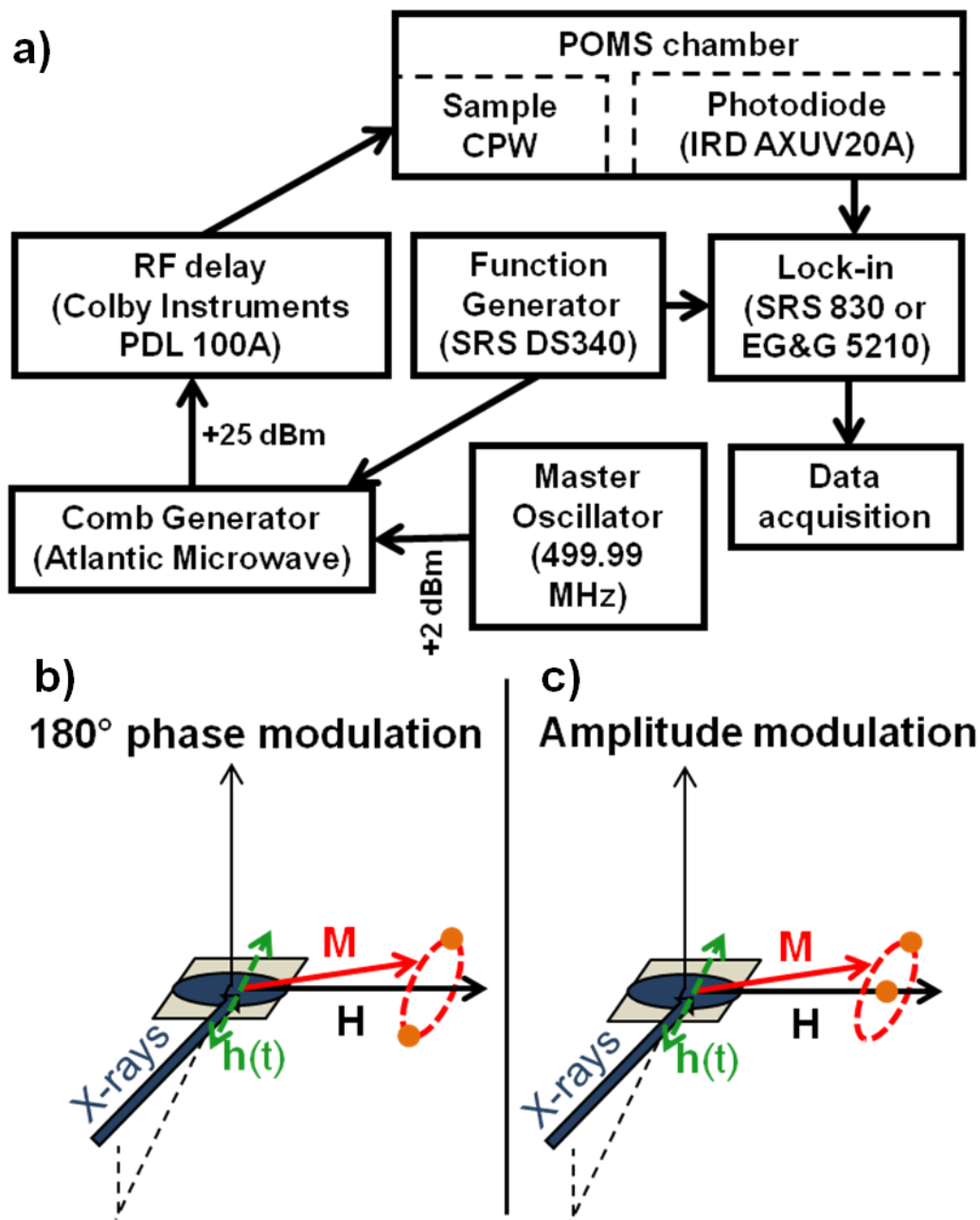


FIG. 3.1.5. (a) A block diagram of the RF equipment used for XFMR measurements. A fixed phase relationship between pump and probe is obtained by using a custom comb generator system that accepts the synchrotron master oscillator as its input. The pump-probe delay is adjusted with a programmable delay generator and the photodiode signal is recovered by audio frequency lock-in detection. (b) Schematic of the principle of 180° phase modulation – the lock-in amplifier measures the difference between the two orange dots on the precession cycle. (c) Schematic of the principle of amplitude modulation. The lock-in amplifier measures the difference between the orange dot on the precession cycle and the orange dot that represents the equilibrium direction.

The RF excitation can be either amplitude or 180° phase modulated at audio frequencies to facilitate lock-in detection. The comb generator system has an integrated amplitude modulator which accepts audio frequency square wave voltages in the range 0 – 5 V.

Here amplitude modulation results in the RF output of the comb generator, and therefore the precession of the magnetisation, being turned on and off periodically. The lock-in amplifier then measures the difference in x-ray absorption between the magnetisation saturated along the applied field direction and the selected point on the precession cycle. This allows an XMCD signal to be obtained with a fixed x-ray helicity. If instead 180° phase modulation is used then the lock-in amplifier will detect the difference signal between two points 180° apart on the precessional orbit. Phase modulation of the comb generator output is achieved by first splitting the master clock signal in two (Atlantic Microwave: BPD 2-way power divider). The two signals are then sent along separate propagation paths with a difference in length that can be precisely tuned by means of a manually operated line stretcher (Atlantic Microwave: AS5677 phase shifter) to induce a  $\pi$  phase shift. The two signals are then passed to the inputs of a single pole double throw PIN diode switch (Atlantic Microwave: APS 2002-A pin diode switch). The PIN diode switch has two inputs and a single output which is then connected to the input of the comb generator. By gating the PIN diode at a chosen audio frequency the switch will then switch periodically between its two different pole positions. Since the output of the comb generator system is phased locked to its input, the phase of the RF output is being modulated by 180 degrees. It was found that phase modulation reduces the DC offset on the lock-in amplifier which then allows the dynamic signal to occupy a greater portion of the input range of the lock-in amplifier. It also increases the signal size by a factor of 2. For all experiments a Stanford Research Systems DS 340 arbitrary function generator was used to provide the modulation frequency which was passed to the reference input of the lock-in amplifier (SRS 830 or EG&G 5210). A modulation frequency of ~ 111 Hz was generally found to give the lowest observed background on the lock-in front panel (generally in the range 40 fA – 400 fA). However the optimal reference frequency could change from beamtime to beamtime and so this was the subject of investigation during the initial setup period. Results obtained during this PhD project from XFMR with fluorescence detection are detailed in chapters 4- 6.

### **3.2 Experimental development of phase-resolved XFMR in luminescence**

In addition to developing phase resolved XFMR in fluorescence yield this PhD project has also led to the subsequent development of phase-resolved XFMR in luminescence

where the aim was to make transmission style measurements on samples on substrates that are opaque in the soft x-ray regime. It may then be possible to apply the XMCD sum rules, something which is complicated when measuring in fluorescence due to the presence of self-absorption effects. The incident x-ray beam is partially absorbed in the magnetic sample with the remainder propagating into the Cu under layer and eventually being strongly absorbed in the sapphire substrate. The absorption of the x-rays in the sapphire results in luminescence that is transmitted through the back surface of the substrate and it is this yield that is detected. Whilst the RF equipment remains the same as for the fluorescence setup, it was necessary to design a new sample holder to allow the luminescence from the back surface of the substrate to be measured. A photograph of the luminescence sample stick is shown below in Fig. 3.2.1.

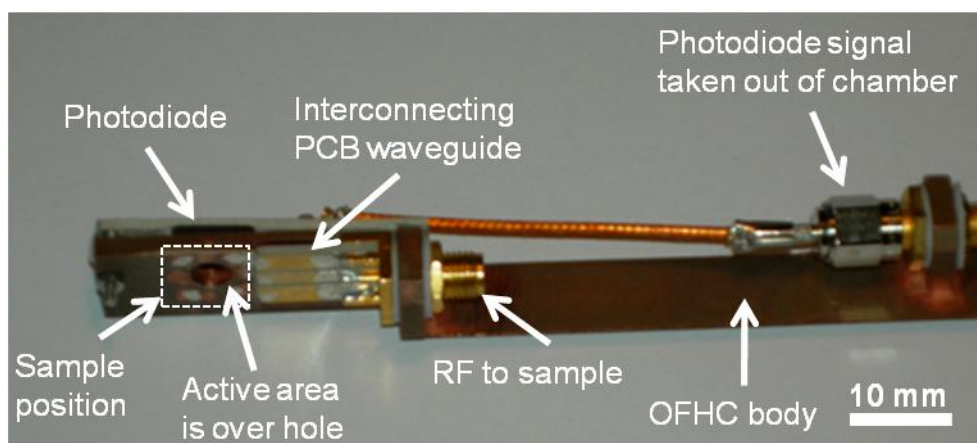


Fig. 3.2.1. A photograph of the sample stick used for XFMR experiments in luminescence yield. It comprises a Cu body, vacuum compatible SMA cabling, an interconnecting PCB waveguide and a large area UV photodiode. The photodiode sits facing the back surface of the sapphire substrate to measure the luminescence. The dashed white line highlights where the sample would be mounted.

The body of the luminescence sample stick was milled from a rod of OFHC copper. The RF pieces used to deliver the RF excitation to the sample waveguide are the same as those previously described for the fluorescence sample stick. The sample waveguide sits over a hole in the copper body with the photodiode fixed in place over the other side of the hole. This allows the luminescence from the back surface of the sapphire substrate to be detected by the photodiode. With nothing mounted above the sample surface there were no restrictions on the angle of incidence. As with the fluorescence setup the photodiode signal was taken out of the vacuum chamber with a length of vacuum SMA and passed to the current input of a lock-in amplifier. The principle of measuring the

phase dependent components of the magnetisation orthogonal to the external bias field in a stroboscopic fashion remained unchanged.

Results obtained during this PhD project with XFMR in luminescence are detailed in chapter 8.

### **3.3 Experimental development of phase-resolved VNA-FMR**

In addition to the development of XFMR during this PhD project it was necessary to develop several experiments based in Exeter to allow for thorough characterisation of samples of interest before making XFMR measurements. The first of these setups that will be described is phase-resolved Vector Network Analyzer Ferromagnetic Resonance (VNA-FMR). Phase-resolved VNA-FMR was developed to identify the resonance fields of a range of samples prior to XFMR measurements with a quick turn-around time. VNA-FMR is a frequency domain technique in which the frequency of the RF excitation is swept in the presence of a fixed bias field<sup>44</sup>.

A VNA is a piece of RF equipment that outputs an RF signal with frequency and power that can be swept. The RF signal is then passed to the Device Under Test (DUT) before returning to the VNA. The return signal is then compared to the original output signal. A VNA is essentially a combination of a microwave synthesiser and a lock-in amplifier that utilises phase sensitive detection to measure the amplitude and phase of the returning signal. For all measurements presented in this thesis an Agilent PNA-X series 5242 network analyzer was used. This is a two port instrument, where each port can act as an emitter, receiver or both concurrently. This allows for two possible measurement geometries to be realised. A reflection geometry is where a single port acts as both emitter (j) and receiver (i), whereas in a transmission geometry a second port acts as the receiver. By comparing the emitted signal with that received after interaction with the DUT the VNA is measuring the S- (or scattering) parameters ( $S_{ij}$ ) of the DUT. Denoting the ports as 1 and 2 gives  $S_{11}$  and  $S_{22}$  being acquired in a reflection geometry and  $S_{12}$  and  $S_{21}$  in a transmission geometry. Originally VNA-FMR measurements were made on samples on integrated waveguides similar to those used for XFMR that were shown above in Fig. 3.1.2. The samples measured in VNA-FMR and XFMR contained the same wafer stack. Diagrams of the devices used for VNA-FMR measurements and the position of the picoprobes are shown below in Fig. 3.3.1

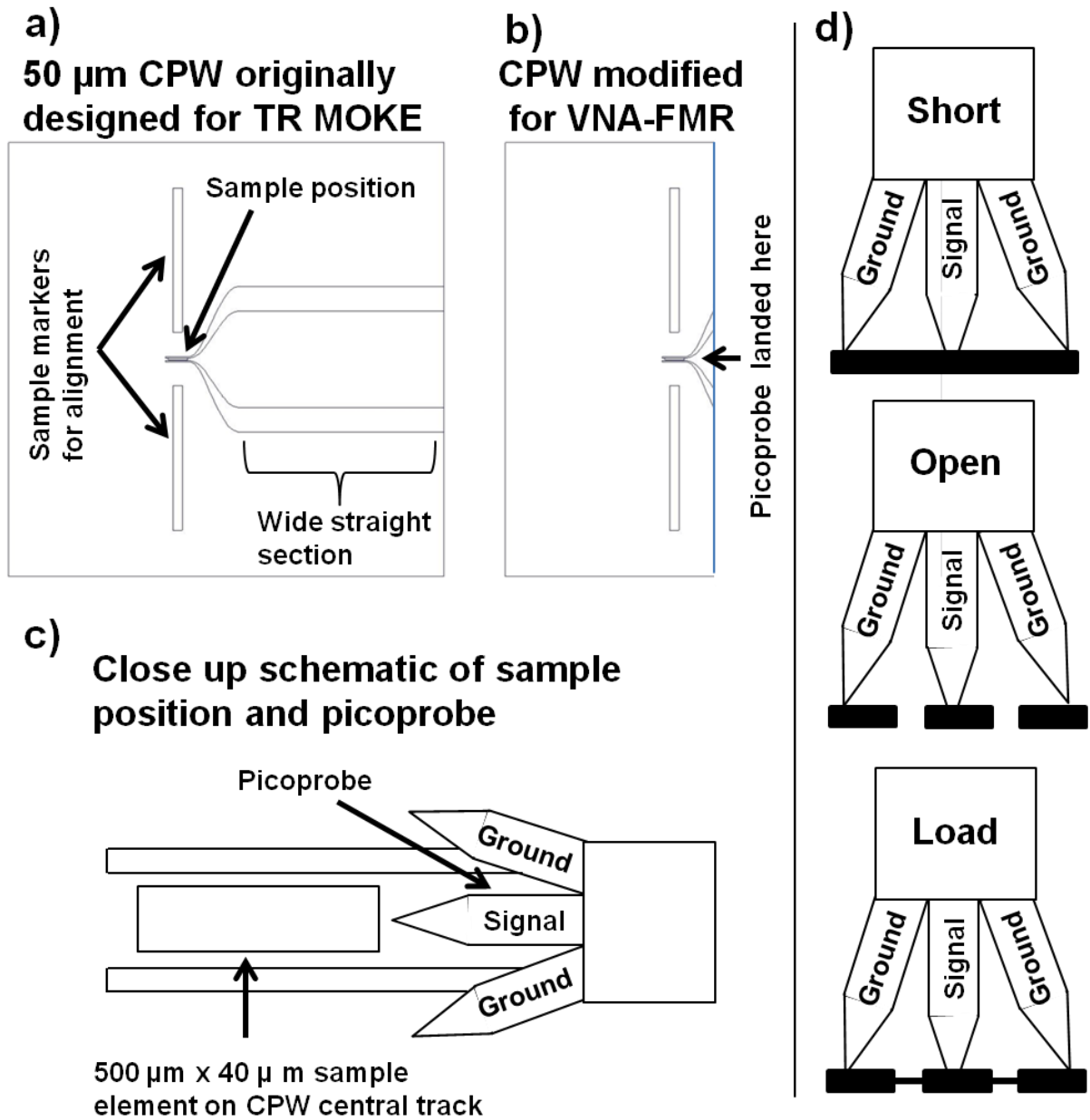


FIG. 3.3.1 (a) A scale drawing of the 50  $\mu\text{m}$  CPW devices originally designed for TR MOKE measurements that were later modified for use with VNA-FMR. (b) The devices were modified by removing the wide straight section shown in (a) to enable VNA-FMR measurements to be made. (c) A schematic of the high frequency microwave probes (picoprobes) used to make electrical connections to the sample CPW in VNA-FMR. (d) Schematics of the picoprobe landed on a short, open and 50  $\Omega$  load as part of a calibration.

VNA-FMR measurements were made on a CPW with 50  $\mu\text{m}$  central track width. The CPW was shorted at one end to generate a current anti node at the position of the short so as to guarantee a non zero RF magnetic field amplitude at the sample position as is the case for the devices used for XFMR measurements. The sample fills the majority of

the central track so as to provide a larger inductive signal for a given precessional cone angle.

High frequency microwave probes (GGB Industries, Inc. Model: 40 A, Mounting: DS-style) Fig. 3.3.1 (c) & Fig. 3.3.2 (b)) were connected to the RF cabling from the VNA and landed on the tapering region of the CPW. The reason picoprobes were landed on the sample CPW, rather than making electrical connections with Ag paint as in the XFMR setup described above, was to allow for the artefacts due to the RF cabling and interconnects to be calibrated out. The purpose of performing a calibration is to produce a correction factor that accounts for the frequency dependent losses in the RF cabling and interconnects connected between the sample CPW and the VNA. The method of calibration used for all work in this thesis is known as the Short Open Load Thru (SOLT) method. Here the user measures a well characterised short, open,  $50 \Omega$  load and if they are working in a transmission geometry a thru. Such devices are referred to as mechanical calibration standards and are screwed onto the end of the cabling assembly once it has been removed from the picoprobe. Each set of mechanical standards come with idealised data that is loaded onto the VNA before the calibration measurements are made. By comparison of the results from measurements made with the calibration standards with the idealised data the VNA is then able to generate a correction factor to account for the artefacts due to the RF cabling and interconnects. For the work shown in this thesis the Agilent 85052 D calibration set was used. The calibration should be performed over the range of excitation frequencies and powers at which the subsequent VNA-FMR measurements are to be performed. The drawback of calibrating using mechanical standards is that it does not allow the user to calibrate out the artefacts due to the picoprobe. In this case a calibration substrate (GGB Industries, Inc. – CS-5 calibration substrate) can be used in place of the mechanical standards. Rather than having a series of standards that screw onto the end of the cabling assembly a calibration substrate has thin film equivalents deposited onto an insulating sapphire substrate. The picoprobe can then be landed on each of the devices in turn (Fig. 3.3.1 (d)). This then allows both the RF cabling and the picoprobe to be calibrated. It is preferred to contact the sample CPW with a picoprobe rather than with Ag paint as the latter is harder to calibrate for. The devices used for VNA-FMR measurements were originally designed for TRSKM measurements in which an interconnecting PCB waveguide of 2 mm central track width is used to make the connection to the sample waveguide. It was found to be necessary to remove the wide straight section of the

CPW to facilitate VNA-FMR measurements, as shown above in the inset of Fig. 3.3.1 In chapter 4 it will be shown experimentally that the presence of the wide straight section heavily distorted the expected Lorentzian line shape of the FMR response when the picoprobe was landed on the tapering section of the CPW. No attempt was made to use a set of microwave probes of sufficiently large pitch so as to allow for landing on the wide straight section of the CPW.

To make VNA-FMR measurements the sample waveguides were positioned between the poles of a dipole electromagnet that was mounted on a rotatable ring. This allowed the magnet to be rotated manually by 360°. The stage upon which the sample CPW and picoprobes were mounted was mounted on an Aluminium post centred between the pole pieces of the electromagnet. This allowed an applied bias field of up to 2 kOe to be applied in the plane of the sample at any angle with respect to the symmetry axis of the sample CPW. The electromagnet and stage were inherited from an earlier Time-Resolved Scanning Kerr Microscopy (TRSKM) experiment that was developed in Exeter.

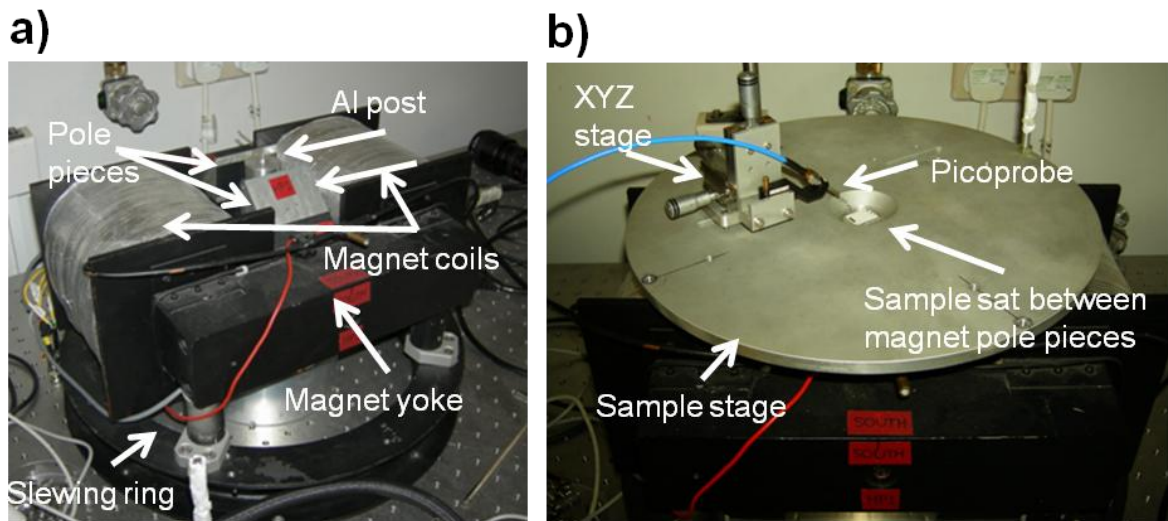


FIG. 3.3.2. Photographs of the experimental setup used to make VNA-FMR measurements. (a) The dipole electromagnet mounted on a slewing ring (stage removed). (b) The stage mounted above the electromagnet. A picoprobe is mounted on an X,Y,Z stage allowing it to be positioned onto the sample waveguide which sits in the depression in the stage so that it is between the pole pieces of the electromagnet.

The torque experienced by the sample magnetisation due to the RF magnetic field scales as  $\sin(\theta)$  where  $\theta$  is the angle between the RF and static magnetic fields. By mounting the electromagnet on a slewing ring so that it could rotate about the sample position it

was possible to take a background spectrum with the external bias field applied in-plane and orthogonal to the symmetry axis of the sample CPW. By subtracting this background spectrum from all measured spectra it was possible to remove sources of noise that are not removed through calibration down to the tip of the picoprobe alone. The process of removing non magnetic signal contributions is discussed in more detail in chapter 4. To allow the picoprobe to be landed accurately on either the calibration substrate or the sample CPW it was mounted on an X,Y,Z translation stage (Martock Design XYZ stage). The devices had lateral dimensions of the order 100  $\mu\text{m}$ . For this reason it was necessary to land the picoprobe whilst imaging with a Charged Coupled Device (CCD) camera with a x2 optical zoom lens attached.

In addition to the VNA-FMR setup outlined above two other VNA-FMR setups were also used. The first was an in-situ setup allowing measurements to be performed on the XFMR sample holder (Fig. 3.1.3) in the POMS vacuum system at Diamond. Whilst the frequency swept line shape was noisy due to the inability to calibrate the cabling assembly it was possible to measure approximate values for the resonance field. High quality data could be obtained by fixing the excitation frequency and sweeping the bias field. This meant it was possible to quickly verify the presence of a dynamic response before undertaking XFMR measurements. Secondly a first attempt at making VNA-FMR measurements in Exeter on coupon samples that are not directly deposited onto CPW structures was made and will be described briefly here. To make coupon measurements a PCB CPW made from high frequency board (ARLON 1000) of central track width 500  $\mu\text{m}$  was mounted onto a PTFE block and SMA edge launchers attached to either end of the CPW to allow transmission measurements to be made (Fig. 3.3.3). Glass coupons of lateral dimensions of the order 10 mm x 10 mm were overlaid onto the CPW so that the entire length of the 500  $\mu\text{m}$  wide central track was loaded with magnetic material. The purpose was to maximise the inductive signal generated for a given cone angle. The glass coupons were held in place with PTFE tape and the PTFE block was mounted on top of an Al post centred between the pole pieces of the electromagnet.

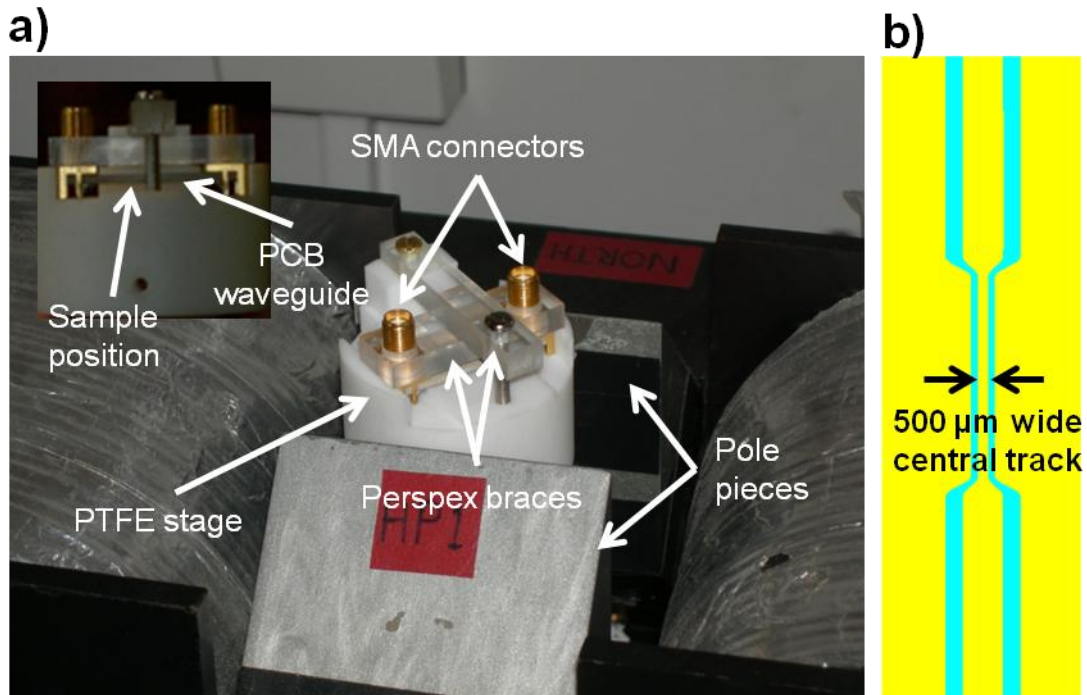


FIG. 3.3.3 (a) A photograph of the PTFE sample block used to make VNA-FMR measurements on coupons. The stage has been offset above the pole pieces for clarity. (Inset) A side view of the PTFE block. The electrical connections to the CPW are made by attaching an SMA edge launcher to each end for a transmission geometry. (b) Scale drawing of the PCB CPW made from high frequency board. The central track width is 500  $\mu\text{m}$ .

The CPW is held firmly in place by a combination of a tension fit with the PTFE body and a pair of Perspex braces which are screwed into the PTFE body. The metallisation on the glass coupon samples was electrically isolated from the CPW by either PTFE tape or photo resist spin coated onto the sample surface. Mechanical calibration standards were used to remove artefacts from the RF cabling assembly and for each measured spectrum a background spectrum, taken with the external bias field orientated in-plane orthogonal to the symmetry axis of the CPW, was subtracted.

The VNA-FMR results obtained during this PhD project are shown in chapter 4.

### 3.4 Experimental development of low temperature Time-Resolved MOKE

In addition to VNA-FMR it was necessary to develop a low temperature TR-MOKE experiment for thorough characterisation of selected samples before undertaking XFMR measurements. TR-MOKE experiments have been established in Exeter for over a decade but prior to this PhD project were only carried out at room temperature.

Upon interaction with a magnetic material, linearly polarised light becomes elliptically polarised due to the Magneto Optical Kerr Effect (MOKE). This can be explained by picturing the spin-orbit interaction in the magnetic sample as a magnetic field which re-orientates the the oscillating dipoles in the magnetic material that are responsible for the reflection of the laser light. By splitting the reflected beam into two beams of orthogonal linear polarisation and then measuring their respective intensities with seperate photodiodes it is possible to accurately measure the angle by which the linear polarisation of the reflected beam has rotated with respect to that of the incident laser beam – the Kerr rotation. A microwave generator is connected to samples on integrated CPWs and an ultrafast laser system used to probe the resulting magnetisation dynamics. The two are phase locked to one another allowing stroboscopic measurements to be made of the temporal evolution of the magnetisation dynamics.

The sample waveguide was mounted on an OFHC copper sample holder by applying Ag paint to the back of the sapphire substrate. Electrical connections were made to the sample CPW by Ag paint contacts to an interconnecting waveguide of 2 mm central track width. The interconnecting CPW was made from high frequency board (ARLON 1000).

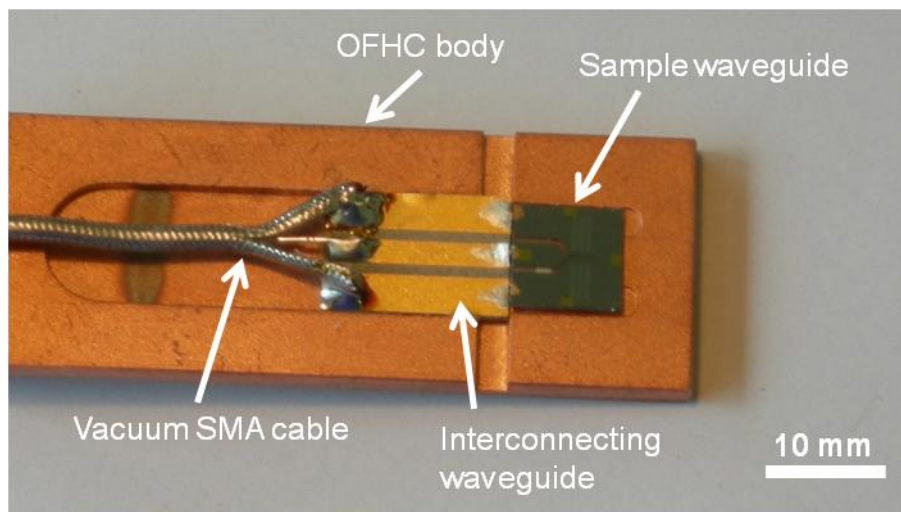


FIG. 3.4.1. A photograph of the OFHC sample holder used for low temperature TR-MOKE measurements. The sample CPW and interconnecting waveguide are mounted on the copper body which is then screwed onto the cold finger of the cryostat.

The OFHC sample holder was screwed onto the end of the cold finger of a He flow cryostat (Oxford Instruments Microstat He). The temperature was measured by a sensor

at the end of the cold finger. The sapphire substrate is an excellent thermal conductor and was in thermal contact with the OFHC sample holder. For this reason it was assumed that the measured temperature was equal to the sample temperature. A length of vacuum SMA cable (Atlantic Microwave: ASF-086 semi-flexible cable) entered the cryostat via an SMA feed through to supply the RF excitation. Due to spatial constraints inside the cryostat it was not possible to use an SMA edge launcher to connect the vacuum SMA cable to the interconnecting CPW and so it was vacuum soldered (Stay-Brite Silver Solder) directly onto the interconnecting waveguide. Normal incidence allowed the polar Kerr effect to be measured. Optical access was enabled by a low Verdet constant optical window, which minimised the Faraday rotation of the light in the windows. The window was located in the cryostat's tailpiece and was parallel to the sample surface. The symmetry axis of the sample CPW lay along the long axis of the tubular cryostat meaning that for FMR measurements to be made an external magnetic field had to be applied along the long axis of the cryostat. The realisation of this geometry is shown below in Fig. 3.4.2.

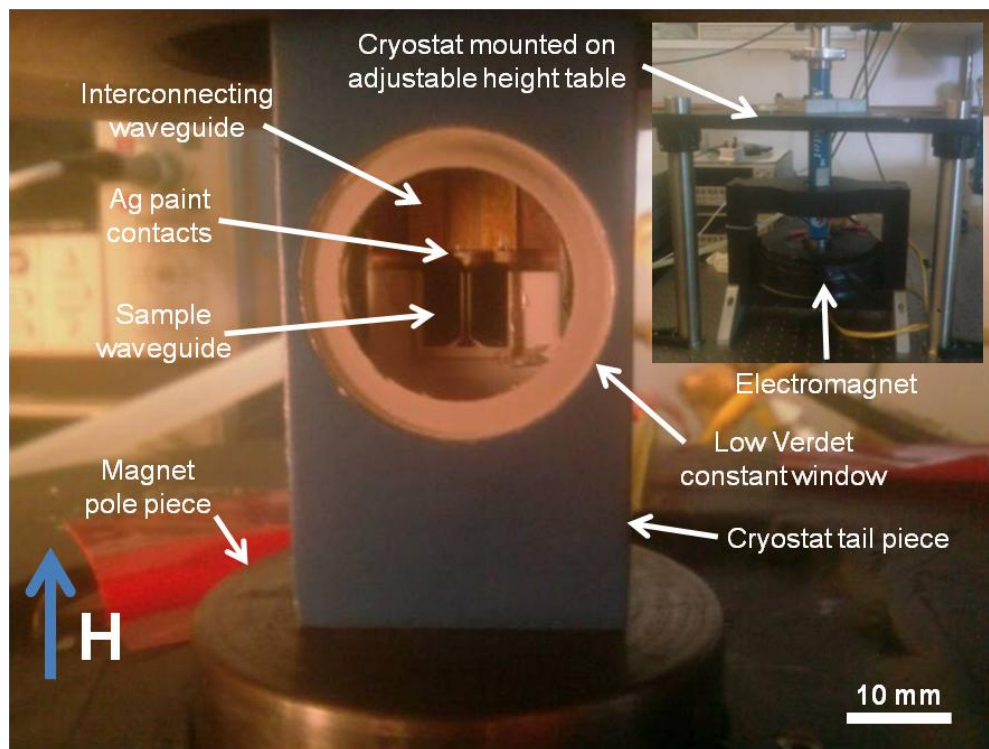


FIG. 3.4.2 Optical access at normal incidence is obtained through a low Verdet constant optical window allowing the polar Kerr effect to be measured. (Inset) Photograph of the experimental setup used to realise an FMR geometry in the He flow cryostat. The cryostat is mounted on a three legged variable height platform and is suspended through the yoke of an electromagnet.

The cryostat is suspended through a hole in the yoke of an electromagnet. The sample CPW was centred above the lower pole piece where the field has the highest degree of spatial uniformity. Despite the hole in the top plate, the magnetic circuit was sufficiently complete so as to allow a field of up to 1.7 kOe to be obtained. The height of the three legged table can be adjusted allowing the sample waveguide to be moved relative to the probe beam whilst keeping the working height of the beam constant. With a suitable FMR field geometry realised, the setup shown above in Fig. 3.4.2 was integrated into a stroboscopic pump-probe measurement setup based around an ultrafast pulsed laser to enable TR-MOKE measurements to be made at low temperature.

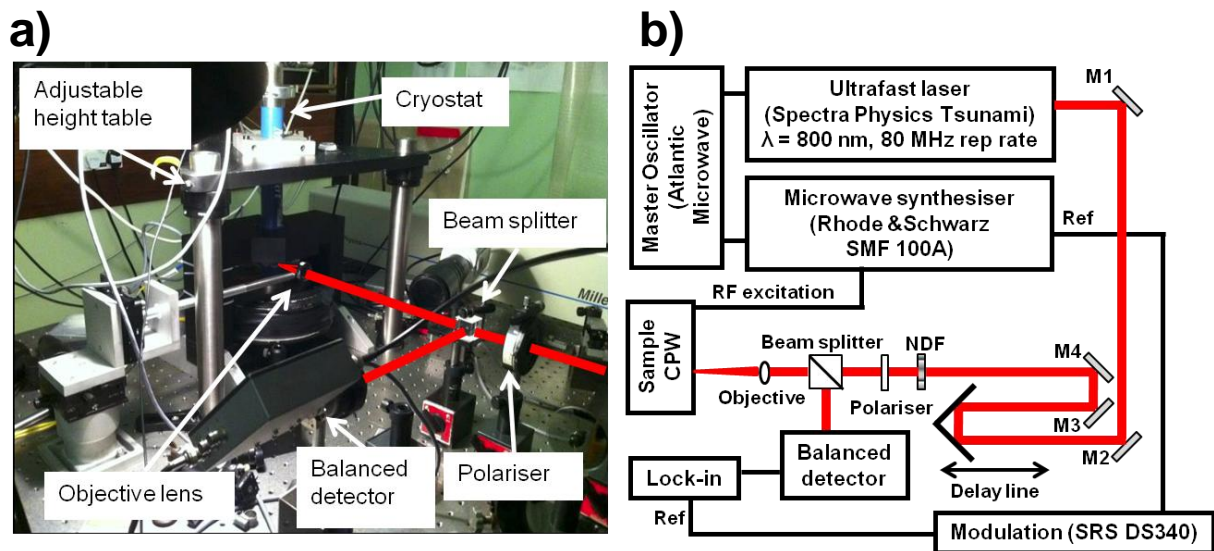


FIG. 3.4.3 (a) A photograph and (b) a schematic diagram of the pump-probe setup used to make low temperature TR-MOKE measurements. Magnetisation dynamics are excited by an RF magnetic field which is phase locked to an ultrafast pulsed laser system. The laser beam is incident on the sample surface at normal incidence so as to detect the polar Kerr effect. The pump-probe delay time is adjusted by delaying the probe beam with an optical delay line.

For the low temperature TR MOKE setup all timing signals were locked to a master oscillator (Atlantic Microwave) that produced a pair of phase locked outputs at 80 MHz and 10 MHz. Magnetisation dynamics were excited by passing the output of a microwave generator (Rhode & Schwarz: SMF-100A), locked to the 10 MHz master oscillator output, down the sample waveguide. The dynamics were then probed by a Ti: sapphire pulsed laser system (Spectra Physics Tsunami Laser System) of 800 nm wavelength, 100 fs FWHM pulse width and 80 MHz repetition rate. The Tsunami was phase locked to the 80 MHz output of the master oscillator. The use of an 80 MHz repetition rate then confines the microwave excitation frequency to be an integer multiple

of 80 MHz. The relative delay between the pump and probe was changed by sending the probe beam through an optical delay line that offered a total delay of 4 ns and sub picosecond step resolution. After traversing the delay line the laser beam passed through a neutral density filter and then through a polariser with transmission axis normal to the plane of the optical table, and therefore parallel to the symmetry axis of the sample waveguide. An 8 cm focal length lens was used to focus the beam onto the sample and to recollimate the reflected beam. The reflected beam was then diverted into a balanced detector by a intensity beam splitter. The balanced detector consists of a Glan-Thompson polarising beam splitter and a pair of photodiodes. The Glan-Thompson polarising beam splitter splits the incident beam into two beams with orthogonal linear polarisation. Each beam is detected by one of the photodiodes. Sum and difference amplifiers allow the Kerr rotation (difference) and DC reflectivity (sum) to be measured. The difference signal from the balanced detector is then passed to a lock-in amplifier. The amplitude of the microwave excitation was modulated at a specific audio frequency to facilitate lock-in detection.

To set and maintain a desired temperature in the range (4 K – room temperature) liquid He was circulated continuously through the cold finger of the cryostat, onto the end of which the OFHC sample holder was attached. The cooling setup used is shown in schematic form below in Fig. 3.4.4.

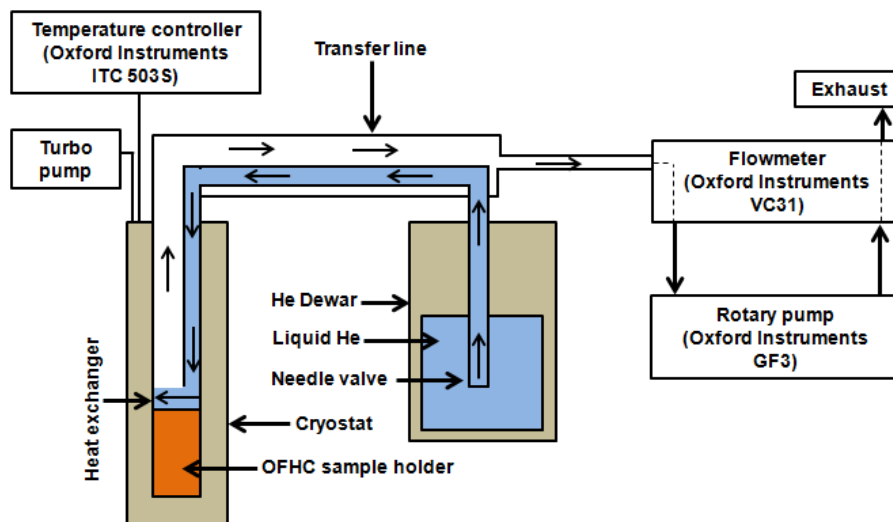


FIG. 3.4.4. Schematic of the cryostat cooling setup used to perform TR-MOKE measurements in the temperature range (4 K – room temperature). A He dewar is connected to the cryostat via a transfer line and the liquid He drawn through by pumping on the transfer line. The rate of the resulting flow can be controlled by a flow meter. A heater inside the cryostat cold finger helps set and regulate the temperature.

A heater in the cryostat is controlled by a temperature controller (Oxford Instruments ITC 503S) allowing the desired temperature to be set. As the heater works automatically and the flow of liquid He is controlled manually there are several competing factors which must be considered when trying to set a specific temperature. Once a flow of liquid He was established it was found that the most effective way of changing temperatures was to leave the flow meter untouched and to manually adjust the needle valve on the transfer line to adjust the flow of liquid He drawn from the dewar. It was possible to remain at a desired temperature in the range 4 – 293 K to well within an accuracy of 1 K. It was necessary to pump on the vacuum space continuously to avoid the build up of condensation on the inside of the optical window.

Results obtained with low temperature TR-MOKE setup are shown in chapter 5.

### **3.5 Experimental development of Time-Resolved XPEEM**

In addition to the FMR based experiments described above, this PhD also led to the development of Time-Resolved X-ray Photoemission Electron Microscopy (TR-XPEEM) on beamline I06 at the Diamond Light Source. TR-XPEEM<sup>45,46</sup> has potential to extend TRSKM and BLS studies of nanomagnets.

XPEEM utilises XMCD resulting in chemical and site specificity and magnetic contrast. As discussed in chapter 2, when a transition metal ferromagnet is irradiated with soft x-rays of the appropriate energy, an electron is excited from the 2p core states to the Fermi level. There are two decay channels via which the excited photoelectron can return to its ground state; emission of a photon (fluorescence) or emission of an electron by an Auger process. The latter causes a cascade of secondary electrons to be emitted from the sample surface and it is this yield that is detected in XPEEM measurements. As the escape length of electrons in such a material is only a few nanometres XPEEM is predominantly surface sensitive. Magnetic contrast is obtained by subtracting images taken with opposite circular polarisation. TR-XPEEM is a technically challenging measurement technique that is performed in an Ultra High Vacuum of the order  $10^{-10}$  mbar. A photograph of the XPEEM microscope is shown below in Fig. 3.5.1.

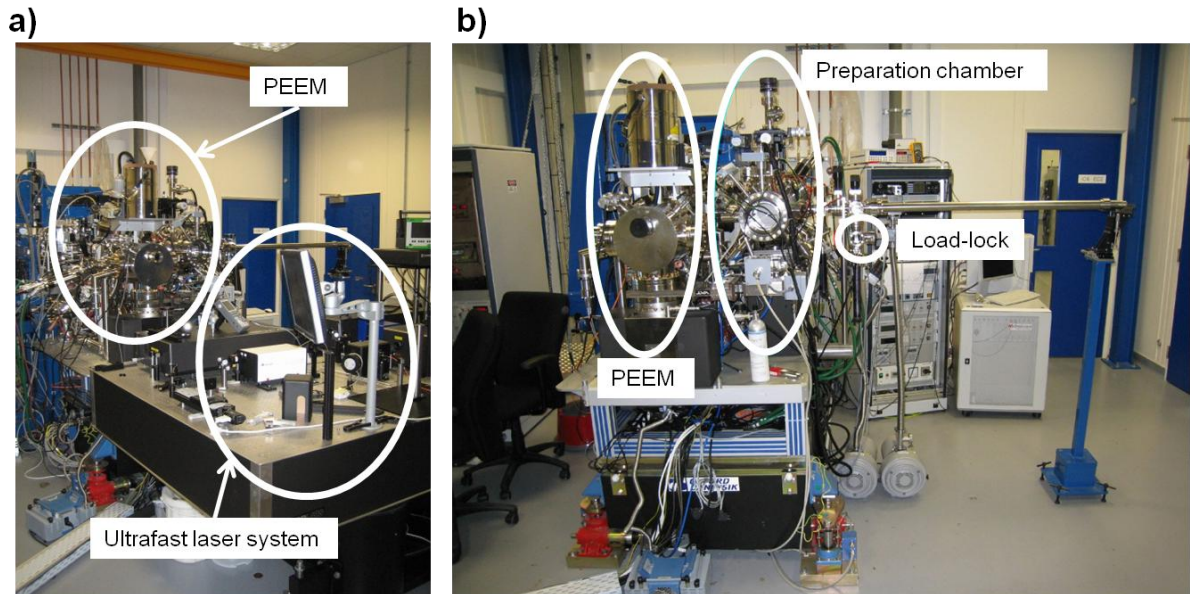


FIG. 3.5.1. (a) A photograph of the Elmitec XPEEM microscope on beamline I06 at Diamond. (b) Samples are placed in the load lock before being attached to the long manipulator under vacuum. They are then fed through the prep chamber before slotting into a holder in the PEEM ready for measurement.

Multilayer stacks of the form: Ta(5)/Cu(25)/[Ta(3)/Cu(25)]<sub>3</sub>/Ta(10)/Ru(5)/Ni<sub>81</sub>Fe<sub>19</sub>(40)/Al(1.5)+oxidation (thicknesses are in nanometres) were magnetron sputtered onto an insulating sapphire substrate of 500 μm thickness. Ni<sub>81</sub>Fe<sub>19</sub>/AlO<sub>x</sub> elements were formed on the Cu underlayer by a combination of electron beam lithography and ion beam milling. The remaining Cu was then patterned by photolithography and ion beam milling to form a CPW structure with a characteristic impedance of 50 Ω. The CPW was tapered to confine the transmitted current within the narrow middle section (Fig. 3.5.2. (a)). A NiCr thin film resistor, designed to have a resistance of 50Ω, was deposited at one end so as to absorb current pulses and prevent multiple reflections of the pulse propagating along the CPW. The permalloy elements lay on top of the central conductor of the middle section where they experienced an in-plane magnetic field. Au bond pads were deposited at each end of the waveguide to facilitate electrical contacting to the sample CPW. Two types of structure were fabricated, with central conductor widths of 6 μm and 30 μm. The permalloy sample elements were of square, rectangular, elliptical or circular shape with lateral dimensions ranging from 250 nm to 10 μm. To measure the electron yield the samples were placed inside a modified Elmitec sample cartridge machined in Exeter like those shown below in Fig. 3.5.2. (b & c).

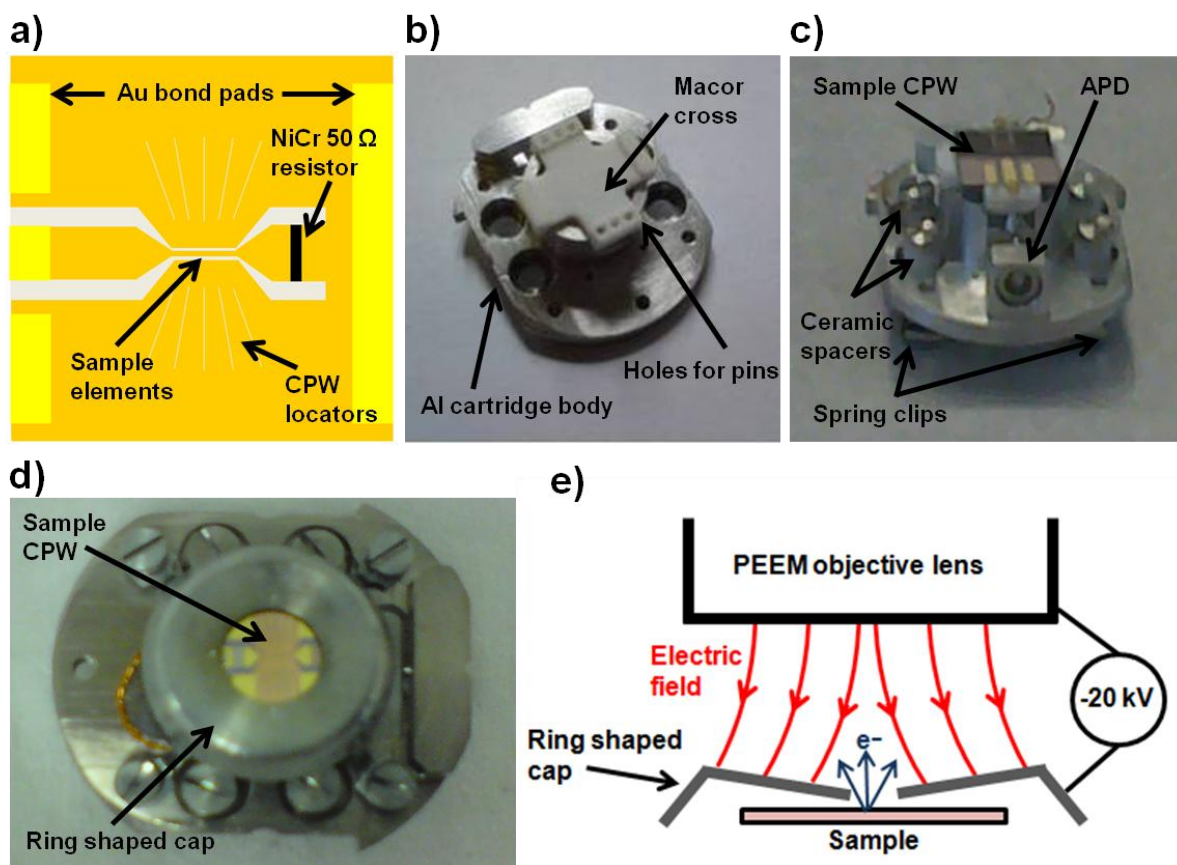


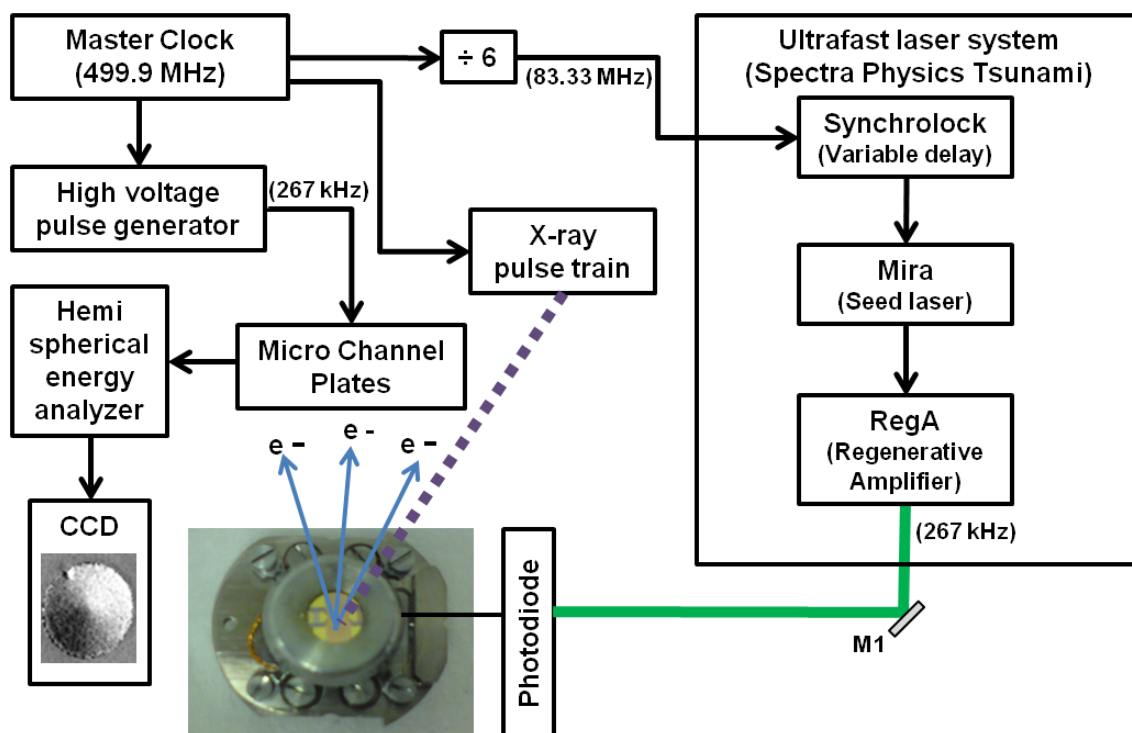
FIG. 3.5.2. (a) To allow dynamics to be excited the sample elements were deposited onto the central track of a CPW which is shown in schematic form. (b & c) Photographs of the cartridge body inspired by the original Elmitec design and later modified to accommodate a macor cross on which the sample sat. (d & e) To collect the emitted photoelectrons a ring shaped cap is centred on the sample CPW and a voltage applied between the cap and the base, and the PEEM objective lens.

To collect the emitted photoelectrons it is necessary to mount a conducting ring shaped cap over the sample (Fig. 3.5.2. (d)). A -20 kV bias is then applied between the cartridge/sample and the objective lens of the PEEM (Fig. 3.5.2. (e)). This results in an intense electric field pulling the electrons off the sample surface and into the PEEM detector. The precise spatial distribution of the electric field is determined by the shape of the ring shaped cap. The x-ray beam was incident at 16° grazing angle and so measurements were predominately sensitive to the in-plane component of the magnetisation. The sample CPW was mounted on a macor cross that was fixed to the Al cartridge body (Fig. 3.5.2. (b)). Au plated Cu pins passed through holes at the edges of the macor cross. An Avalanche Photodiode (APD) was electrically connected to the sample CPW by wire bonding the heads of the pins to Au bond pads on the CPW and then vacuum soldering one of the APD legs to the bottom of the pins. The second APD

leg was electrically connected to the spring clips on the bottom of the cartridge so that it could be reverse biased. The spring clips were made from  $W_{97}Re_3$  and were electrically isolated from the Al body by insulating ceramic inserts made from PEEK, allowing the APD to be biased with respect to the cartridge.

TR-XPEEM is a stroboscopic measurement and so there must be a fixed phase relationship between the pump and probe. To this end all timing signals were derived from the synchrotron master oscillator. The APD was gated by an ultrafast laser system (Coherent RegA) whose seed laser (Mira) was locked to the master oscillator using a Synchro-Lock system (Coherent). To do this it was necessary to divide the  $\sim 500$  MHz master oscillator by 6 (giving 83.33 MHz) so that it lay within the locking range of the seed laser. A schematic of the timing arrangement for TR-XPEEM is shown below in Fig. 3.5.3. (a).

**a)**



**b)**

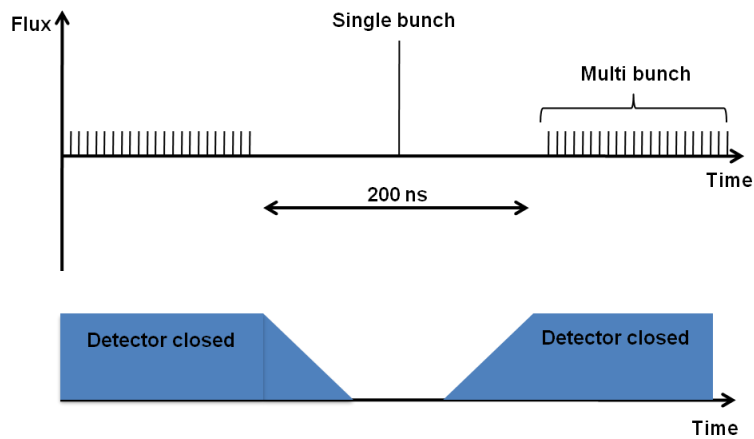


FIG. 3.5.3. (a) A schematic diagram of the timing arrangement used to make TR-XPEEM measurements on beamline I06. (b) A schematic of the hybrid bunch filling structure illustrating that measurements were made only with the larger flux single bunch.

There are 936 buckets, periodically separated in time by 2 ns, around the Diamond storage ring that can be filled with electron bunches – this is referred to as the filling structure. For the TR-XPEEM measurements detailed in this thesis the so-called hybrid bunch mode was used, shown above in schematic form in Fig. 3.5.3. (b). Here a higher flux pulse, referred to as the single bunch, used for imaging is placed in a 200 ns wide gap in the filling structure. The single bunch orbit has a period of 1.87  $\mu\text{s}$ , resulting in a repetition rate of 534 kHz. As the maximum repetition rate of the RegA is 300 kHz it was necessary to measure with alternate single bunches by setting the RegA repetition rate to 267 kHz.

An additional complication not present in the other stroboscopic experiments detailed in this chapter is the need to gate the detector. The detectors in the PEEM microscope are Micro Channel Plates (MCPs). To measure only with the larger flux single bunch the MCPs were gated by a timing signal derived from the master oscillator signal (Fig. 16. (b)). This allowed them to be turned on to record the signal from the single bunch and then turned off during the arrival of the multi-bunch. This was accomplished by using a high voltage pulse generator that was triggered by the bunch marker (a timing signal specific to the single bunch which is derived from the master oscillator), and therefore by the master oscillator. This enabled the voltage applied to the MCP to swing between 900 and 1200 V, which had a sufficient effect on the gain that the MCP could be

considered to be being turned on and off. Before passing through the MCP the electron yield passes through a series of optics and a hemispherical analyzer. After passing through the MCP it is then incident upon a fluorescent screen, where it is imaged by a CCD camera, from which the PEEM image is obtained. It is then necessary to locate the temporal overlap between the pump and probe, and check that the MCPs are being correctly gated. To this end, third harmonic generation from the laser was used to excite photoelectrons from the sample surface. The laser spot became visible in the PEEM image when the time of the arrival of the laser pulse fell within the gating window of the MCPs. The adjustment of the pump-probe delay was then carried out in two stages. Firstly the time of arrival of the laser pulse was set relative to the synchrotron bunch marker and could be adjusted in steps of 12 ns by choosing which pulse from the 83.33 MHz seed laser was injected into the RegA cavity using the Synchro-lock. Fine adjustment was then achieved by adjusting the phase locking of the seed laser relative to the bunch marker using the Synchro-lock. Zero delay was then identified by gating the photodiode with the laser and noting at which point the maximum shift of the photoelectron spectrum occurs. At this point the arrival of the pulsed magnetic field completely washes out the PEEM image. An example is given in the chapter detailing the experimental results from the TR-XPEEM setup (Chapter 7)

During the XPEEM measurements it was found to be vital to thoroughly clean all items before they were placed under vacuum and to pump on the vacuum until the pressure reached  $10^{-10}$  mbar. If this was not done then arcing was likely to occur when the extraction voltage was turned on. This is where a conducting path is formed between the sample surface and the extractor lens, resulting in the CPW and or the APD being destroyed.

The XPEEM results obtained during this PhD project are shown in chapter 7.

## Chapter 4: FMR characterisation of CoFe/NiFe

Phase-resolved X-ray Ferromagnetic Resonance (XFMR) measurements in fluorescence yield form the basis of the main experimental results presented in this thesis. As the technique was first developed during this PhD project the first half of this chapter is devoted to the first experimental results obtained that proved the feasibility of the experimental setup. The second half of this chapter details the Vector Network Analyzer Ferromagnetic Resonance (VNA-FMR) setup that was developed to enable high quality phase-resolved characterisation prior to synchrotron studies with a quick turn-around time.

### 4.1 Phase-resolved XFMR in fluorescence – measurements to prove the concept

#### 4.1.1. Motivation and geometry

Previous XFMR studies can be divided into two distinct categories: phase-resolved measurements<sup>37,38,39</sup> and time-average measurements<sup>40,41,42</sup>. Both types of measurements are generally performed in transmission, although an earlier phase-resolved study was performed in reflection at grazing incidence<sup>43</sup>. Transmission measurements are usually limited to samples grown on substrates such as Si<sub>3</sub>N<sub>4</sub> that are transparent in the soft x-ray regime. To extend phase-resolved XFMR measurements to samples on opaque substrates an experimental setup was developed to measure the fluorescence yield. The experimental results presented below have been published in Journal of Applied Physics<sup>25</sup>.

To demonstrate the feasibility of making phase-resolved XFMR measurements in fluorescence yield measurements were made on stacks of the form: Ta(5)[Cu(25)/Ta(3)]<sub>3</sub>/Cu(25)/Ta(10)/Ru(5)/Co<sub>50</sub>Fe<sub>50</sub>(0.7)/Ni<sub>90</sub>Fe<sub>10</sub>(5)/Ru(3) (thicknesses in nanometres). The stack was magnetron sputtered onto a 500 μm thick insulating sapphire substrate. Elements with lateral dimensions of 190 μm x 400 μm were formed on the thick Cu underlayer by electron-beam lithography and ion beam milling. The aspect ratio of the elements is sufficient to avoid any inhomogeneous

dynamics due to edge effects which may complicate the interpretation of the acquired data. Photolithography was then used to pattern the exposed Cu into a Coplanar Waveguide (CPW) structure with  $50 \Omega$  characteristic impedance and  $200 \mu\text{m}$  central track width. A  $5 \mu\text{m}$  border was left around the edges of the sample elements to avoid any sizable out-of-plane excitation<sup>47</sup>. All fabrication was carried out by collaborators at the Hitachi Global Storage Technologies (HGST) San Jose research centre. The sample stack was chosen to be representative of thin film sensor layers currently used in industry where for layers containing NiFe the Fe concentration is typically in the range 8 – 12%. It is for this reason that  $\text{Ni}_{90}\text{Fe}_{10}$  is used as opposed to the more commonly studied  $\text{Ni}_{80}\text{Fe}_{20}$ .

As described in the previous chapter; XFMR is a stroboscopic technique meaning that it is constrained to the measurement of repeatable processes and there must be a fixed phase relationship between the pump and probe. The pump was a Radio Frequency (RF) magnetic field resulting from the propagation of an RF current along the sample waveguide. The RF current was output from a custom comb generator system driven by the  $\sim 500 \text{ MHz}$  synchrotron Master Oscillator (MO). This then constrains the RF output frequency from the comb generator to be an integer multiple of  $500 \text{ MHz}$  if a fixed phase relationship is to be achieved. The sample waveguide was shorted at one end to ensure non-zero RF field amplitude at the sample position. The experimental geometry is shown below in Fig. 4.1.1.1.

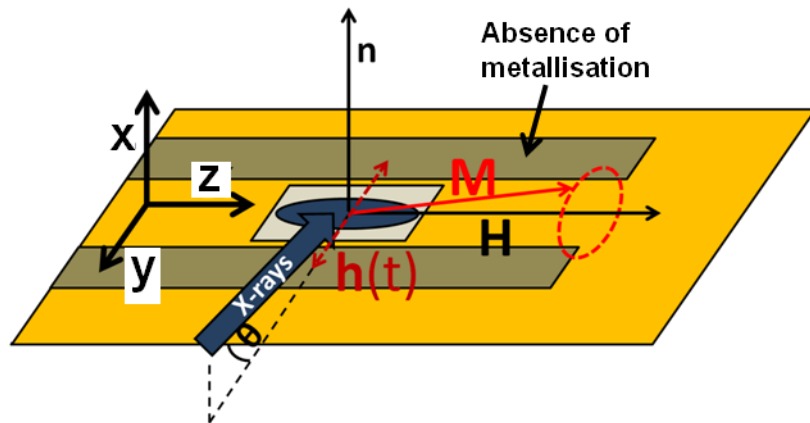


FIG. 4.1.1.1. A schematic representation of the experimental geometry used to make phase-resolved XFMR measurements. The magnetization ( $\mathbf{M}$ ) is forced into a state of steady precession about the externally applied static bias magnetic field ( $\mathbf{H}$ ) by an in-plane Continuous Wave (CW) RF magnetic field ( $\mathbf{h}(t)$ ). The probe beam is at a shallow grazing angle to detect the larger in-plane phase dependent component of magnetisation.

Careful consideration should be given to the choice of excitation frequency. If the frequency is too low then the Kittel curve (the resonance frequency as a function of applied bias field) of the sample under investigation will not pass through the chosen frequency point meaning that no dynamics can be excited. If the frequency is too high then the large resonant bias field will result in a reduced in-plane cone angle, and therefore a reduced dynamic signal for a given microwave power. For the measurements on  $\text{Co}_{50}\text{Fe}_{50(0.7)}/\text{Ni}_{90}\text{Fe}_{10(5)}$  a 4 GHz excitation was found to be suitable and so all XFMR measurements presented in this chapter were made with this excitation frequency.

Three different types of dynamic measurement can be made with the phase-resolved XFMR setup. Each involves the variation of one of the following parameters: externally applied bias field (field sweeps); the relative phase between the pump and probe (delay scans); and the x-ray energy (dynamic XMCD spectra). Each phase-resolved measurement will now be discussed in turn and typical results shown so as to illustrate the technique.

#### 4.1.2 Field sweeps

The first step in characterising the dynamic properties of a magnetic thin film is to find the resonance field for a given excitation frequency. In the XFMR experiment the magnetisation is driven by an RF magnetic field and so is forced to precess about the internal effective field at the frequency of the RF excitation. The phase of precession of the magnetisation vector relative to the driving field is altered by changing the value of the applied bias field. The parameter relating the magnetisation to the bias magnetic field in the presence of an RF magnetic excitation is the AC magnetic susceptibility<sup>48</sup> ( $\chi_{ij}$ ) which for an anisotropic material is a 2<sup>nd</sup> rank tensor represented by a 3x3 matrix. As the XMCD effect utilised to make XFMR measurements is a direct probe of the magnetisation this means that it is possible to measure the magnetic susceptibility tensor by sweeping the applied bias field. The measured component of  $\chi_{ij}$  is determined by the direction of the excitation field and the component of magnetisation that is being probed. With reference to the coordinate system shown in Fig. 4.1.1.1, this means that the magnetic susceptibility component  $\chi_{yy}$  is detected in the XFMR setup. In fact  $\chi_{xy}$  is also present in the measured signal but it is substantially weaker than the  $\chi_{yy}$  portion of the signal due to the shallow grazing angle. The bias field is applied along the symmetry

axis of the CPW and swept with the pump probe delay fixed. It should be noted that the magnetic susceptibility contains information on both the amplitude and phase of the magnetisation and so  $\chi_{yy}$  will be a complex number. This means that if  $\chi_{yy}$  is measured at an arbitrary point on the precession cycle of the magnetisation, or equivalently at an arbitrary relative delay between the pump and probe, then a mixture of the *Re* and *Im* components will be measured. To detect the purely *Re* and *Im* components of  $\chi_{yy}$  a pair of field sweeps are made at two pump-probe delays,  $\pi/2$  radians apart. Example field sweep measurements of the *Re* and *Im* components of  $\chi_{yy}$  measured for both Ni and Fe are shown below in Fig. 4.1.2.1.

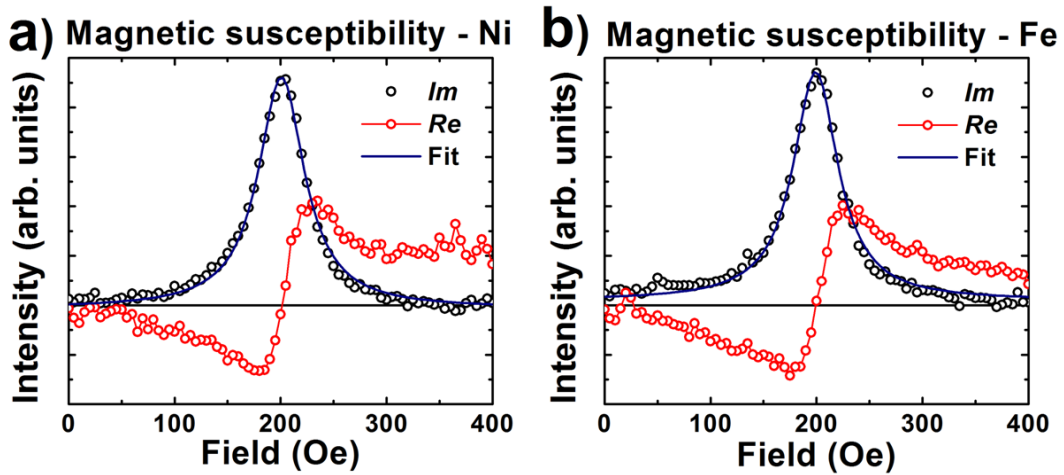


FIG. 4.1.2.1. (a) The *Re* and *Im* components of  $\chi_{yy}$  measured for Ni and (b) for Fe in a  $\text{Co}_{50}\text{Fe}_{50}(0.7)/\text{Ni}_{90}\text{Fe}_{10}(5)$  thin film sample by phase-resolved XFMR. Each curve is taken by sweeping the applied bias field (high to low) at fixed pump probe delay.

The excellent agreement between the lineshapes for the *Re* and *Im* components of  $\chi_{yy}$  measured for Ni (Fig. 4.1.2.1. (a)) and Fe (Fig. 4.1.2.1. (b)) show that the Ni and Fe moments are strongly exchange coupled together. The *Im* component (black curve) is related to the absorption of the energy supplied by the RF field which occurs in the ferromagnet. Resonance is defined as the condition for which the energy absorbed by an oscillator is a maximum (or equivalently the condition for which the amplitude of oscillation is greatest). This means that the resonance field is the applied bias field at which the *Im* component is a maximum, in this case 200 Oe. At the resonance field (the maximum of the *Im* component of  $\chi_{yy}$ ) the *Im* component of  $\chi_{yy}$  (black curve) corresponds to the case where the measured component of the dynamic magnetisation is  $\pi/2$  out of phase with the RF driving field. The *Re* component of  $\chi_{yy}$  (red curve) then

corresponds to the case where the measured component of the dynamic magnetisation and the RF driving field are in phase with one another (or equivalently  $\pi$  radians out of phase) at the resonance field.

There are several ways in which the correct phases for the *Re* and *Im* components can be identified. Firstly one could assume that at remanence the driving field and the magnetisation are  $\pi$  radians out of phase with one another for the case where there is no significant overlap of the FMR response with zero field. It is noted however that this may not be the best approach when dealing with heavily damped systems where the FMR response overlaps the remanent field (see Chapter 5 for an example). The second option is to run field sweeps at two arbitrary phases,  $\pi/2$  radians apart. The two field swept curves will generally have line shapes that are a mixture of the *Re* and *Im* components of  $\chi_{yy}$ . This mixing can be reversed by plotting the FMR curves in the complex plane and converted to 2D polar coordinates. By adding a constant offset to the polar angle one can then undo the mixing of the *Re* and *Im* components by performing a simple coordinate system rotation. As a safety check the user can then set the resonance field identified by the *Re* and *Im* components, run a delay scan (see section 4.1.3.) and then take a second set of field sweeps, this time at pump-probe delays corresponding to the node and anti node of the delay scan. If the two sets of field sweeps have the same line shape then the coordinate rotation has been successful, assuming only a small degree of mixing of the components of  $\chi_{ij}$ . In addition it should be noted that the lineshape of the magnetic susceptibility curves is strongly material dependent. Intrinsic Gilbert damping, magnon scattering, grain dispersion and the presence of impurities can all increase the overall damping of the excited dynamics resulting in an increased line width, reduced amplitude and a change in the resonance field.

With the resonance field well characterised for the chosen excitation frequency it is then possible to perform the 2<sup>nd</sup> type of dynamic measurement with XFMR – delay scans.

#### **4.1.3 Delay scans**

In a delay scan the time delay between pump and probe is scanned with the values of the applied bias field fixed and the energy of the x-ray beam kept constant. Each time the pump probe delay is changed so is the projection of the x-ray wave vector onto the phase dependent component of the magnetisation, and consequently the XMCD signal changes. The XMCD signal scales as the dot product of the two aforementioned vectors. It is therefore expected that a delay scan will result in a sinusoidal variation of the

XMCD signal that has a period constrained to be the same as that of the RF excitation. Typical examples are shown below in Fig. 4.1.3.1.

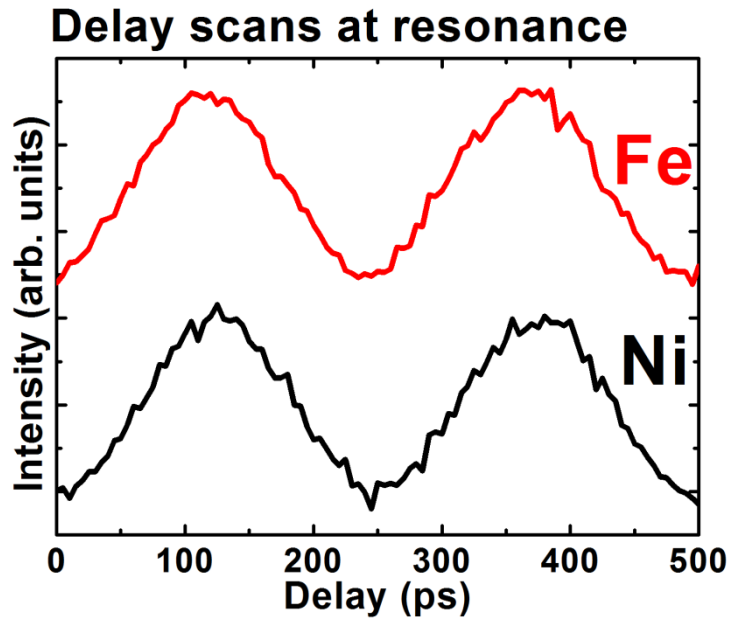


FIG. 4.1.3.1. Delay scans are taken by sweeping the pump probe delay with the value of the applied bias field fixed. Measurements taken at the resonance field of  $\text{Co}_{50}\text{Fe}_{50}(0.7)/\text{Ni}_{90}\text{Fe}_{10}(5)$  show that the Ni and Fe moments precess in phase with one another.

The amplitude of the delay scan signal will vary with the value of the applied bias field for fixed RF field amplitude, with the largest signal occurring when the bias field is set to its resonant value. If delay scans are taken at different values of the applied bias field then the phase of the delay scans relative to one another will vary as a function of applied bias field. If the range of applied bias field values extends sufficiently above and below the resonance field then by extracting the phase at each bias field value with sinusoidal fitting the phase relative to the driving field can be plotted as a function of the applied bias field. This process was performed successfully for the Spin Transfer Torque (STT) studies in chapter 6. The same information can be obtained by plotting the *Re* and *Im* components of  $\chi_{yy}$  in polar coordinates. For a heavily damped sample (chapter 6) it can be easier to obtain the polar angle by taking delay scans at a range of applied bias field values than by first measuring a set of field sweeps.

#### 4.1.4 Dynamic XMCD spectra

The third dynamic measurement that can be made is referred to as a dynamic XMCD spectrum. With the applied bias field set to the resonant value and the pump probe delay

fixed at a particular value of interest, the x-ray energy may then be swept just as it would be for a static X-ray Absorption Spectrum (XAS). In the static case it is necessary to take a pair of XAS spectra with either the sample magnetisation or the x-ray wave vector being reversed between the two scans before calculating the difference signal to yield an XMCD spectrum<sup>49</sup>. This is not necessary when measuring a dynamic XMCD spectrum. In XFMR the dynamic signal is recovered using audio frequency lock-in detection. If for example square wave amplitude modulation of the RF excitation is used, the excitation is being turned on and off periodically at a specific audio frequency. This means that the lock-in amplifier measures the difference in the x-ray absorption between the magnetisation lying along the equilibrium direction and the chosen point on the precessional cycle to which the pump probe delay corresponds. Examples of dynamic XMCD spectra for Ni taken at resonance at different points on the precessional cycle are shown below in Fig. 4.1.4.1.

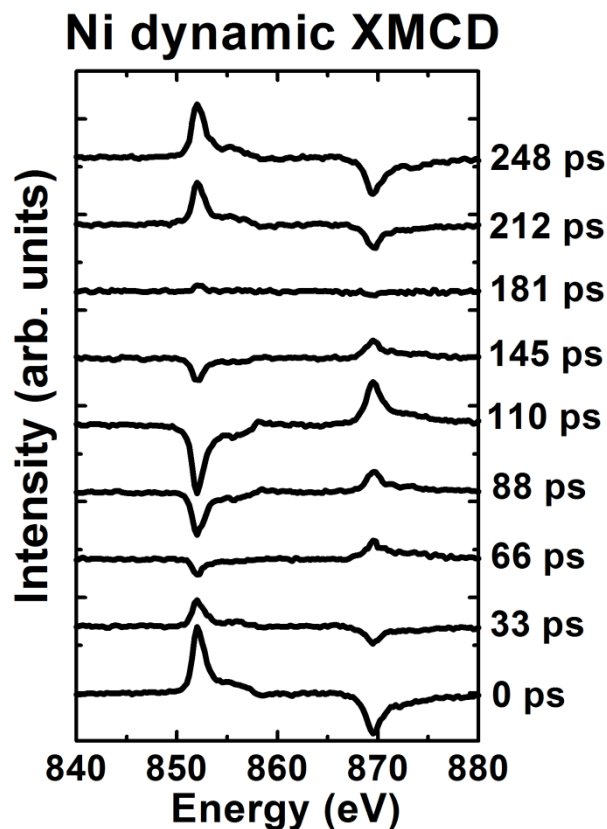


FIG. 4.1.4.1. Dynamic Ni XMCD spectra acquired with fixed circular x-ray polarisation through one 4 GHz precessional cycle. The XMCD signal scales as the scalar product of the x-ray wave vector (fixed) and the local magnetisation (precessing).

The XMCD signal should scale as the scalar product of the x-ray vector (which is fixed) and the local magnetisation (which is precessing). The data in Fig. 4.1.4.1. were taken with a 4 GHz RF excitation, the period of which is 250 ps. By comparing the spectra taken at time delays of 0 ps and 110 ps (approximately a  $\pi$  phase shift) it is seen that the signals are of approximately the same magnitude but opposite in sign. The spectrum taken at 66 ps is seen to have an amplitude close to zero.

The dynamic Ni XMCD spectra were overlaid on a conventional Ni XMCD spectrum, measured in fluorescence yield by flipping the sample magnetisation along the x-ray beam axis, to confirm that the two had the same lineshape. An example is shown in Fig. 4.1.4.2.

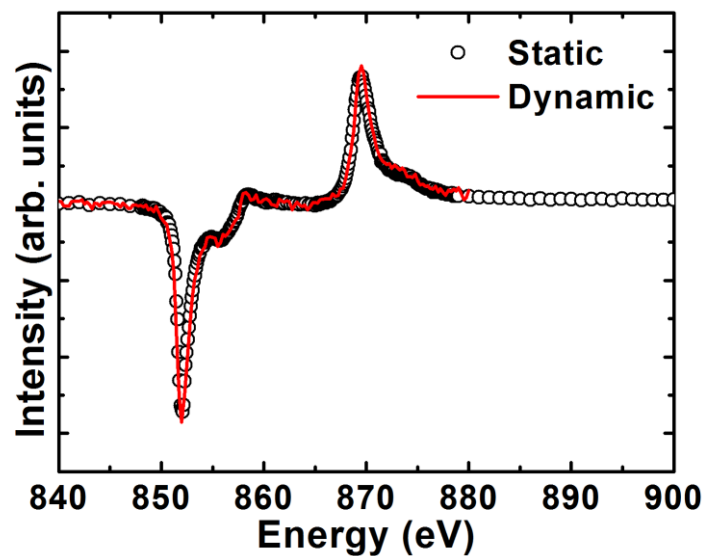


FIG. 4.1.4.2. The lineshape of a dynamic XMCD spectrum overlaid on a conventional static XMCD spectrum obtained in fluorescence yield.

The increased noise on the dynamic spectrum is to be expected as the measured fluorescence signal is approximately 5% of the static XMCD signal.

To extend the above study of the dynamic behaviour of  $\text{Co}_{50}\text{Fe}_{50}(0.7)/\text{Ni}_{90}\text{Fe}_{10}(5)$  an attempt was made to apply the XMCD sum rules to the dynamic spectra shown in Fig. 4.1.4.1. There are however some important caveats regarding the XMCD sum rules which are discussed briefly in the next section.

#### 4.1.5 An aside on the XMCD sum rules

The XMCD sum rules relate integrals of the XMCD spectrum to values for the spin and orbital components of the magnetisation. The simplest approach is to first try and find a value for the ratio of the spin and orbital components as this removes the requirement to know the number holes in the 3d band.

Equations for the sum rules were taken from the experimental work of Chen *et al.*<sup>50</sup> (chapter 2) and applied to the numerical integral of each of the dynamic spectra in Fig. 4.1.4.1. The aim was to look for any evidence of non colinearity of the spin and orbital moments through a change in their ratio around the precessional orbit. However, the calculated ratio of the spin and orbital moments was found to be negative. A negative sign was also found for static Ni XMCD in fluorescence yield. A negative value of the ratio of the spin and orbital moments would mean anti-parallel alignment of the moments projected along the x-ray wave vector, which has no existing theoretical or experimental basis. It was also the case that some of the integrals had not fully converged, in which case the value of the integral at the highest beam energy in the scan was used. The extracted values are shown below in Fig. 4. 1. 5. 1.

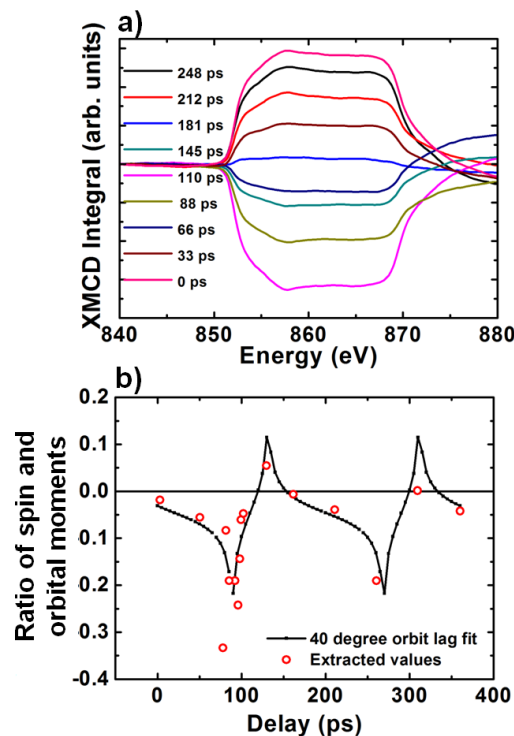


FIG. 4.1.5.1 (a) Integrals with respect to beam energy of the dynamic XMCD spectra shown in Fig. 4.1.4.1. are shown. (b) The sum rules were applied to A negative value for the ratio of the spin and orbital

moments is obtained for nearly all delay values. A reasonable fit to the data is obtained by assuming a 40° angle between the spin and orbital moments.

The reason for the negative value of the ratio of the spin and orbital moments is that the XMCD sum rules are derived under the assumption that the yield is proportional to the incident x-ray intensity<sup>51</sup>. This is not strictly the case in fluorescence yield due to self absorption effects. As the fluorescent photons are passing through the sample stack some of them are reabsorbed and so there is a dependence of the proportionality between the yield and the incident intensity on the x-ray energy. For this reason phase-resolved XFMR in fluorescence yield should be viewed as a high quality phase-resolved magnetometer that can be used to make measurements on opaque substrates but not as a means of applying the XMCD sum rules. Due to the limitations of the experimental data and the method of extracting the ratio of the spin and orbital moments, additional data with better statistics are required before firm conclusions can be drawn.

The algebra used to generate the fitted curve is given in Appendix 1 for completeness.

#### **4.1.6 Conclusions - XFMR**

In conclusion this section has shown that phase-resolved XFMR in fluorescence yield can be used to make high quality measurements of the magnetisation dynamics of magnetic thin films by probing the phase dependent components of the magnetisation orthogonal to the applied field. The *Re* and *Im* components of the complex magnetic susceptibility component  $\chi_{yy}$  can be measured and delay scans allow the relative phase of precession of different chemical species to be measured with a resolution of 1 – 2 ps. It is also possible to obtain an XMCD spectrum from the phase dependent component of the magnetisation at a chosen point on the precessional cycle. The lineshape was shown to be identical to that obtained with the conventional static XMCD measurement technique.

The advantage of phase-resolved XFMR over more commonly used techniques such as Time Resolved Scanning Kerr Microscopy (TRSKM) or Brillouin Light Scattering (BLS) is that XFMR utilises the chemical specificity of the XMCD effect. The use of fluorescence yield extends XFMR measurements to samples that are opaque in the soft x-ray regime, removing the requirement to grow samples on fragile Si<sub>3</sub>N<sub>4</sub> membranes.

## **4.2 How to make frequency swept phase-resolved VNA-FMR measurements**

### **4.2.1 Motivation**

Phase-resolved VNA-FMR was developed as part of this PhD project to provide a quick means of characterising the resonance field of ferromagnetic thin films prior to making more detailed synchrotron based measurements with XFMR. This section illustrates the types of measurement that can be made by showing typical examples of data obtained from a  $\text{Co}_{50}\text{Fe}_{50}(0.7)/\text{Ni}_{90}\text{Fe}_{10}(5)$  thin film. The various procedures employed to reduce the level of background noise are also discussed.

As synchrotron beamtime has a tight set of time constraints it is essential to perform some initial dynamic characterisation before embarking on XFMR measurements. Such characterisation can be done with the TRSKM setup that was well established in Exeter prior to the start of this PhD project - data is shown in chapter 5. Although high quality FMR characterisation can be performed with TRSKM there is a far less time consuming way in which this can be done, namely Vector Network Analyzer Ferromagnetic Resonance (VNA-FMR). VNA-FMR measurements are made as a function of the frequency of a CW RF excitation with the value of the applied bias field fixed<sup>44</sup>. The VNA outputs an RF signal to the sample CPW and can then measure both the transmitted and reflected power by comparing the returning signal(s) with the original output signal. A VNA can be thought of as a single unit comprising of an RF generator and a high frequency lock-in amplifier. Full details of the experimental setup can be found in chapter 3.

### **4.2.2 Non phase-resolved VNA-FMR**

The width of the CPW centre line used for XFMR is limited to 200  $\mu\text{m}$  by the size of the x-ray spot. As no such limitation exists for VNA-FMR it was possible to use a CPW with a 50  $\mu\text{m}$  central track width that had a single 40  $\mu\text{m}$  x 400  $\mu\text{m}$  sample on the central track. As with the XFMR measurements described above a 5  $\mu\text{m}$  gap was left from the edges of the central track to avoid out-of-plane excitations. The aspect ratio is sufficient to avoid complications due to edge effects. The devices measured for VNA-FMR and XFMR were defined in the same wafer stack. The waveguide structures measured were shorted at one end as in the XFMR, meaning that only the reflected

power could be measured. The magnitude of the reflected signal is denoted  $S_{ij}$  where for the case of a reflection geometry ( $i = j$ ) and  $S$  is an element of the scattering matrix, often referred to as an  $S$ -parameter<sup>52</sup>. If the sample magnetisation is saturated along the symmetry axis of the CPW and the frequency of the RF excitation swept then the magnitude of the reflected power was found to be dominated by noise as shown in Fig. 4.2.2.1 (a) below.

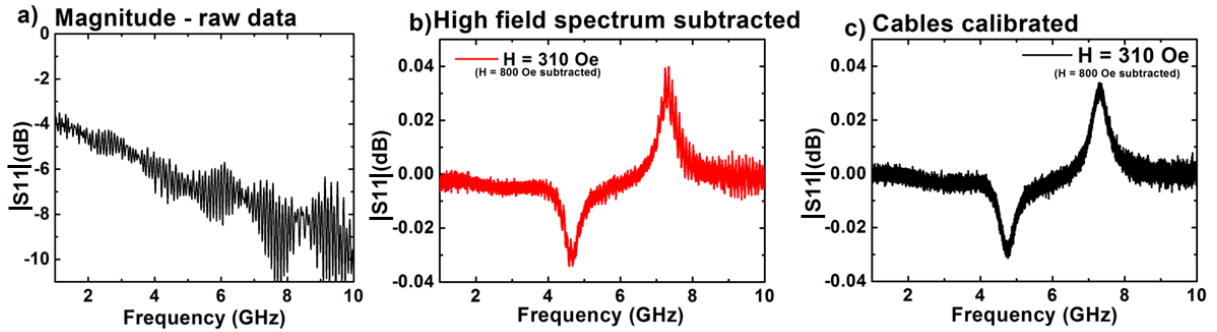


FIG. 4.2.2.1. (a) A VNA-FMR measurement at an applied bias field of 310 Oe showing the magnitude of the reflected power as a function of excitation frequency before any background subtractions. (b) By subtracting a spectrum taken at a higher bias field value (in this case 800 Oe) it is possible to remove a lot of the spurious non magnetic signal. (c) The noise can be further reduced by calibrating out artefacts due to the RF cabling using a set of mechanical standards.

It is clear from Fig. 4.2.2.1. (a) that there is no Lorentzian FMR curve visible and so it was necessary to perform several background subtractions. If a pair of VNA-FMR spectra are measured at different bias fields directed along the CPW symmetry axis and then subtracted from one another a Lorentzian peak can clearly be seen as shown in Fig. 4.2.2.1. (b). Alternatively a background spectrum taken with the bias field transverse to the sample waveguide so that the RF field exerts no torque on the magnetisation can be subtracted. There are two peaks of opposite sign as the background spectrum taken at higher applied bias field also contains a magnetic signal. To reduce the residual noise it was then necessary to calibrate out the artefacts due to frequency dependent losses in the RF cabling. When measuring the magnitude of the FMR response such a calibration can be done by using a set of mechanical standards that consist of a well characterised  $50 \Omega$  load, short circuit and an open circuit. Each mechanical standard is screwed onto the end of the RF cables going to the sample waveguide and measured at the same RF power and across the same frequency range as the FMR measurements are to be made. The VNA then compares the results from these simple structures with idealised data to

produce a correction factor that accounts for losses in the cabling. The result of applying the said correction factor is shown in Fig. 4.2.2.1. (b). More details on the calibration process are given in the experimental development chapter. The peak height in Fig. 4.2.2.1. (c) of approximately 0.02 dB corresponds to an amount of energy absorbed by the film of the order 10  $\mu$ W for an RF power level of 50 mW (+17 dBm) at source. All measurements in this chapter were taken with a 50 mW (+17 dBm) power level at source, which for a 50  $\mu$ m CPW and after factoring in losses, gives an RF excitation field of several Oe. No evidence was found to indicate the presence of non linear effects.

As mentioned earlier in the experimental development chapter the wide straight section of the CPW, shown in the inset to Fig. 4.2.2.2. (a), had to be removed to make VNA-FMR measurements. The picoprobes used to take the RF from the cabling assembly down to the sample CPW had a pitch of 125  $\mu$ m and so were landed on the tapering region of the CPW. The adverse affect of the additional capacitance and inductance from the wide straight section on the measured signal can be clearly demonstrated by making measurements at different applied bias fields with the background subtractions detailed in Fig. 4.2.2.1. (c) applied.

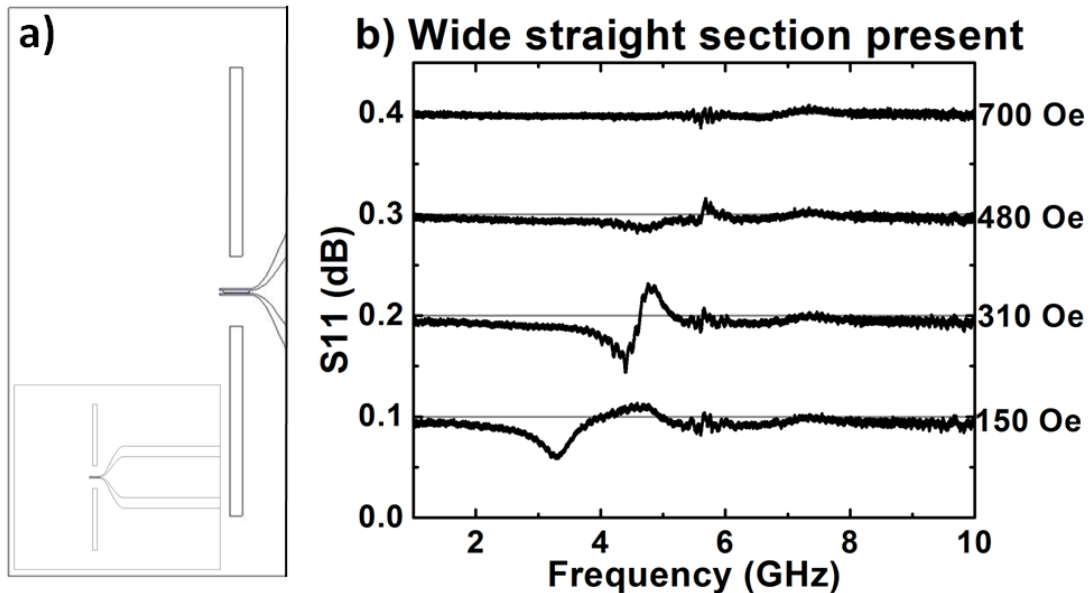


Fig. 4.2.2.2. (a) Scale drawing showing the section of the sample CPW that was removed to make VNA-FMR measurements. (inset) the unmodified sample CPW where the wide straight section of the CPW is present. (b) An attempt at measuring the magnitude of the FMR response. If the wide straight section of the sample waveguide is not removed then there is a field dependent distortion of the lineshape of similar magnitude to the FMR signal. The curves have been offset for clarity.

It is clear that for some applied bias field values in Fig. 4.2.2.2. (b) there is no measurable signal whilst at other field values, such as 310 Oe, there is a feature with lineshape that is heavily distorted and in no way comparable to the lineshapes acquired with the wide straight section of the sample CPW removed as shown in Fig. 4.2.2.2. (c). For this reason the wide straight section has been removed for all measurements shown in this chapter.

### 4.2.3 Phase-resolved VNA-FMR

For our sample geometry, VNA-FMR measures the  $Re$  and  $Im$  components of  $\chi_{yy}$  as in the XFMR measurements shown in Fig. 4.1.2.1. It is important to note that to record phase information the calibration performed to remove the cabling artefacts must also accurately account for the length of the RF path external to the VNA. The complications encountered by ignoring this caveat can be illustrated by calibrating with mechanical standards screwed onto the ends of the RF cabling and attempting to measure the  $Re$  and  $Im$  components.

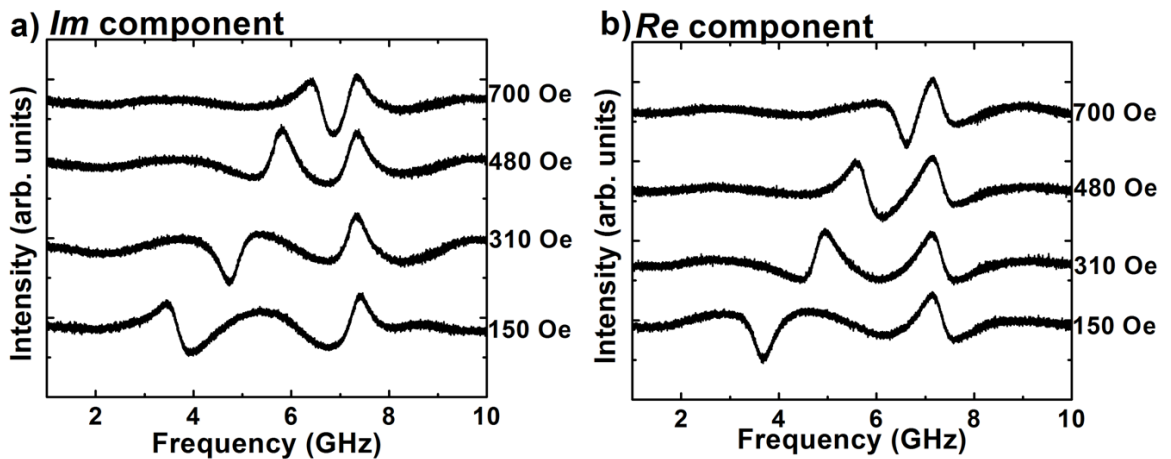


FIG. 4.2.3.1. To measure the purely  $Re$  and  $Im$  components of  $\chi_{yy}$  the length of the RF path outside of the VNA must be accurately accounted for. Here mechanical standards have been used to account for the cable, but not picoprobe, path lengths. A mixing of the two components is seen for two orthogonal RF phases (a & b). A spectrum taken with an 800 Oe bias field has been subtracted from each curve.

The RF phase is shifted by  $\pi/2$  between Fig. 4.2.3.1. (a) & (b) so as to measure the  $Re$  and  $Im$  components of  $\chi_{yy}$ . Instead a bias field dependent mixing of the two components is seen as the path length of the picoprobes has not been accounted for in the calibration. Whilst the mechanical standards account for the path length of the RF cabling they do not account for the additional path length of the picoprobes. To include the effect of the picoprobes in a calibration it is necessary to use a so-called calibration substrate. This

consists of the same simple circuits (open, short and  $50 \Omega$  load) as the mechanical standards, deposited as thin film structures on an insulating substrate. The choice of calibration substrate is specific to the size and footprint of the picoprobes – for further details see the experimental development chapter. The user lands the picoprobes on each of the 3 standards in turn whilst monitoring the DC resistance to determine when the picoprobes have been properly landed on a given device. When this calibration procedure has been completed it is then possible to measure the  $Re$  and  $Im$  components of  $\chi_{yy}$  without any field dependent mixing of the two components, as shown in Fig. 4.2.3.2.

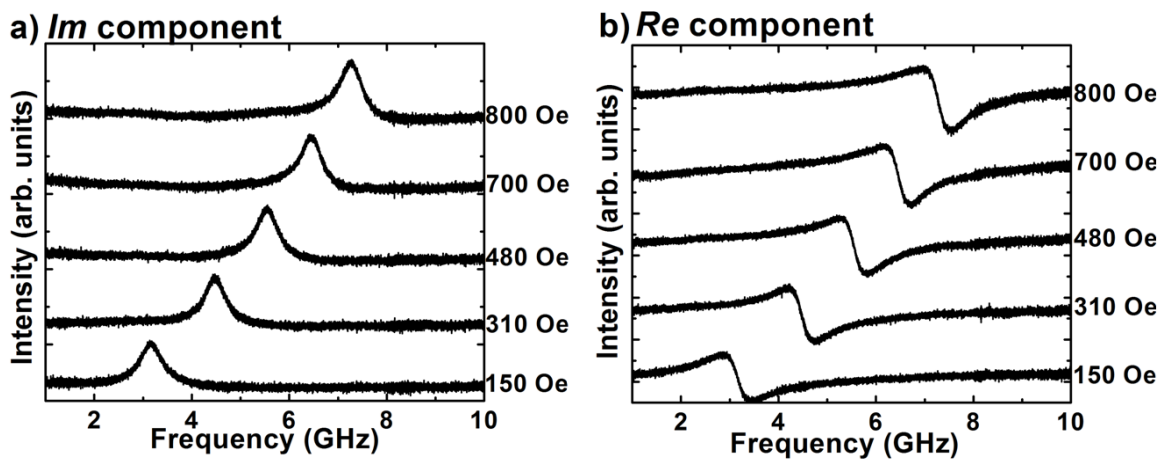


FIG. 4.2.3.2. The  $Re$  and  $Im$  components of  $\chi_{yy}$  can be measured when the affect of the path length of the picoprobes is calibrated out with a calibration substrate. A non magnetic spectrum taken with the bias field applied along the direction of the excitation field has been subtracted.

The  $Re$  and  $Im$  components can be clearly seen as a function of applied bias field once the additional path length of the picoprobes has been calibrated out. In addition a non magnetic spectrum in which the bias field is applied along the direction of the RF excitation field (no torque) has been subtracted.

#### 4.2.4 Conclusions – VNA-FMR

This section details high quality phase-resolved measurements on ferromagnetic thin films using VNA-FMR. The VNA-FMR setup was developed to allow fast characterisation of the resonance field of samples of interest prior to synchrotron based XFMR studies. The VNA-FMR technique allows FMR spectra that would take of the order an hour to acquire with TRSKM to be acquired in just a few seconds

## Chapter 5: Enhanced damping in spin valve free layers due to the addition of Dy capping layers

This chapter presents a detailed characterisation of a  $\text{Co}_{50}\text{Fe}_{50}(0.7)/\text{Ni}_{90}\text{Fe}_{10}(5)/\text{Dy}(1)/\text{Ru}(3)$  thin film, to explore the behaviour and possible micromagnetic origins of the enhanced damping observed by Maat<sup>53</sup> *et al.* Time-Resolved Scanning Kerr Microscopy (TRSKM), low temperature Time-Resolved MOKE and phase-resolved X-ray Ferromagnetic Resonance (XFMR) are used for dynamic characterisation as a function of position, temperature and chemical specificity respectively. Static XMCD measurements are made as a function of temperature to determine changes in the magnetic ordering. The linewidth and resonance field are seen to depend strongly on temperature, and possible explanations are discussed.

### 5.1 Motivation

Magnetisation dynamics govern the operation of a range of widely used high frequency magnetic devices such as magnetic hard disc drives and spin transfer torque oscillators. For the fast moving development in these fields to continue it is becoming increasingly important to improve our understanding of the magnetisation dynamics that underpin the operation of such devices.

It has recently been reported by Maat<sup>53</sup> *et al.* that spin torque noise in current perpendicular to the plane spin-valves can be greatly reduced by capping with a rare earth material such as Dy. The advantage of capping with a rare earth material, as opposed to doping<sup>54,55</sup> is that doping with a material that is non magnetic at room temperature will dilute the magnetisation of the spin-valve free layer and may reduce the giant magneto resistance.

### 5.2 Experimental setup details

A  $\text{Ta}(5)[\text{Cu}(25)/\text{Ta}(3)]_3/\text{Cu}(25)/\text{Ta}(10)/\text{Ru}(5)/\text{Co}_{50}\text{Fe}_{50}(0.7)/\text{Ni}_{90}\text{Fe}_{10}(5)/\text{Dy}(1)/\text{Ru}(3)$  stack was magnetron sputtered onto an insulating sapphire substrate of 500  $\mu\text{m}$  thickness. A second stack with the Dy(1) layer absent was also deposited and served as a control sample. The magnetic parts of the stacks are representative of free layers being used in high density recording heads. Magnetic elements with lateral dimensions of several hundred microns were defined on top of the thick Cu/Ta underlayer by a

combination of electron beam lithography and ion beam milling. Photolithography was then used to pattern the exposed Cu into a Coplanar Waveguide (CPW) structure of  $50 \Omega$  characteristic impedance. TRSKM measurements were made on samples on CPWs with  $50 \mu\text{m}$  wide central tracks and  $40 \mu\text{m} \times 400 \mu\text{m}$  sample elements. Owing to the larger spot size XFMR measurements were made on devices with  $200 \mu\text{m}$  central tracks and  $190 \mu\text{m} \times 400 \mu\text{m}$  sample elements. The aspect ratio of the samples was sufficient to avoid any spatially inhomogeneous dynamics due to edge effects. A  $5 \mu\text{m}$  border was left between the edges of the sample element and the central track to avoid any sizable out-of-plane excitation. The reader is referred to chapter 3 for a scale drawing of the devices.

The measurements presented in this chapter were performed with several different experimental techniques that utilise the experimental geometry shown in Figure 5.2.1. below.

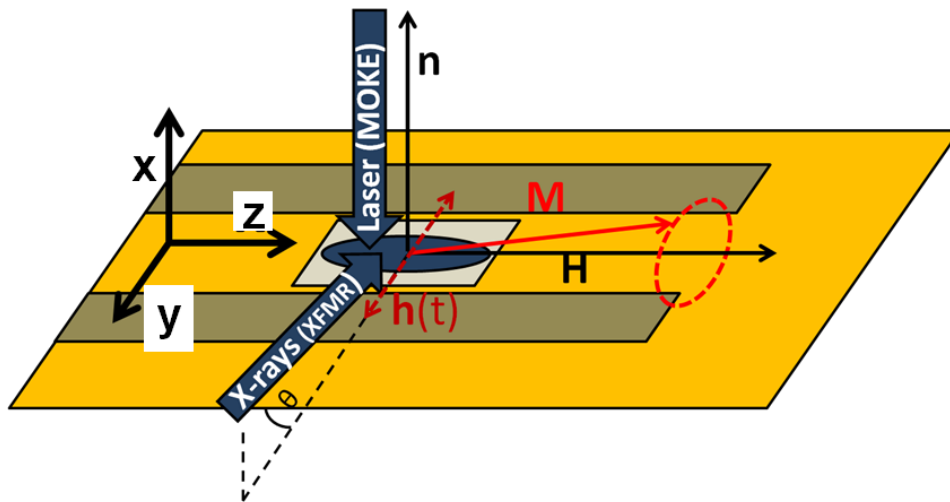


FIG. 5.2.1. A schematic diagram of the experimental geometry used to make TRSKM and phase-resolved XFMR measurements. The magnetization ( $\mathbf{M}$ ) is forced into a state of steady precession about the externally applied static magnetic field ( $\mathbf{H}$ ) by an in-plane continuous wave microwave magnetic field ( $\mathbf{h}(t)$ ). For TRSKM measurements the probe beam is at normal incidence and the polar Kerr effect is used to detect the out-of-plane component of the magnetization. For XFMR the probe beam is at a shallow grazing angle to detect the larger in-plane oscillatory component of magnetisation.

Dynamic characterisation at room temperature was carried out using a Time-Resolved Scanning Kerr Microscope (TRSKM) with sub micron spatial and picosecond temporal resolution<sup>56</sup>. In the TRSKM a Ti: sapphire ultrafast laser produces probe pulses with a

FWHM of the order 100 fs at a repetition rate of 80 MHz. Dynamics were excited by a pulse generator that was phase locked to the master oscillator of the laser. Alternatively a phase locked Continuous Wave (CW) microwave source can be used. The probe pulses are focused onto the sample surface with a microscope objective which also recollimates the reflected pulses. The use of a polarising balanced photodiode detector, delay generator and audio frequency lock-in detection then allows the resulting Kerr rotation to be measured at various time delays between the pump and probe in a stroboscopic fashion. For all results presented in this chapter the polar Kerr effect is shown.

To measure dynamics as a function of temperature the sample waveguide was mounted inside a He gas flow cryostat (Oxford Instruments Microstat He). Optical access was possible through an optical window made of low Verdet constant glass. Ag paint was used to electrically connect the sample waveguide to an interconnecting PCB waveguide, onto which a length of vacuum SMA was connected. An RF feedthrough was fitted to the cryostat to allow the RF to be passed to the sample waveguide. The temperature was measured at the end of the cryostat cold finger which terminates in a copper block, onto which a copper sample holder was attached. The sapphire sample substrate was then placed in thermal contact with the copper sample holder. With both copper and sapphire being excellent thermal conductors it was assumed that the temperature measured at the end of the cold finger is the same as the sample temperature, although there may be a small systematic offset for all measured temperatures. Further details of the setup can be found in chapter 3.

Temperature dependent static characterisation was performed with X-ray Magnetic Circular Dichroism (XMCD) in fluorescence yield in the Vector Magnet Magnetometer (VMM)<sup>57</sup> on BL 4. 0. 2 at the Advanced Light Source. The chemical specificity of XMCD enables the magnetic signal from the Dy capping layer to be isolated. In addition phase-resolved XFMR measurements in fluorescence yield were made at room temperature to complement the MOKE studies.

### **5.3 Experimental results**

The large effect of the Dy cap on the relaxation time of magnetisation dynamics in  $\text{Co}_{50}\text{Fe}_{50}(0.7)/\text{Ni}_{90}\text{Fe}_{10}(5)/\text{Dy}(1)/\text{Ru}(3)$  is clearly illustrated by the results of pulsed field excitations shown in Fig. 5.3.1.

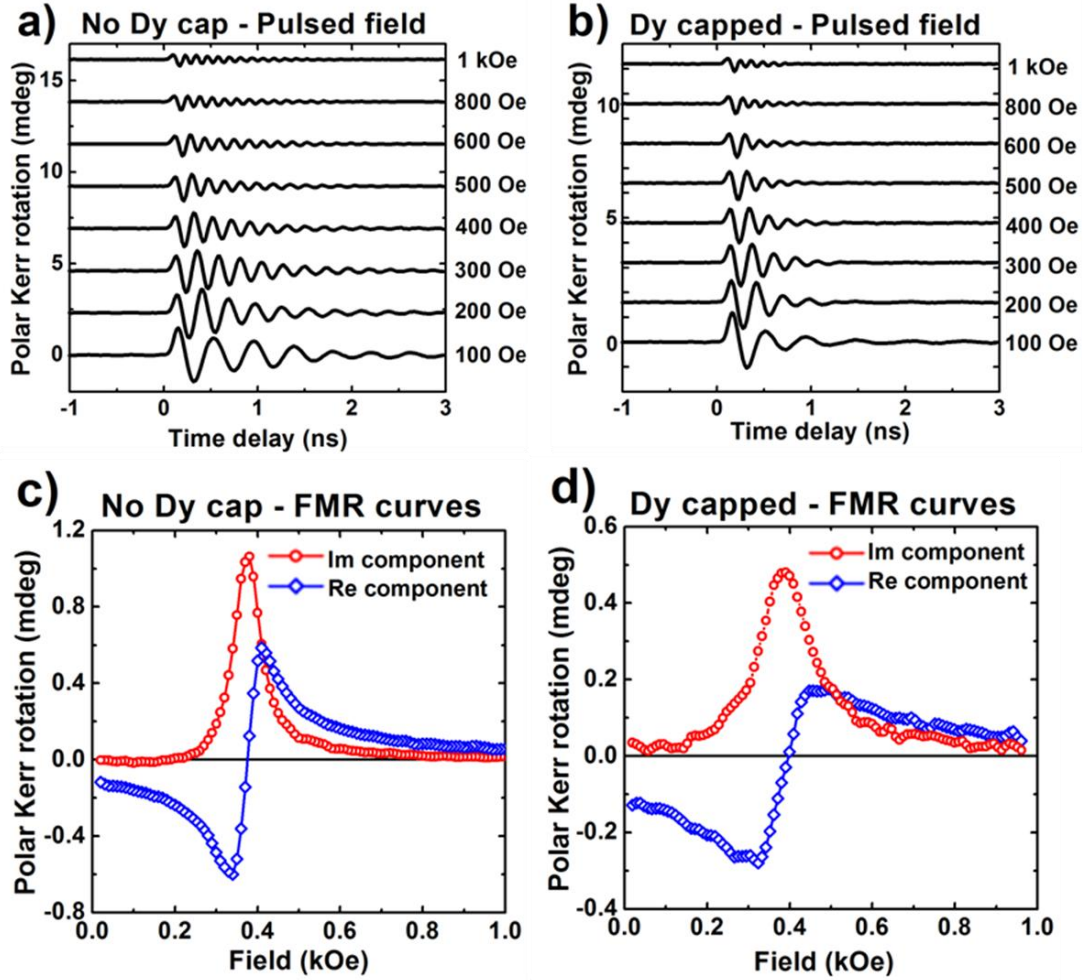
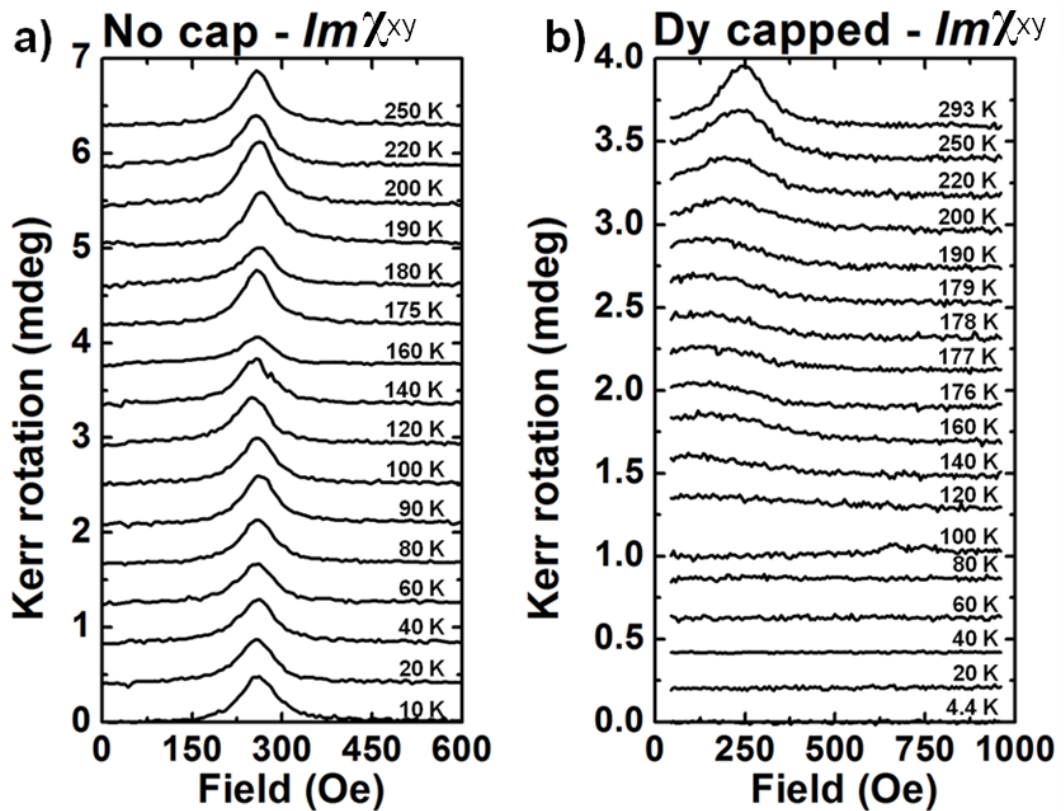


FIG. 5.3.1. (a) Room temperature pulsed field polar Kerr measurements on  $\text{Co}_{50}\text{Fe}_{50}(0.7)/\text{Ni}_{90}\text{Fe}_{10}(5)/\text{Ru}(3)$  are noticeably more lightly damped than equivalent measurements (b) taken with the addition of a Dy capping layer. Field sweeps acquired in the presence of a 5 GHz CW excitation (c) and (d) yield the *Re* and *Im* components of the AC magnetic susceptibility component  $\chi_{zy}$  with the presence of Dy (d) noticeably broadening the line width and therefore enhancing the damping.

Excitation with a pulsed field excites the magnetisation to a state of precession which then damps down until the magnetisation returns to lie along the equilibrium direction. The envelope of such an oscillation is determined by the damping of the magnetic system. By comparing the dynamics observed in the control sample (Fig. 5.3.1. (a)) with those from a Dy capped sample (Fig. 5.3.1. (b)) it is clear that the addition of the Dy cap has significantly increased the damping. Alternatively a CW microwave excitation is used to excite the sample to a state of steady precession whilst the bias field applied in-plane orthogonal to the microwave field is swept. By measuring at two specific pump and probe delays,  $\pi/2$  radians apart, it is then possible to acquire FMR curves whose lineshapes represent the *Re* and *Im* parts of the component of the

susceptibility tensor  $\chi_{xy}$ . Such curves show clear evidence of enhanced damping due to the addition of the Dy cap in the form of a broadening of the line width (compare Fig. 5.3.1. (c & d)).

With the enhanced damping at room temperature due to the addition of the Dy capping layer clearly demonstrated it is then interesting to note that bulk Dy is paramagnetic at room temperature<sup>58</sup> ( $T_{\text{Curie}} = 85 \text{ K}$ ,  $T_{\text{Néel}} = 179 \text{ K}$ ) and so it may be possible to further enhance the damping by cooling. To this end, time resolved measurements were performed with the low temperature TR-MOKE setup described earlier. FMR curves were measured with a 4 GHz CW excitation, the  $Im$  components of  $\chi_{xy}$  are shown in Fig. 5.3.2. The line width, resonance field and peak amplitude that are extracted by performing a Chi squared fit with a symmetric Lorentzian function are shown as well.



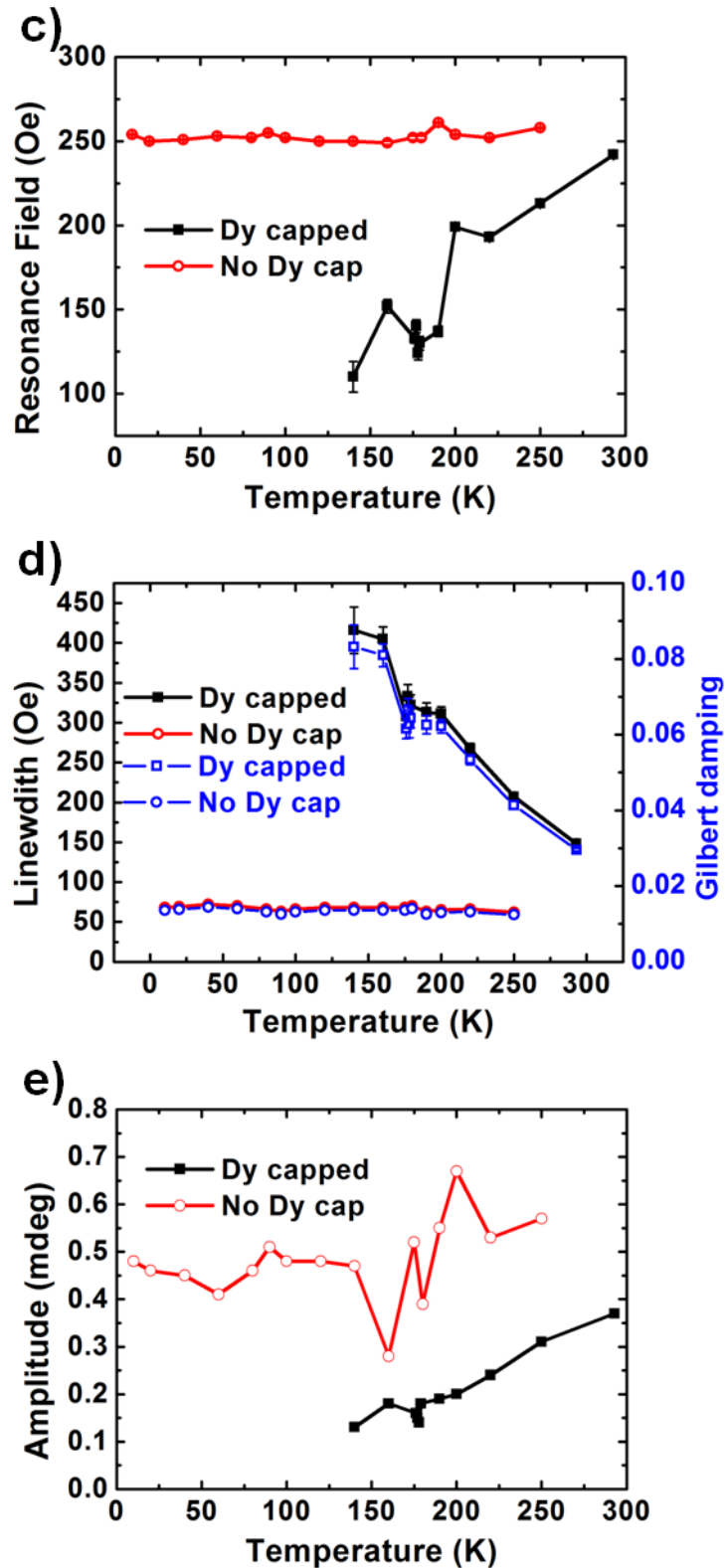


FIG. 5.3.2. (a)  $Im(\chi_{xy})$  FMR curves were measured, with a measurable signal occurring over the whole range of temperatures (10 – 250 K), for the control sample. (b) With the addition of a Dy capping layer the line width is broadened at room temperature and broadened further at low temperature. Dynamics become too heavily damped to be resolved below 140 K. (c) Lorentzian fitting was used to extract the resonance field, (d) line width and Gilbert damping and (e) amplitude for both samples. Cooling was performed at remanence for all measurements.

With the addition of a Dy capping layer the line width is broadened at room temperature relative to the control sample and then more so with decreasing temperature. Dynamics in the Dy capped sample become too heavily damped to be resolved below 140 K and so no extracted values are shown for these temperatures. The error bars on the points extracted from the Dy capped sample illustrate the sharp reduction in signal size as the temperature approaches 140 K. The extracted line width (Fig. 5.3.2. (c)) of the Dy capped sample increases approximately by a factor of 2 compared to its room temperature value whilst the line width of the control sample shows no temperature dependence within experimental error. A higher density of points was measured around the Néel temperature of bulk Dy (179 K). Nothing anomalous was observed at this temperature. This is unsurprising since the Néel temperature of a 1 nm thick film may be quite different to that of bulk Dy. The extracted resonance field (Fig. 5.3.2. (c)) decreases with decreasing temperature in the presence of the Dy cap. Again, no temperature dependence is seen in the control sample within experimental error. The amplitude falls off dramatically with decreasing temperature in the presence of the Dy cap until it falls below the noise floor of the experiment, as illustrated by the noise spectra for temperatures of 140 K and below (Fig. 5.3.2. (b)). A large variation in the amplitude of the control sample between 140 and 220 K suggests a temperature dependent variation of the impedance matching along the RF path which is specific to the control sample. Nevertheless this does not affect its dynamic properties, as shown by the flat temperature dependence in (c) and (d) and is therefore discounted as a significant trend. The strong variation in the line width, resonance field and amplitude observed in the Dy capped sample as a function of temperature clearly demonstrate enhanced damping. As no such variation is observed in the control sample it is apparent that this trend is due solely to the presence of the Dy capping layer.

To investigate the possible microscopic origins of this enhanced damping static XMCD characterisation was performed as a function of temperature for Ni and Dy (Fig. 5.3.3.). Dy XMCD spectra in fluorescence yield measured at a shallow grazing angle were measured as a function of temperature in the absence of a cooling field (Fig. 5.3.3. (a)). Measurements were made by flipping the saturated magnetisation along the x-ray wave vector with fixed x-ray polarisation. Whilst the Dy  $M_4$  peak is difficult to resolve there is a clear monotonic increase in the area under the  $M_5$  peak with decreasing temperature. Whilst the application of the XMCD sum rules to fluorescence measurements is complicated by the presence of self absorption effects<sup>51</sup>, the substantial

increase in the fluorescence signal serves to clearly indicate increased ferromagnetic ordering in the Dy cap as a result of cooling. Ni XMCD spectra (not shown) taken over the same temperature range show no such strong temperature variation. In addition hysteresis loops on the Dy  $M_5$  (Fig. 5.3.3. (b)) and Ni  $L_3$  edges (Fig. 5.3.3. (c)) were taken with fixed x-ray polarisation after cooling in a 5 kOe cooling field that was directed along the x-ray wave vector. The lack of an offset from zero field demonstrates that it was not possible to induce any measurable exchange bias. The Ni  $L_3$ <sup>59</sup> and Dy  $M_5$ <sup>60</sup> dichroisms are of opposite sign which means that the loops illustrate that there is a net anti parallel alignment between the ferromagnetically ordered Ni and ferromagnetically ordered Dy moments. This is in agreement with previous studies on Fe and Dy<sup>61</sup> alloys.

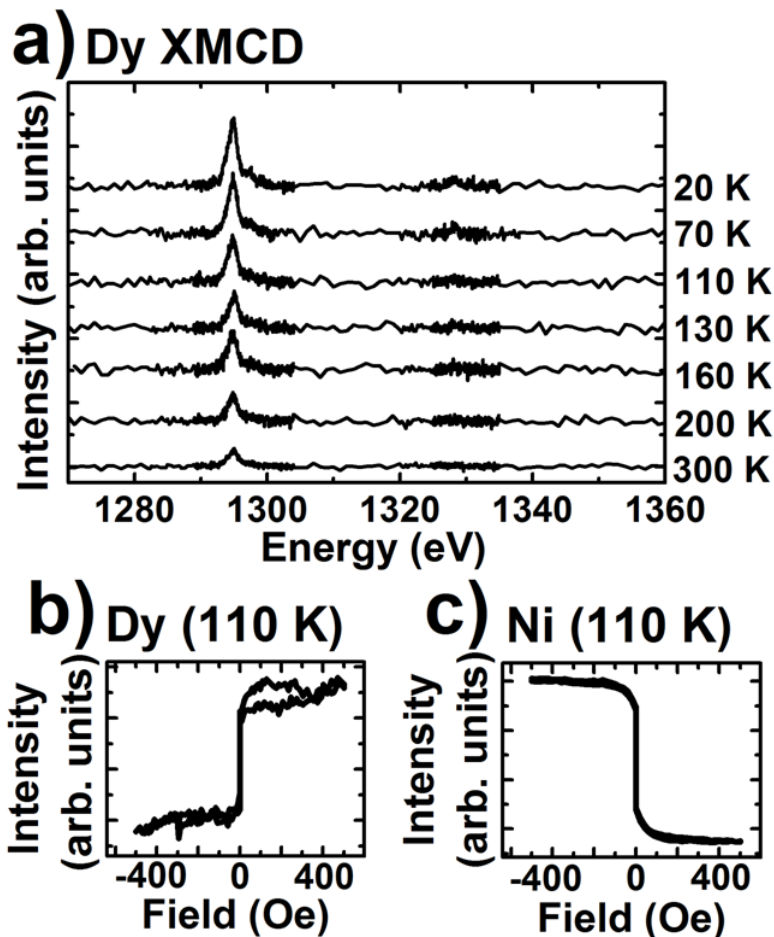


FIG. 5.3.3. (a) Dy XMCD spectra in fluorescence yield measured as a function of temperature, cooling was performed at remanence. The strong monotonic increase in the area under the Dy  $M_5$  peak indicates an increased ferromagnetic ordering of the Dy cap. (b) Dy  $M_5$  and (c) Ni  $L_3$  hysteresis loops taken after cooling in a 5 kOe cooling field directed along the x-ray wave vector show there is a net antiparallel alignment between the ferromagnetically ordered Dy and ferromagnetically ordered Ni moments. The loops also show that no exchange bias could be induced.

It is interesting that a Dy XMCD spectrum can be measured at room temperature at all as the Curie temperature of bulk Dy is 85 K. Whilst a detailed analysis of the crystal structure of the NiFe/Dy interface lies beyond the scope of this chapter it is noted that the ferromagnetic ordering in the Dy may result from either an intermixing of Dy, Ni and Fe atoms at the interface, or the interfacial exchange interaction across a sharp Dy/Fe interface.

Although a full explanation of the observed temperature dependent damping and resonant field utilising an analytical model remains a work in progress it is insightful to discuss the progress made towards a full description of the system under study during this PhD project. Firstly it is possible to experimentally rule out incoherent precession of Fe, Ni and Co spins in the Dy capped sample. Phase-resolved XFMR was used to measure the relative phase of precession of the Ni, Fe and Co moments at room temperature by setting the x-ray energy to that of each of the Ni, Fe and Co  $L_3$  edges in turn and varying the relative delay between the x-ray pulses and CW microwave excitation. The Dy signal lay below the noise floor of the experiment.

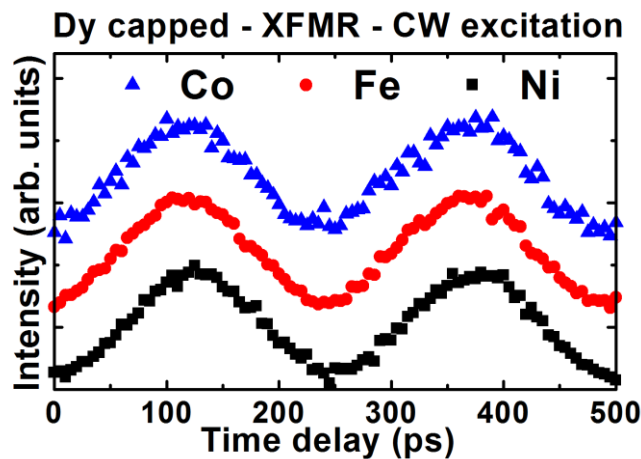


FIG. 5.3.4. Phase-resolved XFMR measurements combine the chemical sensitivity of XMCD with picosecond temporal resolution. Room temperature measurements on the Dy capped sample confirm that the Ni, Fe and Co precess in phase with one another.

No phase lag between the transition metal moments was observed at room temperature due to the dominant exchange interaction and so incoherent precession of the Ni, Fe and Co spins cannot explain the enhanced damping shown in this chapter.

Secondly it is possible to experimentally rule out the change in the dynamic behaviour being caused chiefly by a change in the magnetisation of the sample as a whole.

Vibrating Sample Magnetometry (VSM) measurements were made on continuous films deposited on glass cover slips by collaborators at HGST to look for a change in the magnetisation as a function of temperature.

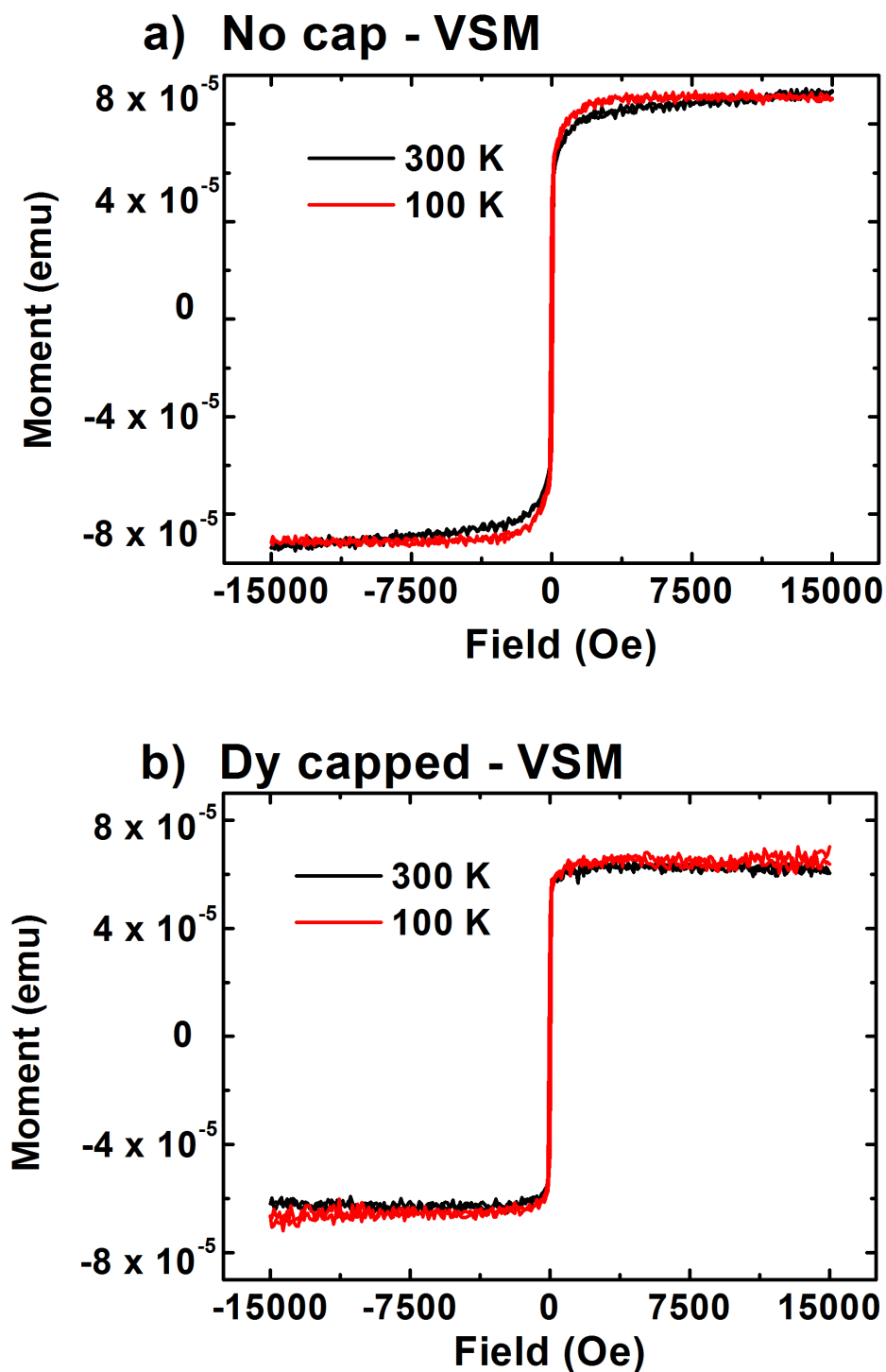


Fig. 5.3.5 (a) VSM measurements on the control sample show an increase of approximately 10% in the magnetisation, for the range of fields measured with FMR, when the sample is cooled from room temperature to 100 K. (b) No appreciable change is seen in the magnetisation of the Dy capped sample when it is cooled from room temperature to 100 K.

The VSM data in Fig. 5.3.5 appears to show that the magnetisation of the control sample increases by approximately 10% when cooled from room temperature to 100 K for the field range over which the FMR measurements were made. This is thought to be an artefact as a result of measuring with a brass sample holder. The Dy capped sample on the other hand was measured with a plastic sample holder and shows almost no change. The moment in the Dy capped sample is seen to be smaller than that in the control sample, this is to be expected as the Dy moments align anti parallel with the Ni moments and so a partial cancellation occurs. This is attributed to the increased ferromagnetic ordering of the Dy cap with reduced temperature, which was shown above in Fig. 5.3.3. to align anti parallel with the Ni moments. It is noted that the loops from the control sample at 300 K do not saturate until  $\sim 10$  kOe – an extremely high value for such a sample. This is attributed to the use of a brass sample holder causing an artefact in the measurement. A plastic sample holder was used for measurements on the Dy capped sample and no such artefact was observed.

Finally, it may be the case that heavily damped dynamics observed in the Dy capped sample require that extra care be taken over the assumptions made in deriving equations for the AC magnetic susceptibility. It may no longer be a valid approach to drop terms in the Gilbert damping parameter in the Kittel curve as the system is heavily damped (Appendix 2). To test this idea analytical modelling of the FMR response of permalloy at 4 GHz was performed. Results showed that it was not possible to shift the resonance field even when the Gilbert damping was increased to 0.50, at which point dynamics could no longer be excited.

## 5.4 Conclusion

In conclusion, a variety of phase and temperature resolved measurements on industrially relevant spin valve free layer stacks motivated by the work of Maat<sup>53</sup> *et al.* have been presented. Clear evidence of enhanced damping in a Dy capped sample has been shown, as compared to a control sample. FMR curves measured at different temperatures (Fig. 5.3.2.) show an enhanced damping with decreasing temperature. The strong temperature dependent damping in Fig. 5.3.2 is attributed to the increased magnetic ordering that occurs in the Dy cap as it is cooled (Fig. 5.3.3.). A number of possible explanations for the interesting effects that this has on the FMR response were then discussed.

## Chapter 6: Phase-resolved XFMR measurements of spin pumping in spin valves

Measurements of the spin pumping effect predicted by Tserkovnyak<sup>20</sup> *et al.* on spin valve stacks of immediate practical interest are presented in this chapter. Phase-resolved X-ray Ferromagnetic Resonance (XFMR) is used to measure the dynamic behaviour of the free and fixed layers with a timing resolution of just a few picoseconds. A clear signature of STT coupling between the free and fixed layers is discussed and then observed in both experiment and modelling for a spacer that lay in the spin ballistic regime. The STT coupling could then be completely destroyed by inserting a strong spin scattering layer into the NM spacer.

### 6.1 Historical development of spin pumping studies

The Gilbert damping has received much study in recent years, both experimentally and theoretically. Of particular note are experimental investigations of how the Gilbert damping is affected by depositing a normal metal (NM) on top of a ferromagnetic thin film. Studies on Cu/Co<sup>62</sup> and Pt/Co<sup>63</sup> showed that not only is the Gilbert damping enhanced in such structures but that the size of the enhancement is dependent upon the choice of the NM. Early attempts to explain the observed effects have invoked an enhancement of the electron-magnon scattering at the interface<sup>18</sup> or a thermokinetic approach<sup>64</sup>. Also of note is an earlier study based on the interpretation of experimental Transmission-Electron Spin Resonance (TESR) results<sup>65</sup>.

In 2002 Tserkovnyak<sup>20</sup> *et al.* proposed a mechanism by which a precessing magnetic moment could pump a pure spin current (spin-pumping) into an adjacent NM layer. If the NM is placed between two ferromagnetic films, as in the case of a spin valve structure, then the transverse component of the pure spin current can be absorbed by the second ferromagnetic layer (spin sink). The absorption of spin angular momentum by the spin sink generates a torque term acting on the magnetisation of that layer due to conservation of angular momentum. The first experimental evidence of this theory was seen in Ferromagnetic Resonance (FMR) measurements of the line width broadening of the spin pumping layer due as it pumped angular momentum into the NM layer<sup>66</sup>. More recently the dynamics induced in the spin sink have been measured by Time Resolved Magneto Optical Kerr Effect (TR-MOKE) measurements<sup>67</sup>. The structures measured so

far have covered a wide range of transport regimes<sup>68</sup>, from spin ballistic to strongly spin diffusive. The experimental study presented in this chapter extends the existing body of literature on spin-pumping by presenting XFMR measurements performed on spin valve stacks of immediate practical interest. XFMR is a suitable technique for such measurements as it allows the phase of precession of the free and fixed layers in a spin valve to be characterised. The phase is of particular interest as it is particularly sensitive to Spin Transfer Torque (STT) phenomena, as will be discussed in this chapter.

## 6.2 Experimental details

A Ta(5)/ [Cu(25)/Ta(3)]<sub>3</sub>/ Cu(25)/ Ta(5)/ Ru(10)/ Ta(3)/ Ru(2)/ Ir<sub>80</sub>Mn<sub>20</sub>(6)/ Co<sub>50</sub>Fe<sub>50</sub>(3)/ Cu(6)/ Ni<sub>80</sub>Fe<sub>20</sub>(5)/ Ru(7) stack (thicknesses in nanometers) was magnetron sputtered onto an insulating sapphire substrate of 500  $\mu\text{m}$  thickness. The IrMn layer is antiferromagnetic at room temperature and the stack was field annealed to give an exchange bias field along the symmetry axis of the CPW (collinear with the applied bias field). The CoFe layer is then referred to as the fixed layer or spin sink and the permalloy as the free layer or spin pump. The 6 nm thick Cu spacer is thin compared to the spin diffusion length in Cu which has been found experimentally to be 350 nm<sup>69</sup>. This puts the valve stack in the spin ballistic regime where a pure spin current can be assumed to be unattenuated as it passes from the spin pump to the spin sink layer. A second stack was identical except for the insertion of a Ta layer in the Cu spacer, the valve structure was then of the form: Ir<sub>80</sub>Mn<sub>20</sub>(6)/ Co<sub>50</sub>Fe<sub>50</sub>(3)/ Cu(2.5)/ Ta(1)/ Cu(2.5)/ Ni<sub>80</sub>Fe<sub>20</sub>(5)/ Ru(7). Ta is known to be a strong spin scatter and so was inserted into the NM spacer with the intent of fully depolarizing any electron spin current pumped into the Cu before it reaches the spin sink. This second valve stack therefore acts as a control sample where it is expected that no STT induced dynamics will be observed in the spin sink. The wafer stacks were chosen to be representative of spin valve stacks currently being used in high density recording heads fabricated by collaborators at Hitachi Global Storage Technologies (HGST). Magnetic elements of lateral dimensions 190  $\mu\text{m}$  x 400  $\mu\text{m}$  were defined on top of the Cu/Ta underlayer by a combination of ion beam milling and electron beam lithography. Photolithography was then employed to pattern the exposed Cu into a Coplanar Waveguide (CPW) structure of 50  $\Omega$  characteristic impedance. The aspect ratio of the samples is sufficient to avoid any spatially inhomogeneous dynamics due to edge effects. A 5  $\mu\text{m}$  border was left between the edges of the sample element and the central track to avoid any sizable out-of-plane excitation. The reader is referred to chapter 3 for a scale drawing of the device.

Phase-resolved measurements were made with the XFMR setup in fluorescence yield<sup>25</sup> that was detailed in chapter 3 so as to make element specific measurements with a resolution of just a few picoseconds. A Continuous Wave (CW) Radio Frequency (RF) field, phase locked to the synchrotron's x-ray pulse train, was used to drive the magnetisation into a state of steady precession about an in-plane bias field. The experimental geometry is shown below in Fig. 6.2.1.

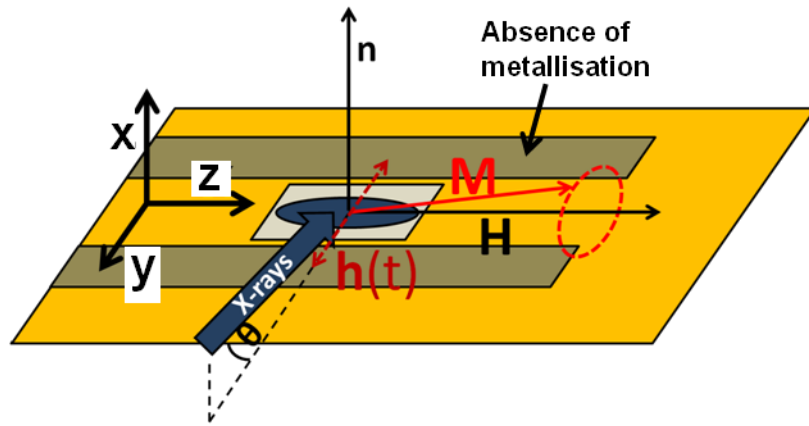


FIG. 6.2.1 A schematic of the experimental geometry used to make phase-resolved XFMR measurements. The magnetisation ( $M$ ) is forced into a state of steady precession about the applied bias field ( $H$ ) by an in-plane continuous wave RF magnetic field ( $h(t)$ ). The probe beam is at grazing incidence to detect the large in-plane oscillatory component of the magnetisation.

Previous studies of the STT induced dynamics in the spin sink have been made with TR-MOKE measurements where the spacer layer was chosen to be thick enough so as to block any MOKE signal from the bottom layer<sup>67,70</sup>. Some studies also used a rotatable compensator to cancel the signal from the bottom layer<sup>67</sup>. As XFMR utilises the chemical specificity of XMCD such experimental limitations are readily avoided by tuning the x-ray energy to that of the Co  $L_3$  edge (spin sink) or the Ni  $L_3$  edge (spin pump).

### 6.3 Spin pumping theory

Before embarking on a detailed discussion of the experimental results it is insightful to first highlight the signatures of spin-pumping. The theory of Tserkovnyak<sup>20</sup> *et al.* predicts two dynamic effects<sup>71</sup>. The first prediction is line width broadening of the spin pumping layer. The spin pumping layer can be thought of as an oscillator that is “leaking” angular momentum into the adjacent NM. This results in an additional Gilbert-like damping term acting on the magnetisation of the spin pump layer which broadens the FMR response. When a pure spin current is pumped into the NM layer spin accumulation occurs resulting in a spin-split chemical potential which is a higher energy state for the NM. For the spin-splitting of the chemical potential to be invoked it is required that there be a globally diffuse momentum distribution in the NM so that the occupation of the electronic states in the NM is still governed by Fermi-Dirac statistics. Such a momentum distribution can arise due to diffuse scattering at interfaces. It has been shown experimentally that diffuse interfacial scattering of the itinerant electrons in the NM can occur even in polycrystalline samples where the spacer thickness lies in the ballistic regime<sup>72</sup>. As there is no preferred direction for spin diffusion in the NM, half of the accumulated spin flows into the spin sink whilst the other half flows back to the spin pumping layer. The latter is known as spin back flow and partially compensates for the spin pumping into the NM. Due to the short spin coherence length (<1 nm) in the 3d transition metal ferromagnets, the simplifying assumption that the spin current is completely absorbed at the interface is made. The absorption of angular momentum by the spin sink results in the second dynamic effect predicted by the spin-pumping theory; that there will be a torque term acting on the spin sink magnetisation generated by the absorption of the transverse component of a pure spin current by that layer. The equations of motion for such a system take the form of a pair of coupled Landau-Lifshitz-Gilbert (LLG) equations that are modified to include the spin-pumping terms

$$\begin{aligned} \frac{\partial \mathbf{m}_i}{\partial t} = & -\gamma_i [\mathbf{m}_i \times \mathbf{H}_{eff,i}] + \alpha_i^{(0)} \left[ \mathbf{m}_i \times \frac{\partial \mathbf{m}_i}{\partial t} \right] \\ & + \alpha_i^{SP} \left[ \mathbf{m}_i \times \frac{\partial \mathbf{m}_i}{\partial t} - \mathbf{m}_j \times \frac{\partial \mathbf{m}_j}{\partial t} \right] \end{aligned} \quad (6.3.1)$$

where the free layer is denoted  $i = 1$ , the fixed layer  $j = 2$  and  $\mathbf{m}_i$  is the magnetisation unit vector. The LLG equation describing the fixed layer dynamics is obtained by swapping the indices in equation 6.3.1. The first term on the right hand side is the

torque term due to the effective field while the second term is the damping term first proposed by Gilbert. The third term describes the enhanced damping due to spin pumping into the NM. The negative sign of the fourth term means that it represents the dynamics induced by the absorption of a spin current pumped from the other layer, the study of which is the main focus of this chapter.

Additional insight into the affect of spin-pumping on the fixed layer dynamics can be gained by constructing a vector diagram showing the different terms acting on the fixed layer magnetisation unit vector  $m_2$ .

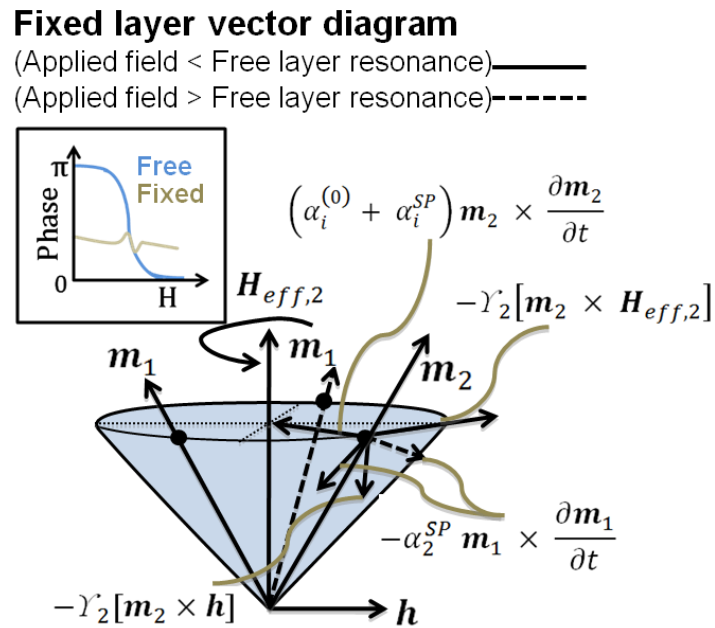


FIG. 6.3.1 A vector diagram showing the terms acting on the fixed layer magnetisation ( $m_2$ ) for cases where the applied field is above, and below the free layer resonance field respectively. (Inset) The reorientation of the spin-pumping term causes a change in the phase of the fixed layer as a function of applied field.

The vector diagram in Fig. 6.3.1 shows the terms acting on the fixed layer magnetisation when the applied field is above, or below the free layer resonance. The fixed layer is assumed to be heavily damped such that its phase relative to the driving field is broadened greatly with respect to that of the free layer. It is noted that the orientation of the spin-pumping term is different in the two cases which changes the superposition of the spin-pumping and RF excitation torques acting on the fixed layer magnetisation. Either side of the free layer resonance field there is a clear difference in the direction of their resultant vector. Below the free layer resonance the phase

difference between the fixed layer and the driving field will increase as the spin-pumping term partially opposes the torque term due to the RF excitation. This is in contrast to the case where the applied field is greater than the free layer resonance. In this case the phase difference between the fixed layer and the driving field will decrease as the spin-pumping is now partially adding to the torque term due to the RF excitation. It is then noted that the spin-pumping effect is largest near the free layer resonance and so to a good first approximation the width of such a feature will be equal to that of the FWHM of the free layer resonance. Outside of this range of applied field values the fixed layer phase will then monotonically return to the background phase relative to the driving field that results from direct excitation of the fixed layer by the RF excitation. At some applied bias field value the phase of the free and fixed layers relative to the driving field will be the same and the STT effects will vanish resulting in a nodal point in the phase. In the presence of spin-pumping we then expect to see a bipolar feature in the fixed layer phase relative to the driving field whose centre value and peak-to-peak linewidth are related to those of the free layer resonance. This is shown in schematic form in the inset in Fig. 6.3.1

## 6.4 Experimental results

It was first necessary to characterise the static properties of both spin-valve stacks by using the Magneto Optical Kerr Effect (MOKE) in the longitudinal geometry to measure hysteresis loops. The resulting loops therefore provide information on the in-plane magnetisation and allow a value for the exchange bias field to be determined.

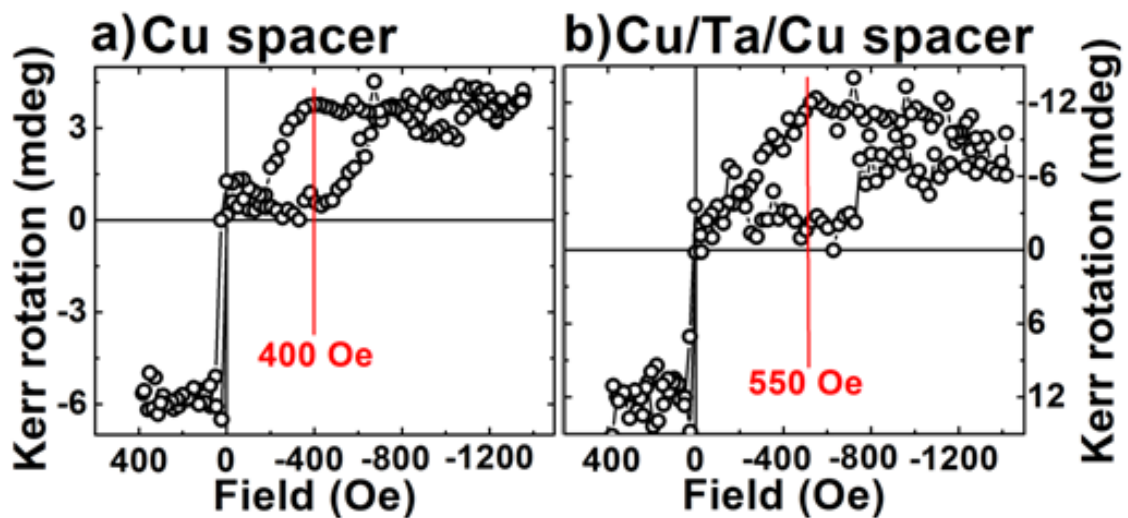


FIG. 6.4.1 Hysteresis loops measured with longitudinal MOKE after x-ray irradiation during XFMR measurements for (a) the valve with Cu spacer (b) the control sample with Cu/Ta/Cu spacer.

Measurements taken after the completion of the XFMR measurements (Fig. 6.4.1 (a) & (b)) show the exchange bias field to be 400 Oe and 550 Oe for the valve with Cu spacer and the valve with Cu/Ta/Cu spacer respectively. All dynamic measurements presented in this chapter were performed in quadrant 2 of the above loops. This corresponds to the case where the free and fixed layer magnetisations are parallel.

As the spin pumping effect is predicted to be largest when the spin pump (free layer) is resonating<sup>20,71</sup> it is necessary to identify the free layer resonance condition. The  $Im$  component of the AC magnetic susceptibility component  $\chi_{yy}$  can be measured by setting the pump-probe delay to the specific value that allows the component of the precessing magnetisation that is  $\pi/2$  out of phase with the driving field at resonance to be measured, and sweeping the applied bias field along the symmetry axis of the CPW. Examples for both valves are shown below in Fig. 6.4.2. It is noted that it was not possible to obtain a fixed layer resonance curve from either valve structure. This is attributed to a very large damping resulting from the fixed layer being in direct contact with the IrMn.

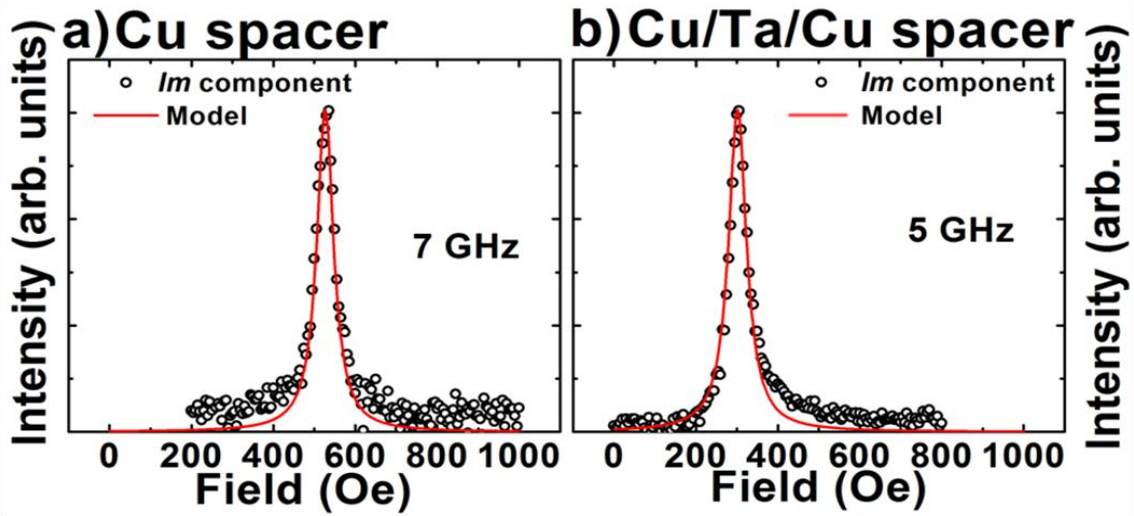


FIG. 6.4.2 (a) The  $Im$  component of the AC magnetic susceptibility component  $\chi_{yy}$  from the free layer (spin pump) of the valve with Cu spacer and (b) for the control sample. The linewidth is determined by the combined effect of intrinsic Gilbert damping ( $\alpha^{(0)}_l$ ) and the additional Gilbert-like damping term due to spin pumping ( $\alpha^{SP}_l$ ).

The linewidth extracted with Lorentzian fitting is found to be the same for the two samples within the experimental error of a few Oe. The linewidth of 50 Oe corresponds

to a damping parameter of 0.0105 that is a combination of the intrinsic Gilbert damping of the spin pump ( $\alpha^{(0)}_I$ ) and the additional Gilbert-like damping term due to spin pumping ( $\alpha^{SP}_I$ ). Despite extensive attempts to ensure that the RF path to the sample was of 50  $\Omega$  characteristic impedance throughout, it was found during the experiments that there was a significant increase in the RF loss at particular excitation frequencies. The frequency dependence of the RF loss was found to change when a new sample waveguide was loaded as doing so requires a new set of Ag paint contacts to be made to the sample CPW. Optimum excitation frequencies of 7 and 5 GHz were found for the samples in Fig. 6.4.2 (a) and (b) respectively.

Although no attempt is made in this chapter to separate the two damping terms it is noted that the intrinsic Gilbert damping will have only have a weak frequency dependence over the range 5 – 7 GHz and so to a good first approximation it is the same for the FMR curves in Fig. 6.4.2 (a) & (b). This was confirmed by VNA-FMR measurements (not shown) which showed no appreciable difference in linewidth over the range 5 - 7 GHz when the FMR curves were overlaid. This then implies that  $\alpha^{SP}_I$  is the same for both samples, which in itself is an interesting result. In the sample with the Cu spacer the fixed layer sinks the transverse component of the pure spin current. This is in contrast to the control sample where the Ta spacer layer completely randomises the spin by transferring angular momentum to the lattice. This indicates that the pure spin current pumped into the Cu is predominantly transverse (to the polarisation of the FM layers) and so this result is a clear experimental demonstration that the spin-pumping layer is precessing in the small angle regime. The Gilbert-like spin-pumping terms are of the form<sup>72</sup>

$$\alpha_i^{SP} = \frac{g\mu_B g_{\uparrow\downarrow}}{4\pi M_i d_i} \quad (6.4.1)$$

where  $M_i$  is the saturation magnetisation,  $d_i$  is the thickness,  $g$  the spectroscopic g-factor,  $\mu_B$  the Bohr magneton and  $g_{\uparrow\downarrow}$  is the *Re* component of the spin-mixing conductance.

While it was not possible to obtain the *Im* component of  $\chi_{yy}$  for the fixed layer (spin sink) it was possible to obtain a series of delay scans at different applied fields. Delay scans at different applied bias field values from the fixed layer in both valve stacks are shown below in Fig. 6.4.3

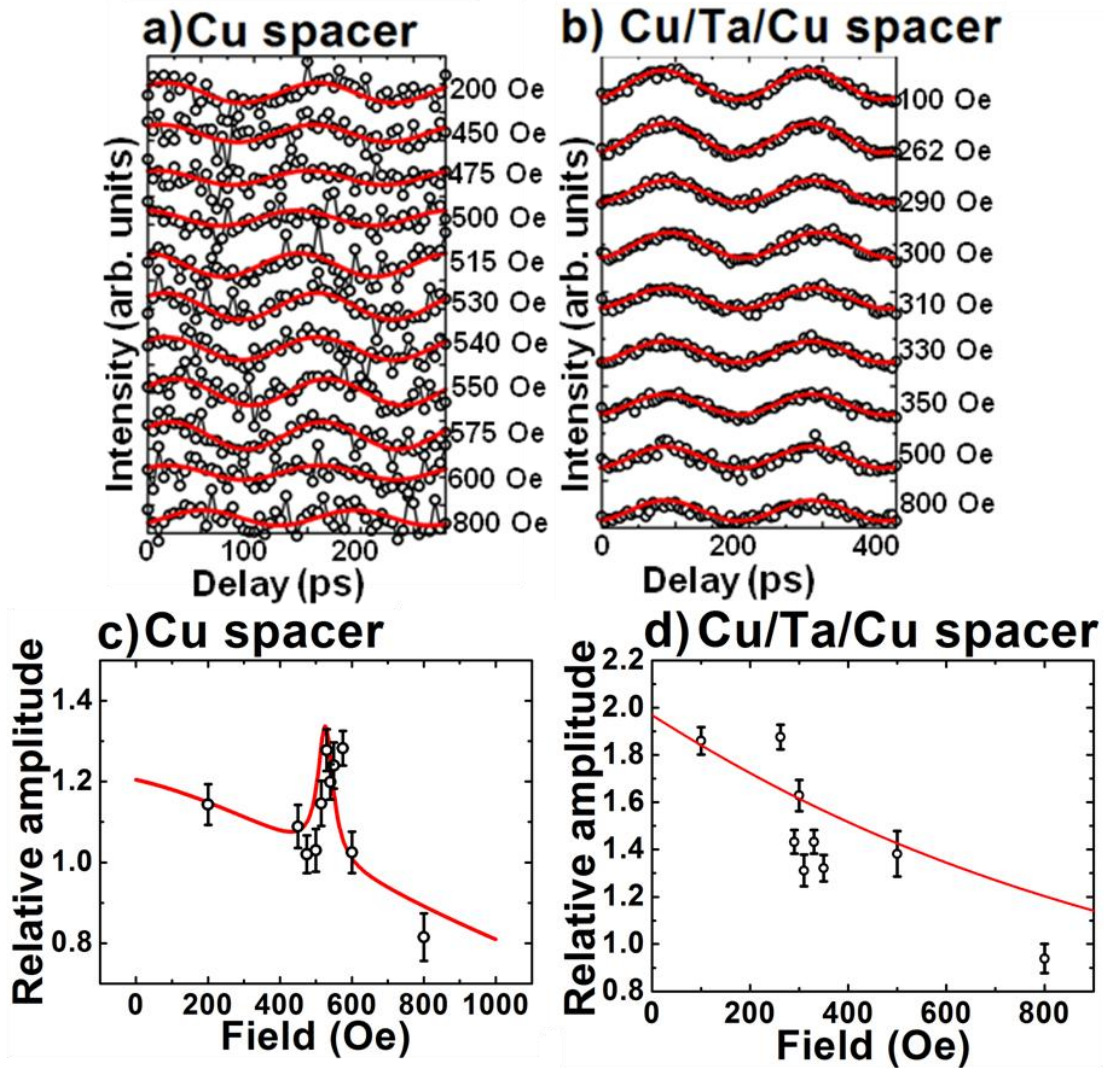


FIG. 6.4.3. (a) Fixed layer (spin sink) delay scans (7 GHz excitation) at different applied bias fields for the valve with a Cu spacer. A strong variation in the phase is seen for different applied bias field values. The amplitude is also seen to increase near to the free layer resonance field (530 Oe) as shown in (c). (b) Fixed layer (spin sink) delay scans (5 GHz excitation) at different applied bias fields for the control sample. No variation in the phase (or amplitude (d)) is seen as the bias field is swept through the free layer resonance. Red lines are sinusoidal fits to the data where the period is constrained to be equal to that of the RF excitation.

There are marked differences between Fig. 6.4.3 (a) & (b) in terms of the phase and amplitude as a function of applied bias field. The amplitude of the delay scans in Fig. 6.4.3 is dependent on the in-plane cone angle, which is dependent on the excitation frequency for a fixed RF power. In addition the loss in the RF cables is frequency dependent. As a result the amplitudes of the two datasets (Fig. 6.4.3 (a) & (b)) are not directly comparable. Instead the amplitudes extracted with sinusoidal fitting are normalised to the smallest extracted amplitude in each dataset and plotted as a function

of applied field (Fig. 6.4.3 (c) & (d)). For the sample with the Cu spacer (Fig. 6.4.3 (c)) a clear increase of the fixed layer amplitude is seen to occur for applied field values lying within the FWHM of the free layer resonance. In addition there is a sloping background level due to the direct excitation of the fixed layer by the RF excitation. This is in stark contrast to the control sample (Fig. 6.4.3 (d)) where no such feature is seen at the free layer resonance. Whilst the difference between the extracted amplitudes indicates the presence of STT coupling, an even clearer indication is seen in the variation of the phase as a function of applied field. For the control sample (Fig. 6.4.3 (b)) there is no strong dependence of the phase of the sinusoidal fits on the applied bias field. This is not so for the valve with Cu spacer (Fig. 6.4.3 (a)) where there is a clear bipolar variation in the phase, centred on 530 Oe (the free layer resonance field). The variation in phase as a function of applied bias field is the key result obtained from the measurements presented in this chapter and is the clearest indicator of the presence of STT coupling. By using the sinusoidal fits shown in Fig. 6.4.3 the phase of the precession of the fixed layer relative to the driving field was plotted as a function of the applied bias field. The difference in signal-to-noise of the two datasets is attributed to the larger in-plane cone angle at 5 GHz. The same process was repeated for the free layer in both sample stacks.

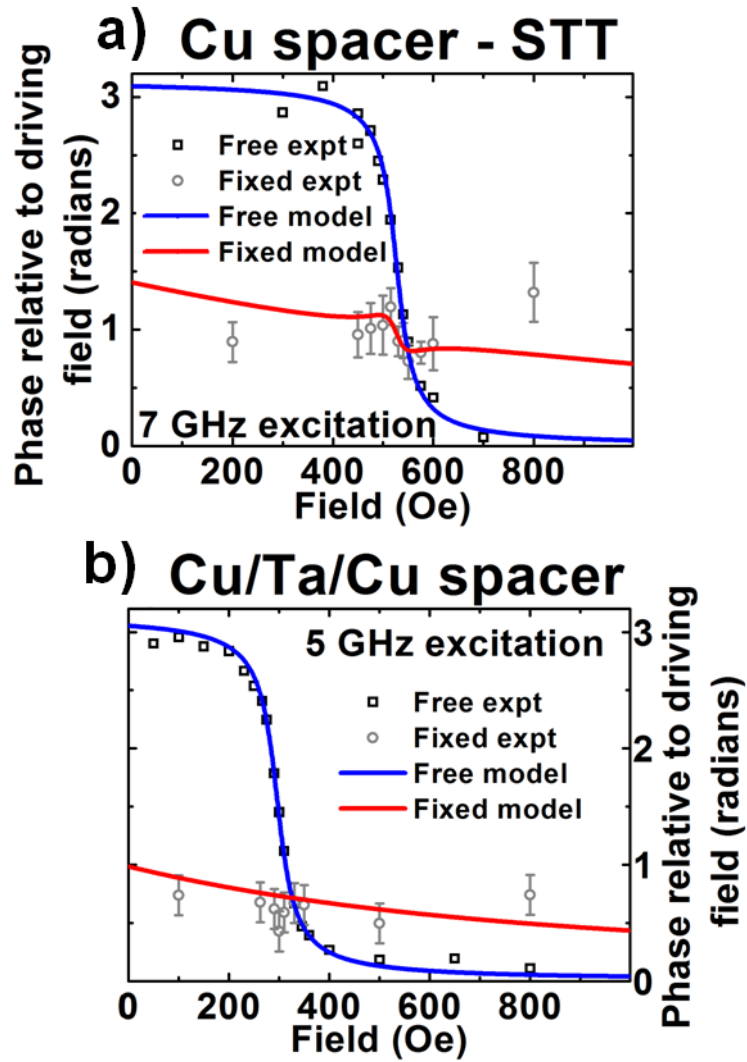


FIG. 6.4.4 (a) The experimental and modelled phase relative to the driving field of the response of the free layer and fixed layers are shown for the valve with Cu spacer. The fixed layer phase shows a bipolar response about the free layer resonance field indicative of STT coupling as predicted from (Fig. 6.3.1) The peak-to-peak width of the bipolar feature matches the FWHM of the free layer resonance (50 Oe). (b) The experimental and modelled phase relative to the driving field of the response of the free layer and fixed layers are shown for the control sample. The fixed layer phase shows no deviation at the free layer resonance field from its broad sigmoidal response that is indicative of very heavily damped SHO. For (a) the following modelling parameters were used;  $\alpha^{SP}_1 = 0.0050$  and  $\alpha^{SP}_2 = 0.0034$ . For (b) the following modelling parameters were used;  $\alpha^{SP}_1 = 0.010$  and  $\alpha^{SP}_2 = 0.0068$ .

While the free layer response shows a sigmoidal response typical of a SHO for both Fig. 6.4.4 (a) & (b), the fixed layer response is markedly different between the two valve stacks. For the valve with the Cu spacer (Fig. 6.4.4 (a)) there is a clear bipolar feature in the fixed layer phase superimposed on top of the broad sloping background. This feature is centred on the free layer resonance field and is a clear signature of STT as

outlined in Fig. 6.3.1 It is then interesting to make the comparison with the fixed layer response observed in the control sample (Fig. 6.4.4 (b)). The fixed layer response is indicative of a broad sigmoidal response due to very heavily damped SHO and no bipolar variation is seen indicating that the Ta layer has strongly scattered the pure spin current and so destroyed any STT coupling between the two layers. There is a possible indication of a small negative dip in the fixed layer phase at the free layer resonance field. This is indicative of dipolar coupling between the two layers resulting from interfacial roughness. If such a feature is present then it lies within the size of the error bars of the extracted phases and so no attempt is made to quantify the size of this effect. The phase plots in Fig. 6.4.4 show that the resonances of the two layers partially overlap, meaning that both layers are being driven to some extent by the RF excitation. This is why it is possible to measure a fixed layer delay scan several hundred Oe away from the free layer resonance field. This is an illustration of the additional considerations that must be made when extending the existing body of work to structures of immediate practical interest that have not been tailored with a specific experimental setup in mind. In addition to this clear experimental demonstration of the existence of STT coupling an attempt to model the observed response of the two samples has been made and will now be detailed.

## 6.5 Modelling discussion

The extracted line widths in Fig. 4 constrain the sum of the intrinsic damping ( $\alpha^{(0)}_1$ ) and the additional Gilbert-like damping term due to spin pumping ( $\alpha^{SP}_1$ ) of the free layer in the valve with Cu spacer to be 0.0105 whilst for the control sample it is 0.0150. Equation 6.4.1. shows that the relative size of the spin-pumping Gilbert-like terms acting on the two layers is related by the magnetisation and thickness of the respective layers. Values for the saturation magnetisation of the free and fixed layers were found to be 815 emu cm<sup>-3</sup> and 2017 emu cm<sup>-3</sup> respectively by means of Vibrating Sample Magnetometry (VSM). The VSM measurements were performed by collaborators at HGST. The relative size of  $\alpha^{SP}_1$  and  $\alpha^{(0)}_1$  was then varied subject to the constraint that their sum must equal that determined above (Fig. 6.4.2). The best agreement between the modelled curves and experimental data shown in Fig. 6.4.4 (a) was found when  $\alpha^{(0)}_1 = 0.0055$  and  $\alpha^{SP}_1 = 0.0050$ . This then constrains  $\alpha^{SP}_2 = 0.0034$ . An intrinsic Gilbert damping of 0.0055 for permalloy is in agreement with the range of values for this parameter reported in the literature<sup>73</sup>. The values for  $\alpha^{SP}_1$  and  $\alpha^{SP}_2$  are comparable to those found in previous spin-pumping studies ( $3-5 \times 10^{-3}$ )<sup>67</sup>. As no

evidence of STT was observed in the experiment for the control sample the 4<sup>th</sup> term on the right hand side of equation 6.3.1 was set to zero for both layers to mimic the effect of the strong spin scattering of the Ta layer. In both samples no dipolar coupling due to interfacial roughness was included and the value of the exchange bias field was taken as the value obtained from hysteresis loops taken after x-ray measurements (Fig. 6.4.1 (a) & (b)). The exchange biased fixed layer was too heavily damped for a value of the fixed layer intrinsic damping ( $\alpha^{(0)}_2$ ) to be reliably extracted.  $\alpha^{(0)}_2$  was therefore used as a tuneable parameter (taking the values; 0.45 and 0.35 for the Cu spacer valve and control sample respectively) which in conjunction with the measured values for the exchange bias field set the background level of the fixed layer response that was due to direct excitation by the RF field. The effect of exchange bias on the intrinsic Gilbert damping is an area that has started to receive attention in recent years. It has been shown experimentally<sup>74</sup> in an interesting study on Ni<sub>81</sub>Fe<sub>19</sub>/Fe<sub>50</sub>Mn<sub>50</sub> that the Gilbert damping of the NiFe layer scales linearly from 0.008 – 0.05 when the exchange bias field is increased from 0 – 120 Oe. Extrapolating this relationship to encompass the exchange bias values measured in this study (Fig. 6.4.1) yields values of the intrinsic Gilbert damping in the NiFe that are of the same order as the CoFe intrinsic damping values used above for modelling. It is noted that it was only possible to recreate the peak-to-peak height of the bipolar feature in the fixed layer phase (Fig. 6.4.4 (a)) by subtracting a complex background, due to RF pickup. This then allowed all measured curves to be accurately modelled simultaneously. It is also possible to obtain a value for the *Re* component of the spin-mixing conductance,  $g_{\uparrow\downarrow}$  in Cu.  $g_{\uparrow\downarrow}$  is related to the number of conducting channels per spin in the Cu spacer and is a measure of the spin-pumping efficiency. The larger  $g_{\uparrow\downarrow}$  the more efficiently the spin-pump will pump spins in to the NM layer<sup>75</sup>. By rearranging equation 6.4.1 and using the modelled value of  $\alpha^{SP}_1$  one obtains a value of  $g_{\uparrow\downarrow} = 1.32 \times 10^{15} \text{ cm}^{-2}$  for Cu. It is noted that in the existing literature on spin-pumping there are two approximate expressions that relate the spin-mixing conductance to the number of electrons per spin in the NM ( $n$ ). In reference 68 the approximation  $g_{\uparrow\downarrow} \approx 1.2n^{2/3}$  is made whereas an alternative approximation of  $g_{\uparrow\downarrow} \approx 0.75n^{2/3}$  is presented elsewhere<sup>76</sup>. By assuming an electron density per spin of  $4.25 \times 10^{22} \text{ cm}^{-3}$  in Cu<sup>77</sup> one obtains estimates for  $g_{\uparrow\downarrow}$  in units of  $e^2/h$  in Cu of  $1.46 \times 10^{15} \text{ cm}^{-2}$  and  $0.91 \times 10^{15} \text{ cm}^{-2}$  respectively. As has been discussed in detail by Tserkovnyak<sup>71</sup> the measured spin-mixing conductance contains a contact resistance term known as the Sharvin conductance and so the value obtained from modelling should be renormalised. Doing so requires ab-initio calculations and a knowledge of the interfacial mixing that

lies beyond the scope of this study. Regardless, the experimental and modelled phase curves shown in Fig. 6.4.4 show that the relative size of the STT coupling can be compared in structures with different stack compositions.

## **6.6 Conclusion**

In this chapter first measurements of the spin pumping effect predicted by Tserkovnyak<sup>20</sup> *et al.* on spin valve stacks of immediate practical interest have been presented. A clear signature of STT coupling between the free and fixed layers was observed for a spacer that lay in the spin ballistic regime. The STT coupling could then be completely destroyed by inserting a strong spin scattering layer into the NM spacer. Modelled phase curves recreated the key features observed in experiment and the parameters used were justified and discussed in detail. This study serves to illustrate the rich variety of physics present in such samples and is of interest to both researchers studying spin pumping on a fundamental level and device physicists focused on industrial applications. In addition it has shown that phase-resolved XFMR provides a powerful experimental tool for determining the effectiveness of spin-scattering layers.

## Chapter 7: Establishing TR-XPEEM at the Diamond Light Source

A significant part of this PhD project was spent developing Time-Resolved X-ray Photoemission Electron Microscopy (TR-XPEEM) on beamline I06 at the Diamond Light Source. XPEEM is an imaging technique that utilises X-ray Magnetic Circular Dichroism (XMCD) to take images with magnetic contrast<sup>78,79,80</sup>. The purpose of this chapter is to describe the progress made towards establishing TR-XPEEM on beamline I06.

### 7.1 Motivation and sample details

As well as demonstrating the feasibility of TR-XPEEM measurements at the Diamond Light Source for the first time the broader aim of this study was to then use TR-XPEEM to study the precession and the gyration of magnetic vortex cores in isolated ferromagnetic elements. This is interesting as both processes have been found to be integral to the operation of nano-scale devices<sup>81</sup>. The magnetic contrast available with XPEEM may then shed new light on these fundamental phenomena. The vortex cores were an ideal subject for a first study since the vortex generates a large magnetic contrast in the acquired XPEEM images, and is observable in both micro- and nano-scale elements<sup>46,82</sup>. The development of this technique is of general importance for the magnetism and spintronics communities since it is particularly well suited to the study of non-local spin transfer torque phenomena.

Measurements were performed in the I06 PEEM end station on samples fabricated at the Hitachi San Jose Research Centre. Square, rectangular, circular and elliptical elements of lateral dimensions ranging from 250 nm to 10  $\mu\text{m}$  were deposited onto the central track of a CPW of 50  $\Omega$  characteristic impedance. CPWs with 6  $\mu\text{m}$  and 30  $\mu\text{m}$  central track width were fabricated and each was terminated by a NiCr thin film resistor that had a nominal value of 50  $\Omega$ . The sample CPW was defined in a thick Cu/Ta underlayer and the sample elements were of the form  $\text{Ni}_{81}\text{Fe}_{19}(40)/\text{AlO}_x(1.5)$  + oxidation (thicknesses are in nanometres). A schematic of the sample CPW is shown in Fig. 7.1.1. Further details on the sample fabrication and the full stack composition can be found in chapter 3.

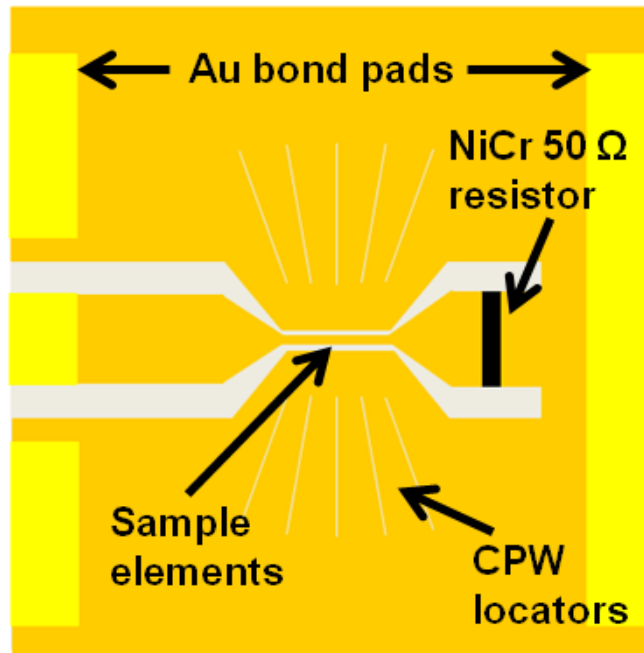


FIG. 7.1.1. A schematic diagram of the sample CPW used for TR-XPEEM measurements. The sample elements are deposited onto the central track of a CPW waveguide so they experience an in-plane excitation field. The CPW is terminated by a 50  $\Omega$  thin film resistor to prevent back reflections.

Prior to XPEEM studies, initial dynamic characterisation was performed with Time-Resolved Scanning Kerr Microscopy (TRSKM) on the sample devices described above to confirm the operation of the CPW devices. This work will now be detailed in the following section.

## 7.2 Initial characterisation with TRSKM

As with any stroboscopic measurement the pump and probe are required to be phase locked to one another for TR measurements to be possible. In the TRSKM setup the probe is a Ti: sapphire ultrafast pulsed laser system (Spectra Physics Tsunami). For the measurements presented in this chapter the pump used in TRSKM measurements was a pulsed magnetic field supplied by passing the output from a pulse generator (Picosecond Pulse Labs (PSPL) 3600) down the sample CPW so that the sample elements experienced an in-plane pulsed field. All timing signals were locked to a master oscillator (Atlantic Microwave) that produced a phase stable 80 MHz output. A schematic of the TRSKM is shown in Fig. 7.2.1.

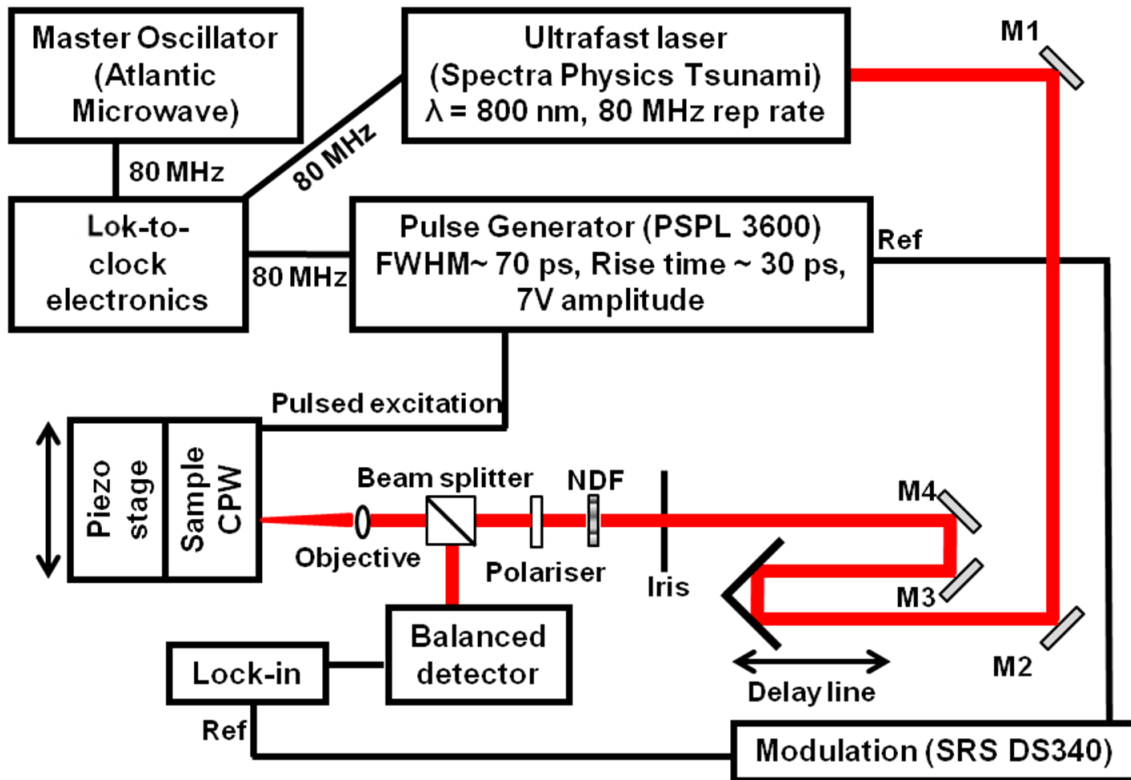


FIG. 7.2.1. A schematic of the TRSKM. A Ti: sapphire ultrafast laser system probes the magnetisation dynamics induced in micro and nano scale elements by an in-plane pulsed field. Time resolution is obtained by shifting the pump-probe delay by sending the probe pulse through an optical delay line.

The Tsunami was phase locked to the 80 MHz output of the master oscillator via the lok-to-clock electronics shown in Fig. 7.2.1. The lok-to-clock outputs a second 80 MHz signal which is phase locked to the 80 MHz signal from the master oscillator. This then allows the PSPL pulse generator to be phase locked to the ultrafast laser system. The relative delay between the pump and probe was changed by sending the probe beam through an optical delay line that offered a total delay of 4 ns and sub picosecond step resolution. The linearly polarised probe beam was focused onto the chosen sample element with a x40 microscope objective which also served to recollimate the reflected beam. The sample waveguide was mounted on a piezoelectric stage allowing the sample elements to be rastered underneath the probe beam in sub micron steps. After recollimation the reflected beam was diverted into a balanced detector by a polarization preserving beam splitter. The balanced detector consists of a Glan-Thompson polarising beam splitter and a pair of photodiodes. The Glan-Thompson polarising beam splitter was used to split the beam incident upon it into two beams of orthogonal linear polarisation. Each beam is then detected by one of the photodiodes. Upon interaction with a magnetic material linearly polarised light becomes elliptically polarised due to

the Magneto Optical Kerr Effect (MOKE)<sup>83</sup>. This can be explained by picturing the spin-orbit interaction in the magnetic sample as a magnetic field which re-orientates the oscillating dipoles in the magnetic material so that the polarisation of the emitted light is rotated with respect to that of the incident light<sup>84</sup>. By splitting the reflected beam into two beams of orthogonal linear polarisation and then measuring their respective intensities with separate photodiodes it is possible to measure the Kerr rotation. Alternatively the ellipticity of the reflected beam can be measured by inserting a quarter wave plate in front of the detector. The Kerr rotation and the ellipticity are defined below in Fig. 7.2.2. Sum and difference amplifiers allow the Kerr rotation (difference) and DC reflectivity (sum) to be measured. The difference signal from the balanced detector is then passed to a lock-in amplifier. The output of the pulse generator was modulated at an audio frequency of  $\sim 3$  kHz to facilitate lock-in detection. For all the TRSKM measurements presented in this chapter the polar Kerr effect was measured (Fig. 7.2.2).

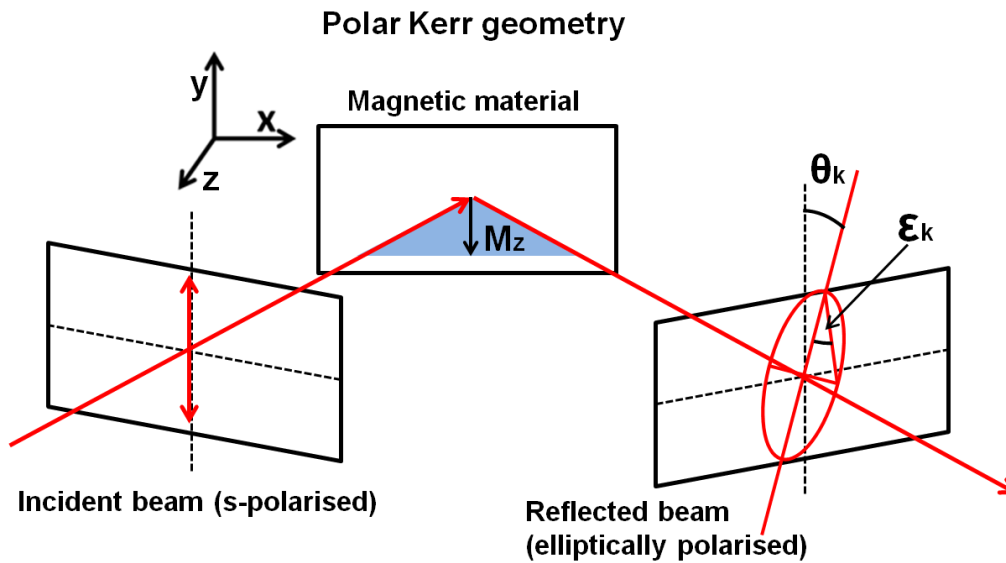


FIG. 7.2.2. A schematic diagram defining the polar Kerr geometry and the Kerr rotation ( $\theta_K$ ) and ellipticity ( $\epsilon_K$ ) that arise from the reflection of linearly polarised light from a magnetic material. The case of s-polarised light is shown.

Whilst it is not usually possible to image the ground state magnetisation with TRSKM because the signal-to-noise ratio is significantly worse without the phase sensitive detection, it is possible to acquire a spatial map of the dynamic response of a sample element with lateral dimensions of just a few microns. A typical example from a  $5 \mu\text{m}$  square element is shown in Fig. 7.2.3.

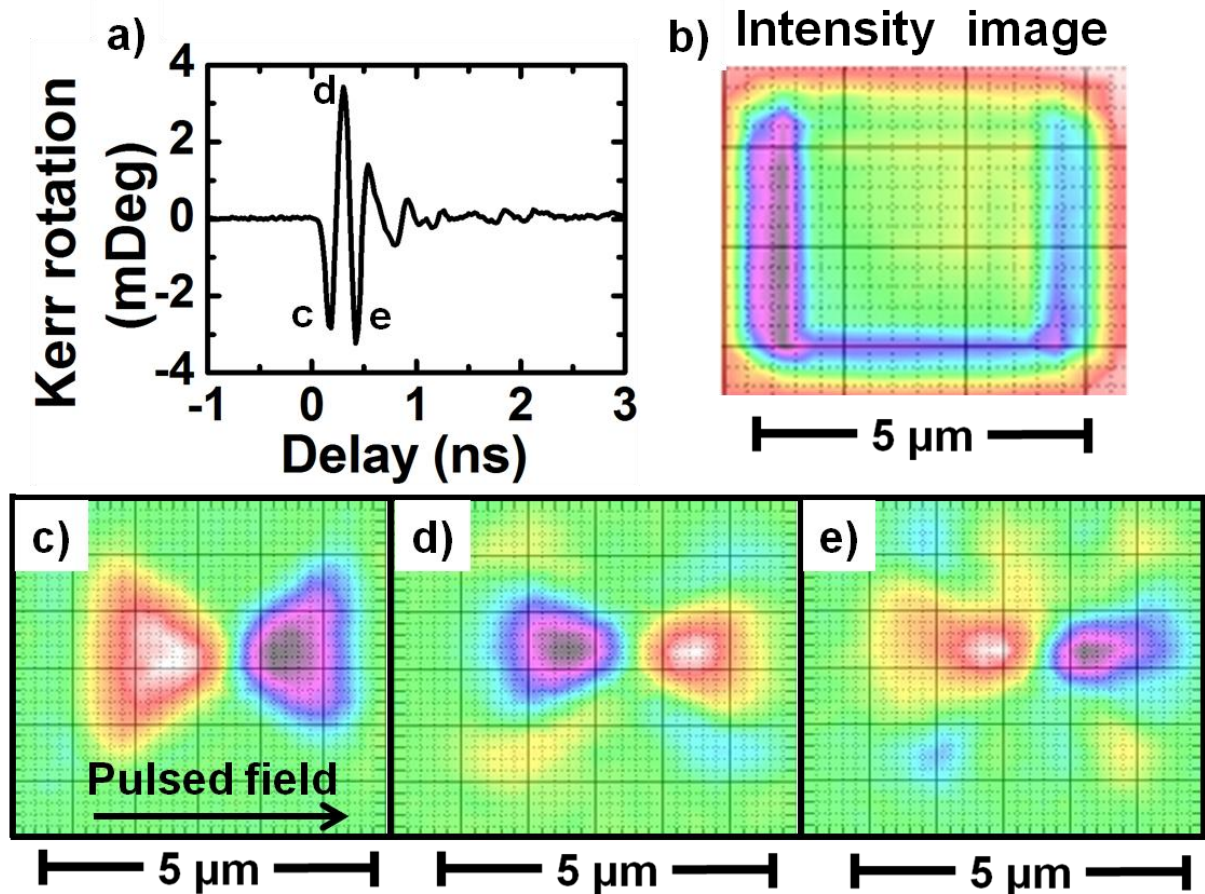


FIG. 7.2.3 (a) The response of a 5  $\mu\text{m}$   $\text{Ni}_{81}\text{Fe}_{19}$  square element to an in-plane pulsed field. Zero time delay is defined as the time at which pulsed field reaches 10% of its maximum value. (b) An intensity image of the 5  $\mu\text{m}$  square. (c) By setting the pump-probe delay to the first negative anti node in the pulsed field response it possible to obtain a spatial map of the dynamic polar Kerr signal. (d) & (e) The dynamic contrast is seen to reverse at successive anti nodes. An example pulse profile and details on how it was measured is given in Fig. 7.4.1.

First the 5  $\mu\text{m}$   $\text{Ni}_{81}\text{Fe}_{19}$  square element is excited by an in-plane pulsed field and the temporal evolution of the dynamic response recorded by scanning the pump-probe delay. The dynamics are seen to relax after  $\sim 1$  ns. It is then possible to obtain a spatial map of the dynamic polar Kerr signal by fixing the pump-probe delay at a value of interest, determined from Fig. 7.2.3. (a), then raster scanning the probe spot over the sample element. Typical examples are shown in Fig. 7.2.3. (b)(c) & (d). Only the magnetisation in the two magnetic domains orientated orthogonal to the pulsed field experience a torque and so it is only in these domains that a dynamic response is observed. The dynamic contrast is seen to reverse when the pump-probe delay is shifted between two anti nodes in Fig. 7.2.3. (a) of opposite sign. This is consistent with the

magnetisation precessing about the effective internal field with the reversal of the contrast representing a  $\pi$  phase shift.

The dynamic Kerr images show clear evidence of precession in magnetic domains with magnetisation orthogonal to the pulsed field. As with any measurement technique there are some inherent limitations of TRSKM. For example, as mentioned above, it is not possible to image the ground state. This can be a problem as the initial magnetisation configuration has a strong influence on the subsequently excited dynamic behaviour of the magnetic system<sup>47</sup>. Such measurements are however readily obtained with an XPEEM microscope, which can be used to obtain high quality images with magnetic contrast<sup>85</sup>. This is one way in which XPEEM can complement TRSKM studies.

### **7.3 Examples of static XPEEM imaging**

As mentioned above XPEEM utilises the XMCD effect and can be used to acquire images with magnetic contrast. When transition metal ferromagnets are irradiated with soft x-rays of sufficient energy a photoelectron is excited from a 2p core state to the Fermi level. There are then two decay channels by which the excited photoelectron may return to its ground state: via the emission of a photon (fluorescence); or by the emission of an electron via an Auger process. It is this second decay channel, or yield, that is detected in XPEEM measurements. The Auger electron strongly scatters inside the ferromagnet giving rise to a cascade of secondary electrons being emitted from the sample surface. As the escape length of the electrons is only a few nanometres XPEEM is a predominately surface sensitive technique<sup>86,87</sup>. The probing x-ray spot can be raster scanned across the sample element and the XPEEM microscope measures the intensity of emitted photoelectrons over the sample surface. In the XMCD effect the photoelectron yield from a particular point on the sample surface depends upon the scalar product of the x-ray wave vector and the local magnetisation. By taking the difference of two images taken with opposite x-ray helicity it is then possible to obtain an image with magnetic contrast. Typical examples are shown in Fig. 7.3.1.

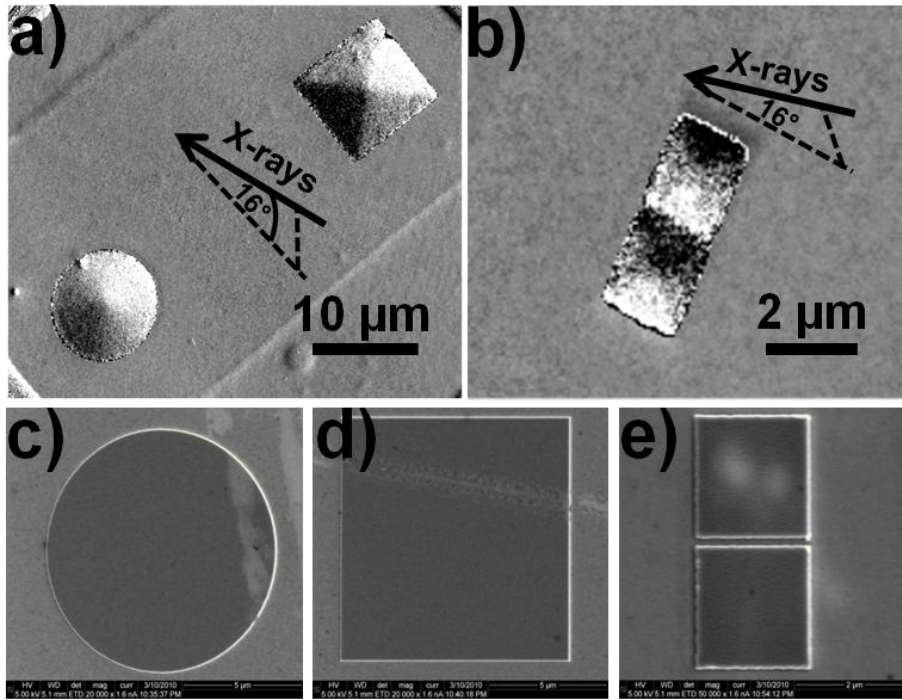


FIG. 7.3.1. (a) XPEEM images of flux closure states within 10  $\mu\text{m}$  circle and square elements. (b) Landau states with the same sense of circulation are shown for a pair of 2  $\mu\text{m}$  square elements separated by a 100 nm gap that has not been resolved. SEM images of (c) a 10  $\mu\text{m}$  circle (d) a 10  $\mu\text{m}$  square and (e) a pair of 2  $\mu\text{m}$  squares separated by 100 nm.

The grey-scale in Fig. 7.3.1. (a) & (b) indicates the direction of the local magnetisation. White corresponds to the magnetisation lying parallel to the x-ray wave vector for positive helicity and black corresponds to the case of anti parallel alignment. Looking at the 10  $\mu\text{m}$  square element in Fig. 7.3.1. (a) it also seen that there are two opposite domains each with an intermediate grey contrast. This corresponds to the case where the x-ray wave vector and local magnetisation are orthogonal and so the contrast in the two domains is the same. The two parallel lines in Fig. 7.3.1. (a) are the edges of the central track of the CPW. In all XPEEM images shown in this chapter the x-rays were at 16° grazing angle and so the grey-scale is dominated by the in-plane component of the magnetisation. The out-of-plane vortex core polarisation is not detected in this measurement geometry. It should also be noted that all XPEEM imaging presented in this chapter was done in the absence of an applied field. This is because the presence of an applied field would alter the trajectory of the emitted photoelectrons and in doing so distort the acquired image. This is one limitation of the XPEEM technique. It is noted that images with magnetic contrast can be acquired in an applied field with techniques that measure in a transmission geometry such as Transmission X-ray Microscopy (TXM)<sup>88,89</sup>.

With the principle of obtaining an XPEEM image with magnetic contrast described and the suitability of the samples demonstrated, the progress made towards establishing TR-XPEEM on beamline I06 will now be discussed.

## 7.4 Demonstration of a working TR-XPEEM setup

The principles of making TR-XPEEM measurements are largely the same as those discussed above for TRSKM. It is a stroboscopic measurement technique which means that there is a strict requirement for a fixed phase relationship between the pump and probe. In TR-XPEEM the probe is the pulsed x-ray beam and the pump is an in-plane pulsed magnetic field. The pulsed magnetic field is generated by connecting an Avalanche Photodiode (APD) to the sample CPW and gating it with an ultrafast pulsed laser system as there is currently no high frequency feedthrough on the PEEM microscope on beamline I06. An example pulse profile obtained from an APD (Silicon Sensor AD100-8TO52S1) is shown below in Fig. 7.4.1. A PIN diode was also used (Hamamatsu S9055) The pulse profile was measured by connecting an oscilloscope (Agilent 86100C (50 GHz) across the photodiode, without a current limiting resistor.

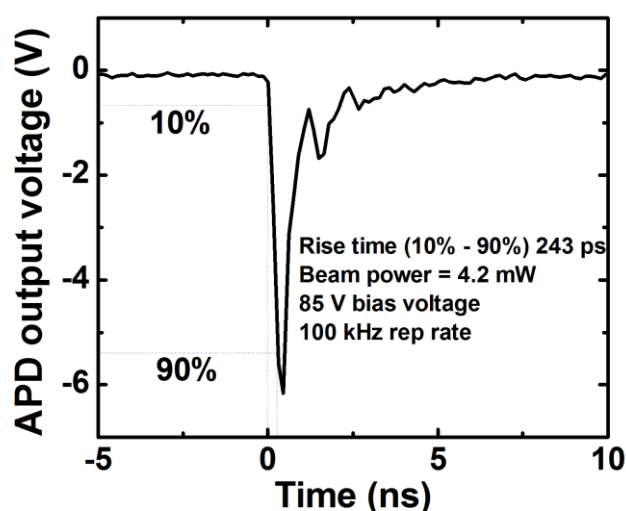


FIG. 7.4.1 The pulse profile acquired from an APD as measured by a 50 GHz oscilloscope. Zero time delay is defined as the point at which the pulse height reaches 10% of its maximum value.

The x-ray pulses and the ultrafast laser are both phase locked to the synchrotron master oscillator and so have a fixed phase relationship, allowing the pump-probe delay to be adjusted. Further details of the experimental setup can be found in chapter 3.

To perform TR measurements with a pulsed field excitation it is necessary to find zero time delay. Note that there is no zero time delay in the XFMR studies discussed in chapters 3 – 6 as these experiments were all performed with a Continuous Wave (CW) excitation. Showing experimental evidence that zero time delay has been found is therefore vital for the demonstration of a working TR-XPEEM setup. Intensity images taken at zero, and negative time delays are shown below in Fig. 7.4.2.

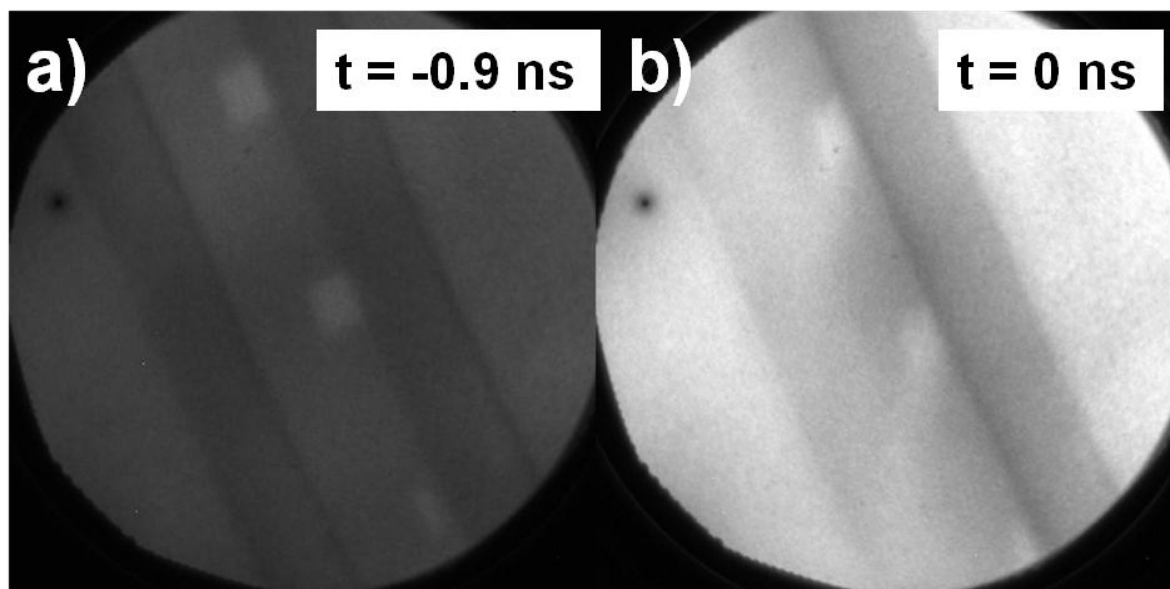


FIG. 7.4.2. (a) A intensity image taken with the PEEM of several 2  $\mu\text{m}$  elements before the arrival of the pulsed magnetic field (negative time delay). (b) When the pulsed field and the x-ray pulses arrive at the same time the intensity contrast from the sample elements is seen to washout in the same direction for each sample due to the deflection of photoelectrons caused by the presence of the pulsed field.

The images shown in Fig. 7.4.2. are intensity images, meaning that they were taken with just one x-ray helicity and therefore do not show magnetic contrast. Before the arrival of the pulsed field (negative delay - Fig. 7. (a)) the sample elements are clearly seen and the spatial extent of the sample grey-scale is the same shape as the sample. The dark black parallel lines are the trenches that separate the central track of the CPW from its ground planes. In Fig. 7.4.2. (b) the rapidly changing potential on the central track of the waveguide and the magnetic field generated by the flow of current in the waveguide both lead to a change in contrast within the image and a washing out of the sample element shape. This is a clear experimental demonstration of the location of zero time delay, meaning that it was possible to adjust the pump-probe delay. This is the key ingredient for any stroboscopic measurement technique.

The next step is to then acquire a series of images with magnetic contrast at different pump-probe delays. The first TR image series acquired with TR-XPEEM on beamline I06 is shown below in Fig. 7.4.3.

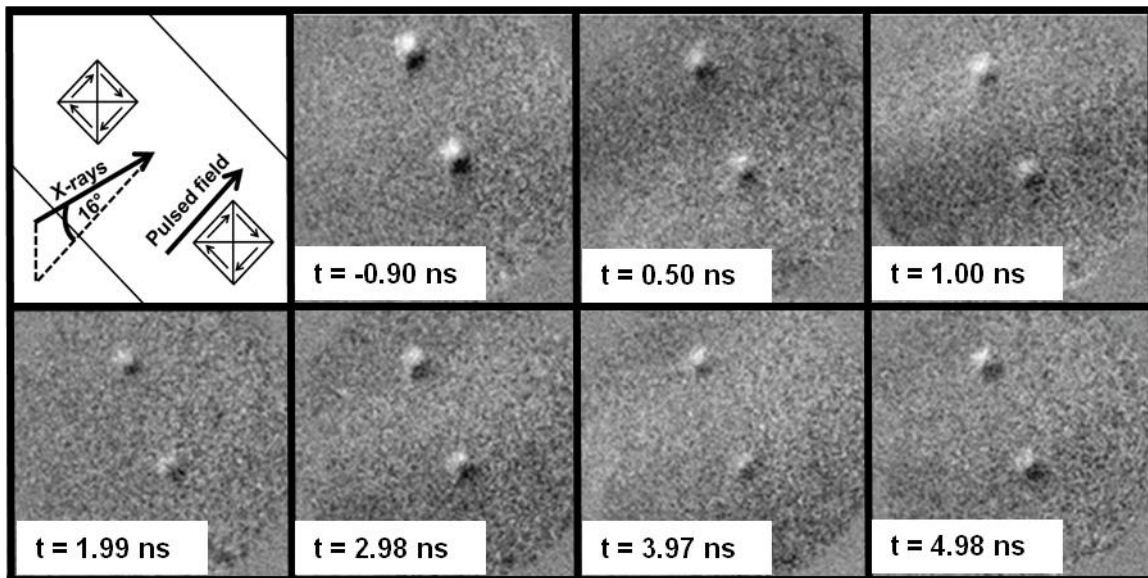


FIG. 7.4.3. A TR image series of a pair of well separated 2  $\mu\text{m}$  square elements subject to an in-plane pulsed field excitation. Magnetic contrast is seen in all images but the resolution of the TR-XPEEM setup is not yet sufficient for precession or vortex gyration to be clearly seen throughout the image series. (Inset) The direction of the pulsed field and x-ray wave vector are shown relative to the sample elements.

The time span of the image series extends from negative time delay to approximately 5 ns. The time span was chosen so as to look for vortex gyration in the 2  $\mu\text{m}$  square elements. The frequency of the gyrotropic mode in samples of the same aspect ratio was found to be of the order of several 100 MHz<sup>90</sup> and so 5 ns of delay should be sufficient to see vortex core motion. It is however clear from the TR image series in Fig. 7.4.3. that the spatial resolution is insufficient to reveal vortex gyration or precession within domains. The amount of beamtime available was insufficient to optimise the spatial resolution further.

## 7.5 Conclusion

The purpose of this chapter was to describe the progress made towards establishing TR-XPEEM at the Diamond Light Source. Permalloy micro and nano scale elements were deposited on integrated CPW devices by collaborators at HGST and the operation of the devices was confirmed with TRSKM. Static XPEEM images were shown to illustrate that the choice of samples allows high quality images with magnetic contrast to be obtained. The successful operation of TR-XPEEM was confirmed by observing a washing out of the intensity images at zero time delay. A TR image series of a pair of well separated 2  $\mu\text{m}$  squares was then taken, however more work is needed to improve the resolution of the TR-XPEEM now that it has been shown to work at the Diamond Light Source.

## **Chapter 8: Progress towards establishing phase-resolved XFMR in luminescence**

It has been known for some time that materials such as sapphire and MgO exhibit luminescence in the visible range when illuminated with soft x-rays<sup>91,92</sup>. In addition to the phase-resolved XFMR setup that measured the fluorescence yield detailed in chapter 4, work has been carried out to measure in luminescence. This chapter details the progress made towards building a working XFMR luminescence setup on beamline 4.0.2 at the ALS, which will ultimately enable transmission style measurements to be made on samples that are opaque in the soft x-ray regime.

### **8.1 Sample details and experimental setup**

All luminescence measurements presented in this chapter were made on a sample stack of the form: Ta(5)/ [Cu(25)/Ta(3)]<sub>3</sub>/ Cu(25)/ Ta(5)/ Ru(10)/ Ta(3)/ Ru(2)/ Cu(6)/ Ni<sub>80</sub>Fe<sub>20</sub>(5)/ Ru(7) stack (thicknesses in nanometres). The stack was magnetron sputtered onto a 500  $\mu\text{m}$  thick insulating sapphire substrate. Elements with lateral dimensions of 190  $\mu\text{m}$  x 400  $\mu\text{m}$  were formed on the thick Cu underlayer by electron beam lithography and ion beam milling. The aspect ratio of the elements is sufficient to avoid any inhomogeneous dynamics due to edge effects which may complicate the interpretation of the acquired data. Photolithography was then used to pattern the exposed Cu into a Coplanar Waveguide (CPW) structure with 50  $\Omega$  characteristic impedance and 200  $\mu\text{m}$  central track width. A 5  $\mu\text{m}$  border was left around the edges of the sample elements to avoid any sizable out-of-plane excitation. All fabrication was carried out by collaborators at the Hitachi Global Storage Technologies (HGST) San Jose research centre.

To detect the luminescence from the sample substrate a photodiode is placed directly behind the sample chip and so the photodiode does not impose any restrictions on the angle of incidence (Chapter 3). The first test carried out in luminescence was to determine which angle of incidence to measure at. This was done empirically by measuring static X-ray Magnetic Circular Dichroism (XMCD) spectra at a range of angles of incidence. XMCD spectra were obtained by fixing the x-ray helicity and flipping an externally applied bias field along the x-ray beam direction.

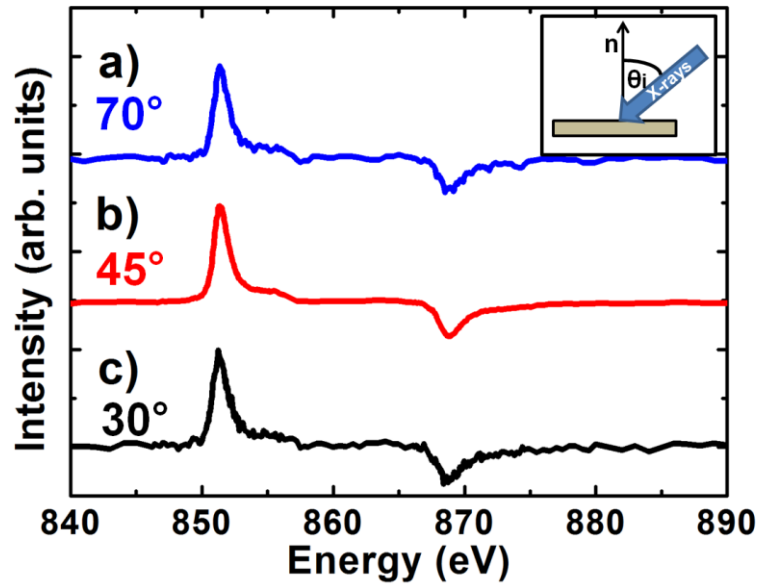


FIG. 8.1.1. Ni XMCD spectra in luminescence for a range of angles of incidence; (a) 70°, (b) 45° and (c) 30°. (Inset) A schematic defines the angle of incidence relative to the sample normal. The cleanest signal is obtained for a 45° angle of incidence. The spectra have been normalised to the same height as one another for ease of comparison.

Ni XMCD spectra were measured at a range of angles of incidence. Above in Fig. 8.1.1. are the Ni XMCD spectra obtained for angles of 70°, 45° and 30°. The spectrum taken at 45° is seen to be noticeably cleaner than the other spectra and so 45° was used for all subsequent dynamic measurements.

For phase-resolved measurements the geometry shown below in Fig. 8.1.2. was used.

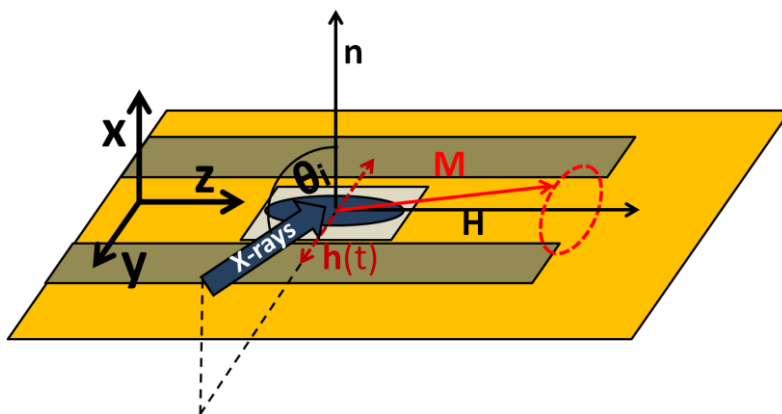


FIG. 8.1.2. The experimental geometry used to make luminescence measurements is the same as that detailed previously for fluorescence, but with the angle of incidence reduced to 45°. The magnetisation  $\mathbf{M}$  is forced into a state of steady precession about the applied bias field  $\mathbf{H}$  by an in-plane Radio Frequency (RF) magnetic field  $\mathbf{h}(t)$ . The x-rays measure a mixture of the in- and out-of-plane components of the magnetisation.

The lock-in detection scheme and the delivery of the RF excitation to the sample CPW used for dynamic luminescence measurements is the same as that used for fluorescence measurements. For brevity the reader is referred to chapters 3 and 4 for further details in these areas.

To test the functionality of the luminescence set up each of the 3 types of dynamic scan (field swept measurements, delay scans and dynamic XMCD spectra) that were previously measured in fluorescence were performed. The remainder of this chapter will show typical examples of each type of dynamic measurement and discuss what each measurement tells us about the operational capability of the luminescence method.

## 8.2 Field sweeps

The AC magnetic susceptibility ( $\chi_{ij}$ ) relates the dynamic magnetisation to the RF magnetic field in the presence of a bias magnetic field<sup>48</sup>.  $\chi_{ij}$  is a complex number so with appropriate choice of geometry and pump-probe delay it is possible to measure the *Re* and *Im* components of a particular component  $\chi_{ij}$ . The values of the indices (i,j) are determined with reference to the coordinate system shown in Fig. 8.1.2. The excitation is applied in the y-direction and so  $j = y$ . Due to the 45° angle of incidence a mixture of the magnetisation components  $M_y$  and  $M_x$  will be detected. It is noted that due to the strong out-of-plane demagnetising field the trajectory of the precessing magnetisation is elliptical, with the major axis in the plane of the sample. For a given RF power the ellipticity is also frequency dependent. For all measurements presented in this chapter a 4 GHz excitation was used. The ratio of the major and minor axes was calculated to be approximately 7:1. The measured component of  $\chi_{ij}$  is then written as  $\chi_{(yx)y}$  to indicate the mixing of  $M_y$  and  $M_x$  in the measured signal. Typical examples of field sweeps are shown in Fig. 8.2.1.

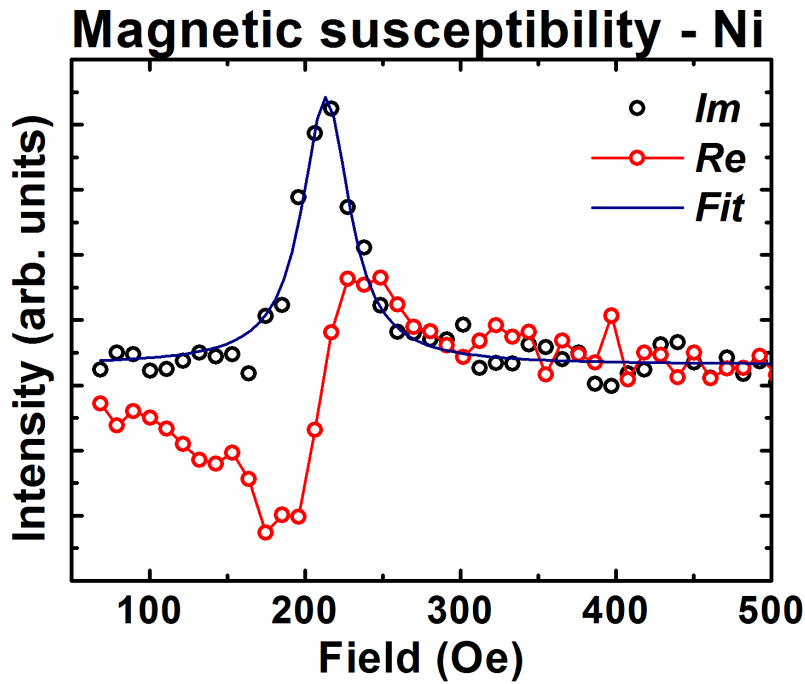


FIG. 8.2.1. The *Re* and *Im* components of  $\chi_{(yx)y}$  measured for Ni in a  $\text{Ni}_{80}\text{Fe}_{20}(5)$  thin film sample by XFMR in luminescence yield. Both curves were taken by sweeping the bias field (high to low) at a fixed pump-probe delay.

The characteristic lineshapes of the *Re* and *Im* components are clearly seen in the data in Fig. 8.2.1. with the steepest part of the *Re* component occurring at the same bias field value as the turning point in the *Im* component. Interestingly, the lineshapes shown in Fig. 8.2.1. agree very well with those obtained in fluorescence yield at an angle of incidence of  $70^\circ$  (Chapter 4). This indicates that the mixture of  $\chi_{yy}$  and  $\chi_{xy}$  is again dominated by the in-plane component,  $\chi_{yy}$  and so in the present geometry:  $\chi_{(yx)y} \sim \chi_{yy}$ .

### 8.3 Dynamic XMCD spectra

With the resonance field well characterised it is then possible to measure dynamic XMCD spectra at different points within the cycle of precession. This is done by setting the bias field to the resonant value, fixing the pump probe delay, and then scanning the x-ray beam energy through the same range that one would use to obtain an XMCD spectrum in the static case. The use of lock-in detection means that it is only necessary to measure with a single x-ray helicity<sup>25</sup>. The reader is referred to Chapters 3 and 4 for further details. Typical examples are shown below. For comparison they are shown next to dynamic XMCD spectra in fluorescence that were also obtained on beamline 4.0.2. at the ALS. The dynamic spectra shown in chapter 4 that have a better signal-to-noise

ratio, were obtained at Diamond, not at the ALS. More averaging was typically needed to obtain comparable signal-to-noise ratio at the ALS. While the amount of time for which one is required to average varies greatly with the choice of sample and the type of measurement being attempted, the time required was found to be roughly 1.5 – 2 times as long at the ALS as compared to Diamond. This value is intended as a guide for future users and should not be rigidly adhered to.

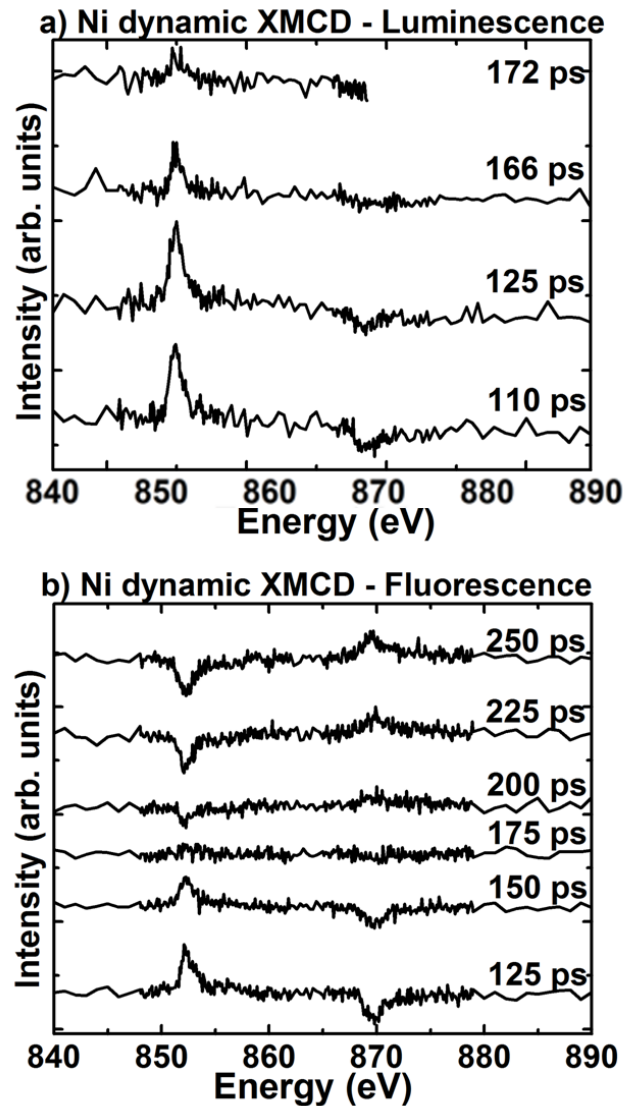


FIG. 8.3.1. (a) Dynamic XMCD spectra for Ni obtained in luminescence at resonance (210 Oe) from a  $\text{Ni}_{80}\text{Fe}_{20}(5)$  thin film sample at the ALS (b) Dynamic XMCD spectra obtained for Ni in a  $\text{Co}_{50}\text{Fe}_{50}(0.7)/\text{Ni}_{90}\text{Fe}_{10}(5)$  thin film sample at resonance (200 Oe) in fluorescence yield at the ALS are shown for comparison. The same amount of averaging was performed for both (a) and (b).

The data in Fig. 8.3.1. follows the expected trend. The lineshape of the XMCD spectra will not change as a function of pump probe delay if the spin and orbital moments

process in phase with one another, but the amplitude will be scaled by the projection of the phase dependent component of the magnetisation onto the x-ray wave vector. In addition to the discussion above about the difference in the light sources at Diamond and the ALS it is also worth noting that there is an inherent difference in the signal sizes measured in luminescence and fluorescence. It was found that the fluorescence signal is in the region of 2 – 3 times larger than that of the luminescence during a like for like measurement, in terms of photodiode current. By this it is meant that the same measurement was performed on the same sample at the same light source. The most reliable comparison was obtained by measuring a Ni L<sub>3</sub> hysteresis loop from permalloy and comparing the values of the photodiode current. Erroneous results can be obtained if the x-ray spot is not fully landed on the sample element. To help avoid this the hysteresis loops were often taken on the much larger ground plane markers (Chapter 3) Care should also be taken to make sure that the beamline is well aligned so that changes in the amount of x-ray flux striking the sample over time do not result in erroneous results.

#### **8.4 Delay scans**

In a delay scan the pump-probe delay is scanned while the applied bias field and the energy of the x-ray beam are kept constant. Changing the pump-probe delay changes the projection of the x-ray wave vector onto the phase dependent component of the magnetisation. The XMCD signal scales as the scalar product of the two aforementioned vectors and so a delay scan will result in a sinusoidal variation of the XMCD signal with period constrained to be the same as that of the RF excitation. Typical examples are shown in Fig. 8.4.1.

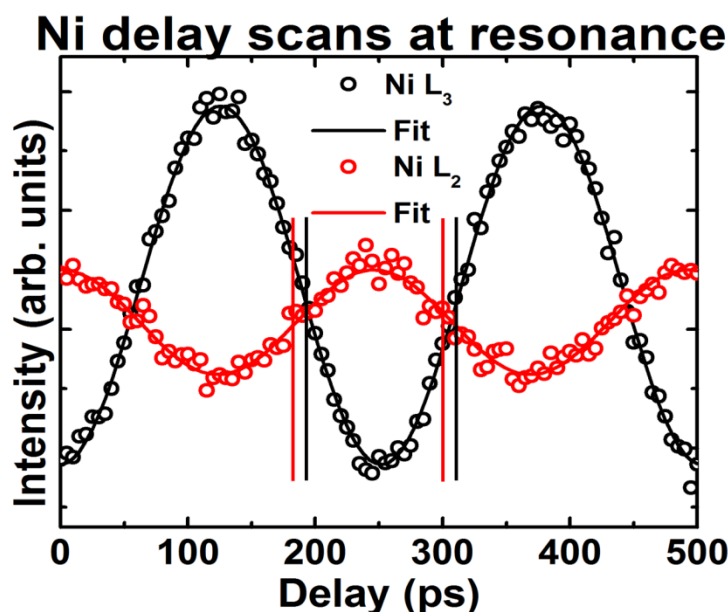


FIG. 8.4.1. Delay scans taken at both the Ni  $L_3$  and  $L_2$  edges from a  $\text{Ni}_{80}\text{Fe}_{20}(5)$  thin film sample by XFMR in luminescence yield by sweeping the pump probe delay at the resonance field. Note the surprising departure from a  $\pi$  phase shift between the two curves.

There are several points to note about the delay scan from the Ni  $L_3$  and  $L_2$  edges shown in Fig. 8.4.1. Firstly the dichroism at the Ni  $L_2$  edge is smaller than that at the  $L_3$  edge<sup>50</sup>. It is therefore not surprising that the amplitude of the  $L_2$  delay scan is smaller than that obtained at the  $L_3$  edge. Secondly the dichroism is of opposite sign at the two edges. One would then expect to see a  $\pi$  phase shift between the two curves in Fig. 8.4.1. – however this is not what is seen. The departure from a  $\pi$  phase shift between the two curves in Fig. 8.4.1 indicates the presence of an unexpected background. The work done to characterise the said background will now be detailed.

As the two delay scans in Fig. 8.4.1. differ only in being measured at different x-ray beam energies, it is interesting to repeat such measurements with the x-ray beam energy set to a value where there is no dichroism.

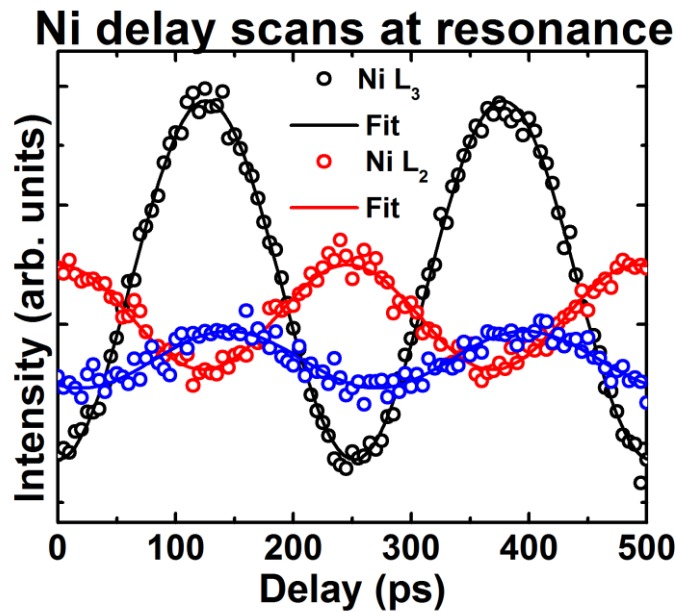


FIG. 8.4.2. Delay scans taken at both the Ni  $L_3$  and  $L_2$  edges from a  $\text{Ni}_{80}\text{Fe}_{20}(5)$  thin film sample in luminescence yield (shown previously in Fig. 8.4.1.) are overlaid with a scan taken on the Ni pre-edge (840 eV) where no dichroism is present.

Interestingly if a delay scan is taken on the Ni pre-edge (840 eV) a clear oscillatory signal is seen as a function of pump-probe delay. The period of the signal is the same as that of the RF excitation and it has a different phase to both the  $L_3$  and  $L_2$  edge delay scans. This indicates that a signal, not of dichroic origin, is being detected at the lock-in reference frequency – something which was checked for but not observed in the fluorescence setup. The presence of such a background will then alter the pump-probe delays at which the node and anti node of a delay scan taken on an absorption edge occur. Hence there is a departure from a  $\pi$  phase shift between the  $L_3$  and  $L_2$  delay scans in Fig. 8.4.1. It is then insightful to ask whether the phase and amplitude of this oscillatory background are dependent on the value of the applied bias field. To investigate this further, delay scans were measured on the Ni pre-edge (840 eV), post edge (890 eV), and  $L_3$  and  $L_2$  edges for several values of the bias field, on and off resonance. Each delay scan was fitted with a sinusoidal function, with period constrained to the same as that of the 4 GHz RF excitation. The extracted phases and amplitudes are shown in Fig. 8.4.3.

| Field (Oe) | $X_c$ (ps)      |                 |                |                |
|------------|-----------------|-----------------|----------------|----------------|
|            | L3              | L2              | Pre-edge       | Post-edge      |
| + 225 Oe   | 47.1 $\pm$ 0.7  | 173.6 $\pm$ 3.8 | 54 $\pm$ 4     | 44.8 $\pm$ 3.8 |
| + 200 Oe   | 25.5 $\pm$ 0.5  | 139 $\pm$ 1.4   | 48 $\pm$ 3.5   | 53 $\pm$ 5.7   |
| - 189Oe    | 15.4 $\pm$ 1    | 122.8 $\pm$ 2.8 | 50 $\pm$ 7     | 49 $\pm$ 7     |
| +180 Oe    | 119.1 $\pm$ 0.7 | 99.8 $\pm$ 1.1  | 52.2 $\pm$ 3.8 | 50.3 $\pm$ 4.2 |

| Field (Oe) | Amplitude (counts) |               |              |              |
|------------|--------------------|---------------|--------------|--------------|
|            | L3                 | L2            | Pre-edge     | Post-edge    |
| + 225 Oe   | 36042 $\pm$ 3      | 4384 $\pm$ 3  | 7650 $\pm$ 4 | 5873 $\pm$ 3 |
| + 200 Oe   | 52883 $\pm$ 3      | 13527 $\pm$ 3 | 8118 $\pm$ 4 | 5888 $\pm$ 4 |
| - 189Oe    | 53607 $\pm$ 7      | 14805 $\pm$ 8 | 9064 $\pm$ 9 | 5603 $\pm$ 5 |
| + 180 Oe   | 44467 $\pm$ 3      | 17958 $\pm$ 3 | 7483 $\pm$ 4 | 5600 $\pm$ 3 |

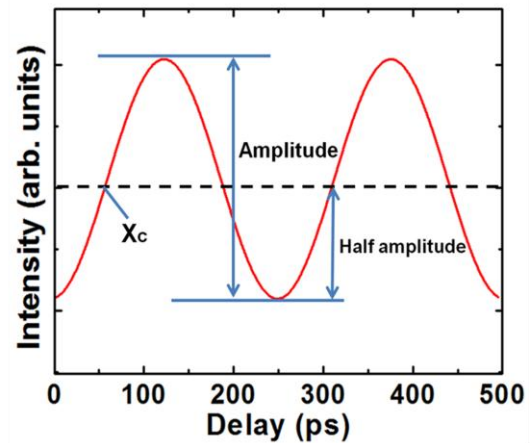


FIG.8.4.3. Delay scans were taken at different applied bias fields and x-ray beam energies to characterise the oscillatory background present in the luminescence setup. The phase and amplitude from each delay scan were extracted with sinusoidal fitting and tabulated. The amplitude and the crossing point,  $X_c$ , are also defined.

There are several features of the data shown in the table in Fig. 8.4.3. to be discussed. For the  $L_3$  and  $L_2$  delay scans a strong variation is seen in both the amplitude and phase with bias field. This is expected from the lineshapes of the AC magnetic susceptibility curves shown in Fig. 8.2.1. The phase of the pre- and post-edge delay scans may show weak bias field dependence. Due to the size of the extracted error bars, better statistics are needed to decide whether the apparent small offset in phase between the pre- and post-edge delay scans is significant. While the amplitude of the pre- and post-edge delay scans shows a similarly weak dependence on the applied field, there is a clear difference of approximately 20 – 30% between the pre- and post-edges. This suggests that it may be necessary to investigate the oscillatory background for a greater number of x-ray beam energies, as well as applied bias field values.

Although the background described above could not be suppressed during this PhD project, it is useful to discuss its possible origin. The use of lock-in detection means that the luminescence setup can only detect signals that are modulated at the lock-in reference frequency. The only signal that is intentionally modulated is the RF excitation which is passed to the sample CPW, which suggests RF pickup. This could occur at two places, either along the cabling assembly to the photodiode, or at the photodiode itself. If present this could generate an alternating bias voltage across the photodiode that would modulate the gain of the photodiode at the lock-in reference frequency. The presence of such an alternating voltage was explored by disconnecting the photodiode

cabling outside the vacuum system from the lock-in amplifier and connecting it to an oscilloscope (Agilent 86100C (20 GHz)) instead. With the RF set to 4 GHz and full power (+25 dBm / 0.5 W at source) a 120 mVpp 4 GHz signal was observed across the photodiode. The signal disappeared when the RF was turned off and fell to 80 mVpp when the RF was attenuated by 3 dB (50%). When the differences in cable lengths between the RF path and photodiode were accounted for, a  $\pi$  phase difference was found between the RF excitation and the oscillatory signal across the photodiode. In addition it is worth noting that the rise time of the photodiode is only 1  $\mu$ s when unbiased, suggesting that the 4 GHz RF signal is being picked up by the vacuum SMA cabling rather than the photodiode. Alterations to the RF shielding were made by replacing large sections of exposed pcb waveguide on which the photodiode was mounted with vacuum compatible SMA cable, but the background remained. During one beamtime a reverse bias was applied to the photodiode so that RF pickup would not modulate its gain. Initially a bench top power supply (Isotech IPS-3303) was used to apply the reverse bias but could not provide the required voltage stability and so a battery was used instead. With the battery connected it was then impossible to measure a dynamic signal, suggesting that the sensitivity of the photodiode had been reduced below the noise floor of the experiment. Further investigation in which different bias voltages are applied to the photodiode may prove more insightful. Also, if RF pickup were the cause of the oscillatory background then one would expect the phase and amplitude extracted from the pre- and post-edge delay scans, shown in Fig. 8.4.3., to be independent of magnetic field.

The other idea advanced to try and explain the oscillatory background was the presence of stray photoelectrons striking the active area of the photodiode. The reader is referred to chapter 3 (Fig. 3.2.1) for a photograph of the luminescence sample holder. The number of photoelectrons emitted from the surface would be dependent on the x-ray beam energy. Also, the trajectory of a photoelectron is field dependent and so one would expect some bias field dependence of the number of photoelectrons striking the photodiode. This could then yield a background dependent on both bias field and x-ray beam energy that is modulated at the lock-in reference frequency. As a first step toward testing this idea photodiodes with 150 nm Al films deposited on the active area (AXUV20AA1 – International Radiation Detectors) were used. The photodiodes are identical to those used for all the XFMR experiments detailed in this thesis, with the addition of a directly deposited Al foil. This approach was taken rather than using a

suspended Al foil, as is used in the fluorescence setup, as the integration of such a device into the luminescence stick required a redesign of the sample stick and frame for the Al foil at short notice. Some preliminary tests were carried out with the photodiodes using the fluorescence setup detailed earlier and results revealed that the Al foil caused a field dependent background to occur that was not present when a free standing Al film was suspended in front of, and not in contact with, the active area. The background was detected during a static measurement in which the x-ray beam energy was set to the Ni L<sub>3</sub> absorption edge and the applied bias field scanned. This background is attributed to the directly deposited Al foil not being electrically well isolated from the active region of the photodiode. As a result the photoelectrons cannot flow to ground (the chamber) as they do in the case when a free standing foil is used. In retrospect it is not clear that the use of an Al foil is useful in this case, since it may strongly attenuate the luminescence.

## 8.5 Conclusion

It was possible to obtain phase-resolved measurements in luminescence yield for the first time. The quality of the data was sufficient for the *Re* and *Im* components of the AC magnetic susceptibility and dynamic XMCD spectra to be clearly seen. The phase difference between delay scans taken on the Ni L<sub>3</sub> and L<sub>2</sub> edges from permalloy was found to depart from  $\pi$ , suggesting the presence of an unexpected background. A sinusoidal signal with the same frequency as the RF excitation was seen on both the Ni pre- and post-edges. The dependence of the background on applied bias field and beamline energy were characterised and the attempts made to remove the said background during this PhD project were detailed. It seems that the most likely cause of the background is RF pickup and that further insight may be gained by using a tuneable battery box to vary the reverse bias applied to the photodiode.

## Chapter 9: Conclusions and future work

### 9.1 Conclusions

The aim of this thesis was to develop and employ a range of FMR based techniques to learn more about the dynamics of a range of magnetic systems in the macrospin limit.

Chapter 2 outlined the underlying theoretical concepts required to understand the later chapters of this thesis.

Chapter 3 detailed the experimental development of a range of time/phase-resolved techniques used to perform FMR measurements: phase-resolved XFMR in both fluorescence yield and luminescence; low temperature TR-MOKE; and phase-resolved VNA-FMR. The progress made towards developing TR-XPEEM for acquiring images with magnetic contrast was also detailed. The experimental results from each technique were shown in later chapters.

Chapter 4 showed XFMR results already published in Journal of Applied Physics and presented at Magnetism and Magnetic Materials in 2010 and Current Research In Magnetism in 2011. The purpose of the chapter was to illustrate that phase-resolved XFMR in fluorescence yield is a viable method of making chemically resolved FMR measurements with a timing resolution of 1 – 2 ps on samples that are opaque in the soft x-ray regime. Phase-resolved VNA-FMR measurements were also shown to illustrate the quality of data that can be obtained from the setup detailed in chapter 3.

Chapter 5 brought together several experimental techniques to learn more about the dynamic and static properties of  $\text{Co}_{50}\text{Fe}_{50}$  (0.7 nm)/ $\text{Ni}_{90}\text{Fe}_{10}$  (5 nm)/Dy (1 nm) – a stack representative of the free layers in high density recording heads currently used in industry. TR-MOKE measurements showed an enhancement of the damping at room temperature in the presence of the Dy capping layer. Static XMCD characterisation revealed the presence of a net magnetic ordering of the Dy at room temperature, even though this in this temperature regime bulk Dy is known to be paramagnetic. Dy XMCD spectra taken as a function of temperature revealed that the magnetic ordering of the Dy cap increases with decreasing temperature. Low temperature TR-MOKE based FMR experiments then revealed that the damping increases with decreasing temperature in the presence of the Dy cap, whilst no such trend was observed for a

control sample where the Dy cap was not present. The efforts made to obtain a full explanation for the interesting behaviour observed in the FMR were detailed.

Chapter 6 presented XFMR measurements of spin pumping effects in industrially relevant spin valve stacks with lateral dimensions of several hundred microns. The purpose of the study was to probe the dynamics induced in the spin sink layer due to the absorption of a pure spin current. Using the chemical sensitivity of XFMR allowed the dynamic response of the spin pump and spin sink layers to be completely separated. Spin pumping induced dynamics were clearly observed in the spin sink layer when the spacer layer lay in the purely spin ballistic regime. A control sample, in which the spacer layer lay in the strongly spin diffusive regime, was also measured and no evidence of spin pumping induced dynamics were seen in the spin sink layer. A macrospin model based on the Landau-Lifshitz-Gilbert-Slonczewski equation was able to qualitatively reproduce all the main features of the experimental data. The use of sample stacks with lateral dimensions of several hundred microns is important as it removes complications due to edge effects associated with nanopillar STOs. Combined with the phase and chemical sensitivity of XFMR this provides a new way of characterising STT based devices and for experimentally determining the spin diffusion length in a whole host of potential spacer layers.

Chapter 7 detailed the progress made towards establishing TR-XPEEM at the Diamond Light Source. Sample suitability was determined with TR-MOKE measurements and the ground state imaged with XPEEM. The various timing constraints in TR-XPEEM have been detailed. The identification of zero time delay between the field pulsed pump and the x-ray probe was shown experimentally and the first TR image series was presented. With the principle of TR-XPEEM demonstrated, the setup can be optimised to yield images with higher spatial resolution.

Chapter 8 detailed the progress made, up to the time of writing, towards developing phase-resolved XFMR in luminescence. The dynamic measurements made with the fluorescence setup were repeated in luminescence and the dynamic response was clearly seen. A background was observed that complicated the interpretation of the acquired data. The current thinking on the origins of the background was presented.

## 9.2 Future work

The experimental work presented in chapter 4 demonstrates that phase-resolved XFMR in fluorescence yield is a tool well suited to performing chemically resolved FMR measurements with a timing resolution of just a few picoseconds. The use of fluorescence yield instead of transmission opens up this emerging technique to samples that are opaque in the soft x-ray regime and so removes the constraint of fabricating samples on fragile  $\text{Si}_3\text{N}_4$  membranes. This then enables a single sample chip to be designed that can be measured by a host of different FMR based techniques.

Chapter 5 showed how the addition of a rare earth capping layer to a read head free layer results in a strong damping enhancement. These results are very useful to industry where a major area of research is to reduce the time it takes to read and write data by reducing the time it takes to switch and stabilise the magnetisation. Enhanced damping is also required to suppress unwanted STT effects. It is next interesting to compare the results obtained with a 1 nm thick Dy capping layer with those obtained with other rare earth element capping layers and their alloys to find the optimal cap for a given read head free layer. The thickness dependence of the capping layer is also a potential area for investigation.

Chapter 6 showed a viable experimental method for measuring the spin diffusion length in a non magnetic material. The accurate determination and subsequent manipulation of spin current is important if spin based logic systems are to emerge as a viable medium for information transfer.

Chapter 7 showed that the foundations for a working TR-XPEEM setup have been laid at the Diamond Light Source. The smaller diffraction limited spot size possible with x-rays as compared to visible light provides the possibility for the spatial resolution of the TR-XPEEM setup to outstrip that of the more common TR MOKE technique. One area that this could then be useful for is characterisation of the inhomogeneous dynamics present in nanomagnets, the understanding of which is interesting both from a fundamental and a device stand point.

There are many systems that can be studied with the FMR techniques developed during this PhD project. At the time of writing the author has developed a working low temperature XFMR setup at the ALS and is working with collaborators from the group of Professor Qiu from UC Berkeley to study AFM/FM bilayers, the dynamic response

of which has received little study to date. Due to the exotic ways in which the FM and AFM spins can statically couple to one another<sup>93</sup>, the dynamic response may prove to be very rich indeed in information which can shed some light on the underlying physics present in such a system. FMR experiments are currently underway as a function of CoO thickness, ambient temperature, excitation frequency and cooling field history. Once these parameters have been thoroughly explored the use of the existing XFMR setup may offer the possibility of performing measurements of the dynamics induced in the CoO that occur as a result of the coupling to the FM layer. This would use X-ray Magnetic Linear Dichroism (XMLD) to resolve the dynamics of the CoO spins that occur as a result of the precession of the NiFe spins, to which they are coupled, being driven to a state of steady precession by a resonant microwave field. In addition it may be possible to utilise the emerging field of magnetic THz spectroscopy to measure the resonant response of AFM thin films. This would provide new and exciting information on the dynamic properties of AFM materials – something which at present has received very little attention and is poorly understood.

## List of commonly used acronyms

ALS: Advanced Light Source

APD: Avalanche Photodiode

BLS: Brillouin Light Scattering

CCD: Charge Coupled Device

CCP: Current Perpendicular to Plane

CPW: Coplanar Waveguide

DUT: Device Under Test

EA: Easy Axis

FM: Ferromagnet

FMR: Ferromagnetic Resonance

FWHM: Full Width Half Maximum

HGST: Hitachi Global Storage Technologies

IPA: Isopropanol

LGGS: Landau-Lifshitz-Gilbert-Slonczewski

LLG: Landau-Lifshitz-Gilbert

MCA: Magneto Crystalline Anisotropy

MCP: Micro Channel Plate

MOKE: Magneto Optical Kerr Effect

NM: Normal Metal

OFHC: Oxygen Free High Conductivity

PEEM: Photoemission Electron Microscopy

POMS: Portable Octupole Magnet System

RF: Radio Frequency

SOLT: Short Open Load Thru

SRD: Step Recovery Diode

STT: Spin Transfer Torque

TR-MOKE: Time Resolved Magneto Optical Kerr Effect

TRSKM; Time Resolved Scanning Kerr Microscopy

TR-XPEEM: Time Resolved X-ray Photoemission Electron Microscopy

VMM: Vector Magnetometer

VNA: Vector Network Analyser

VNA-FMR: Vector Network Analyser Ferromagnetic Resonance

VSM: Vibrating Sample Magnetometry

XAS: X-ray Absorption Spectroscopy

XFMR: X-ray Ferromagnetic Resonance

XMCD: X-ray Magnetic Circular Dichroism

XPEEM: X-ray Photoemission Electron Microscopy

## Appendix 1: Spin-orbit phase lag formula

This appendix shows the algebra used to produce the fit in chapter 4 that assumed a  $40^\circ$  phase shift between the spin and orbital moments

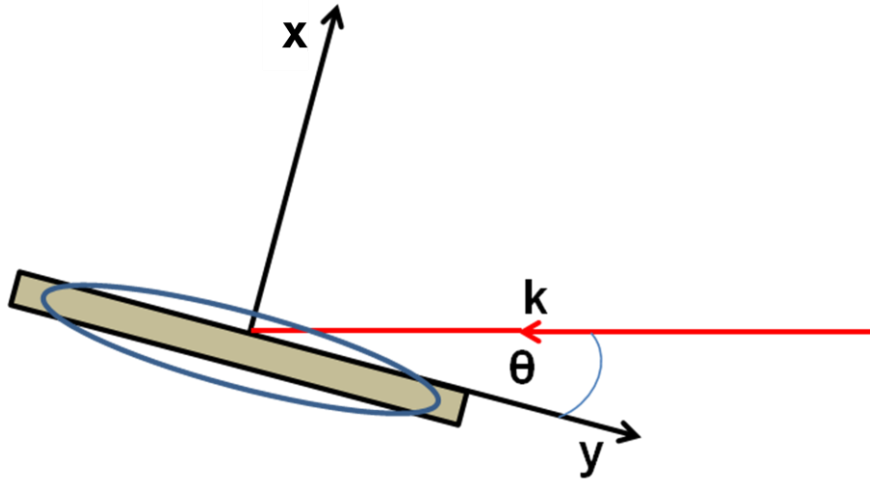


FIG. A2.1. The geometry used: the magnetisation lies in the sample plane and is saturated by an in-plane static field. An RF magnetic field is applied to the sample causing the magnetisation to enter a state of steady precession.

$$\mu_{Sy} = \mu_{So} \cos(\omega t)$$

$$\mu_{Sx} = \varepsilon \mu_{So} \sin(\omega t)$$

$$\mu_{Ly} = \mu_{Lo} \cos(\omega t - \phi)$$

$$\mu_{Lx} = \varepsilon \mu_{Lo} \sin(\omega t - \phi)$$

$$\mathbf{k} = k(-\cos(\theta), -\sin(\theta))$$

where the sine and cosine functions have been scaled by the static orbital and spin moments ( $\mu_{Lo}, \mu_{So}$ ), as these represent the values of the orbital and spin moments when the two lie in the sample plane. The ellipticity,  $\varepsilon$ , has been included in the equations for the out-of-plane components to account for the shortening of the out-of-plane components, relative to the in-plane components, due to the shape anisotropy.  $\phi$  is the angle by which the orbital moment lags the spin moment during precession.

We can now write an expression for the ratio of the orbital and spin moments, projected along the x-ray wave vector, over the entire precession cycle

$$R = \frac{\boldsymbol{\mu}_L \cdot \mathbf{k}}{\boldsymbol{\mu}_S \cdot \mathbf{k}} = \frac{\mu_{L0}}{\mu_{S0}} \frac{[-\cos(\theta) \cos(\omega t - \phi) - \varepsilon \sin(\theta) \sin(\omega t - \phi)]}{[-\cos(\theta) \cos(\omega t) - \varepsilon \sin(\theta) \sin(\omega t)]}$$

It is then necessary to consider the effect of a finite temporal pulse width. Let us define our x-ray pulse as

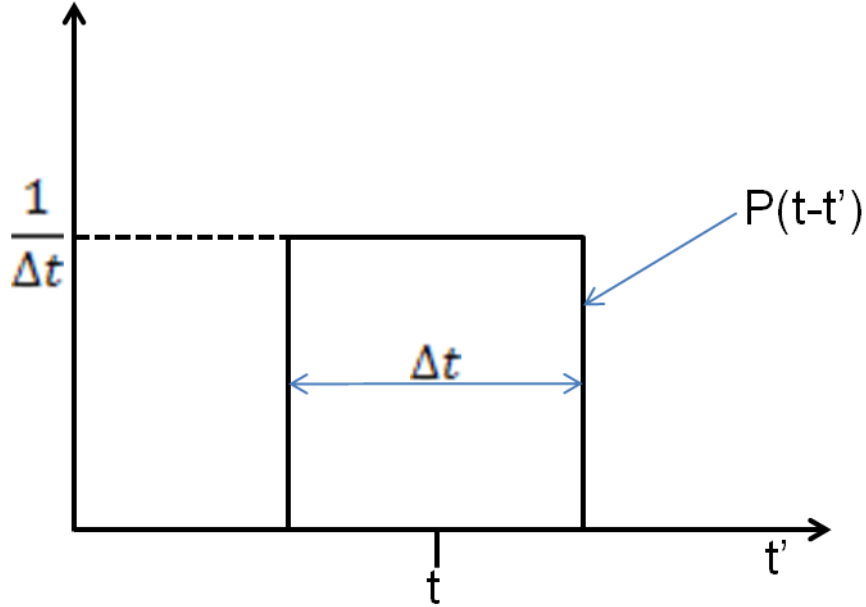


FIG. A2.2 The temporal profile of the x-ray pulses are modelled as a top-hat function with unit area, centred on ( $t' = t$ ).

By considering the convolution of the x-ray pulse with our expression for the ratio of the orbital and spin moments we can write the spin-orbit ratio that is to be compared to experimental data as

$$\bar{R} = \int P(t - t')R(t')dt'$$

To simplify the integration we define

$$\cos(A) = \frac{\cos(\theta)}{\sqrt{[\cos^2(\theta) + \varepsilon^2 \sin^2(\theta)]}}$$

$$\sin(A) = \frac{\varepsilon \sin(\theta)}{\sqrt{[\cos^2(\theta) + \varepsilon^2 \sin^2(\theta)]}}$$

and can then write

$$\frac{R}{\frac{\mu_{Lo}}{\mu_{So}}} = \frac{\cos(A) \cos(\omega t - \phi) + \sin(A) \sin(\omega t - \phi)}{\cos(A) \cos(\omega t) + \sin(A) \sin(\omega t)}$$

$$\frac{R}{\frac{\mu_{Lo}}{\mu_{So}}} = \frac{\cos(\omega t - \phi - A)}{\cos(\omega t - A)} = \frac{\cos(\omega t - A) \cos(\phi) + \sin(\omega t - A) \sin(\phi)}{\cos(\omega t - A)}$$

which simplifies to

$$\frac{R}{\frac{\mu_{Lo}}{\mu_{So}}} = \cos(\phi) + \tan(\omega t - A) \sin(\phi)$$

We carry out a change of variable

$$\bar{R} = \frac{\mu_{Lo}}{\mu_{So}} \int_{t-\frac{\Delta t}{2}}^{t+\frac{\Delta t}{2}} \left( \frac{1}{\Delta t} \right) [\cos(\phi) + \tan(\omega t' - A) \sin(\phi)] dt'$$

The integration can be carried out by making use of the stand integral

$$\int \tan(x) dx = \ln|\sec(x)| + c$$

$$x = \omega t' - A$$

$$\int \tan(\omega t' - A) \frac{dx}{dt'} dt' = -\ln|\cos(\omega t' - A)| + c$$

$$\int \tan(\omega t' - A) dt' = -\frac{1}{\omega} \ln|\cos(\omega t' - A)| + c$$

This then yields

$$\bar{R} = \frac{\mu_{Lo}}{\mu_{So}} \left[ \frac{1}{\Delta t} \left[ \cos(\phi) - \frac{\sin(\phi)}{\omega} \ln|\cos(\omega t' - A)| \right] \right] \Bigg|_{t-\frac{\Delta t}{2}}^{t+\frac{\Delta t}{2}}$$

$$\bar{R} = \frac{\mu_{Lo}}{\mu_{So}} \left\{ \cos(\phi) - \frac{\sin(\phi)}{\omega} \ln \left[ \frac{\cos(\omega(t + \frac{\Delta t}{2}) - A)}{\cos(\omega(t - \frac{\Delta t}{2}) - A)} \right] \right\}$$

The expression for  $\bar{R}$  was used to calculate the ratio of the spin and orbital moments over the entire precession cycle, shown in chapter 4.

## Appendix 2: Ferromagnetic Resonance in the limit of heavy damping

This appendix shows the derivation of equations for FMR curves in the limit of heavy damping. This was discussed in chapter 5 as a means to gain further insight into results from the FMR studies of Dy capped spin valve free layers as a function of temperature that were performed during this PhD project.

The same coordinate system that has been used throughout this thesis is used in the following derivation: z is in-plane and along the CPW symmetry axis, y is in-plane and transverse to the CPW symmetry axis, x is out of plane.

First define the AC magnetic susceptibility,  $\chi_{mn}$ , as

$$\begin{pmatrix} u_{x0} \\ u_{y0} \end{pmatrix} = \frac{1}{M} \chi \begin{pmatrix} h_{x0} \\ h_{y0} \end{pmatrix}$$

where  $u_{y0}$  and  $u_{x0}$  are the in-plane and out-of-plane dynamic components of the magnetisation, and  $h_{y0}$  and  $h_{x0}$  are the components of the RF driving field.  $M$  is the magnetisation.

After solving the linearised LLG equation, the right hand side can be written as

$$\frac{1}{\Delta} \begin{pmatrix} \left[ H \cos(\phi_H - \phi) + \frac{2K}{M} \cos 2\phi - \frac{i\omega\alpha}{|\gamma|} \right] & -\frac{i\omega}{|\gamma|} \\ \frac{i\omega}{|\gamma|} & \left[ H \cos(\phi_H - \phi) + 4\pi M - \frac{2K_{\perp}}{M} + \frac{2K}{M} \cos^2 \phi - \frac{i\omega\alpha}{|\gamma|} \right] \end{pmatrix} \begin{pmatrix} h_{x0} \\ h_{y0} \end{pmatrix}$$

where  $\phi_H$  and  $\phi$  are the angles between the easy axis and applied bias field and magnetisation respectively.  $K$  is an in-plane anisotropy constant and  $K_{\perp}$  is the perpendicular anisotropy constant,  $\alpha$  is the phenomenological Gilbert damping constant and  $\gamma$  is the gyromagnetic ratio. The  $\Delta$  term is given by

$$\Delta = \left[ H \cos(\phi_H - \phi) + \frac{2K}{M} \cos 2\phi - \frac{i\omega\alpha}{|\gamma|} \right] \left[ H \cos(\phi_H - \phi) + 4\pi M - \frac{2K_{\perp}}{M} + \frac{2K}{M} \cos^2 \phi - \frac{i\omega\alpha}{|\gamma|} \right] - \left( \frac{\omega}{|\gamma|} \right)^2$$

The FMR measurements in chapter 5 measured the *Re* and *Im* components of  $\chi_{mn}$ , with the Gilbert damping being related to the line width of the *Im* component. The low temperature TR-MOKE setup used in chapter 5 measured predominately the component of the AC magnetic susceptibility  $\chi_{xy}$ , which has the form

$$\chi_{xy} = -\frac{1}{\Delta} \frac{i\omega}{|\gamma|} = -\frac{1}{|\Delta|^2} \frac{i\omega\Delta^*}{|\gamma|}$$

The *Im* component of  $\chi_{xy}$  is then given by

$$\text{Im}(\chi_{xy}) = -\frac{1}{|\Delta|^2} \frac{\omega \text{Re}(\Delta)}{|\gamma|}$$

This equation can then be used to gain further insight into the FMR data shown in chapter 5.

### Appendix 3: Equations for the AC magnetic susceptibility in the presence of spin pumping

This appendix shows the derivation of the equations for the AC magnetic susceptibility that were used to fit the spin pumping FMR data in chapter 6.

B. Heinrich, PRL **90**, 187601 (2003) considered a trilayer in which the two magnetic layers have different resonance fields by virtue of their different thicknesses and different associated magnetic anisotropy. They write a modified LLG equation (equation 3) that includes spin-pumping torques. To fit the spin pumping data in chapter 6 it was necessary to modify their equations so that they apply to the case where  $M_1$  and  $M_2$  are different materials. An additional term to account for the influence of dipolar coupling was also added. By denoting the two ferromagnetic layers 1 and 2, the equations of motion then become

$$\begin{aligned} \frac{\hat{\mathbf{a}}_1}{\hat{a}} &= -|\gamma_1|\mathbf{u}_1 \times \mathbf{H}_{eff,1} - \beta_1|\gamma_1|M_2\mathbf{u}_1 \times \mathbf{u}_2 + \alpha_1^{(0)}\mathbf{u}_1 \times \frac{\hat{\mathbf{a}}_1}{\hat{a}} + \alpha'_{11}\mathbf{u}_1 \times \frac{\hat{\mathbf{a}}_1}{\hat{a}} - \delta'_{11}\frac{\hat{\mathbf{a}}_1}{\hat{a}} - \alpha'_{12}\mathbf{u}_2 \times \frac{\hat{\mathbf{a}}_2}{\hat{a}} + \delta'_{12}\frac{\hat{\mathbf{a}}_2}{\hat{a}} \\ (1 + \delta'_{11})\frac{\hat{\mathbf{a}}_1}{\hat{a}} - \delta'_{12}\frac{\hat{\mathbf{a}}_2}{\hat{a}} &= -|\gamma_1|\mathbf{u}_1 \times \left\{ \mathbf{H}_{eff,1} + \beta_1M_2\mathbf{u}_2 - \frac{(\alpha_1^{(0)} + \alpha'_{11})}{|\gamma_1|}\frac{\hat{\mathbf{a}}_1}{\hat{a}} \right\} - \alpha'_{12}\mathbf{u}_2 \times \frac{\hat{\mathbf{a}}_2}{\hat{a}} \\ \frac{\hat{\mathbf{a}}_2}{\hat{a}} &= -|\gamma_2|\mathbf{u}_2 \times \mathbf{H}_{eff,2} - \beta_2|\gamma_2|M_1\mathbf{u}_2 \times \mathbf{u}_1 + \alpha_2^{(0)}\mathbf{u}_2 \times \frac{\hat{\mathbf{a}}_2}{\hat{a}} + \alpha'_{22}\mathbf{u}_2 \times \frac{\hat{\mathbf{a}}_2}{\hat{a}} - \delta'_{22}\frac{\hat{\mathbf{a}}_2}{\hat{a}} - \alpha'_{21}\mathbf{u}_1 \times \frac{\hat{\mathbf{a}}_1}{\hat{a}} + \delta'_{21}\frac{\hat{\mathbf{a}}_1}{\hat{a}} \\ (1 + \delta'_{22})\frac{\hat{\mathbf{a}}_2}{\hat{a}} - \delta'_{21}\frac{\hat{\mathbf{a}}_1}{\hat{a}} &= -|\gamma_2|\mathbf{u}_2 \times \left\{ \mathbf{H}_{eff,2} + \beta_2M_1\mathbf{u}_1 - \frac{(\alpha_2^{(0)} + \alpha'_{22})}{|\gamma_2|}\frac{\hat{\mathbf{a}}_2}{\hat{a}} \right\} - \alpha'_{21}\mathbf{u}_1 \times \frac{\hat{\mathbf{a}}_1}{\hat{a}} \end{aligned}$$

where  $\beta$  is a dipolar coupling coefficient,  $\alpha^{(0)}$  is the Gilbert damping, the  $\alpha'_{mn}$  terms are the spin pump ( $m = n$ ) and spin sink ( $m \neq n$ ) terms relating to the  $Re$  component of the spin mixing conductance. The  $\delta'_{mn}$  terms are related to the  $Im$  component of the spin mixing conductance. They are often negligible, but included for completeness. All other terms have their usual meaning. The coordinate system used for this derivation is the same as has been used throughout this thesis:  $z$  is in-plane and along the CPW symmetry axis,  $y$  is in-plane and transverse to the CPW symmetry axis,  $x$  is out-of-plane.

We wish to consider the case of small amplitude excitation when the external field is applied parallel to the easy axis (EA) which we assume is common to both layers.

Layer 1 is the free layer (FL) then layer 2 is the pinned layer (PL) and is subject to an exchange bias field, again parallel to the EA. It is assumed that the static magnetisations of both layers are parallel to the EA. Next we write down the free energy density for each layer (excluding interactions that are written as additional terms in the LLG equation).

$$\begin{aligned}
E_1 &= -(m_{x,1}\mathbf{i} + m_{y,1}\mathbf{j} + (M_1 + m_{z,1})\mathbf{k}) \cdot (h_x\mathbf{i} + h_y\mathbf{j} + (H + h_z)\mathbf{k}) \\
&\quad + \frac{1}{2} \left( D_{xx}m_{x,1}^2 + D_{yy}m_{y,1}^2 + D_{zz}(M_1 + m_{z,1})^2 \right) - \frac{K_1}{M_1^2} (M_1 + m_{z,1})^2 \\
E_2 &= -(m_{x,2}\mathbf{i} + m_{y,2}\mathbf{j} + (M_2 + m_{z,2})\mathbf{k}) \cdot (h_x\mathbf{i} + h_y\mathbf{j} + (H + H_{exb} + h_z)\mathbf{k}) \\
&\quad + \frac{1}{2} \left( D_{xx}m_{x,2}^2 + D_{yy}m_{y,2}^2 + D_{zz}(M_2 + m_{z,2})^2 \right) - \frac{K_2}{M_2^2} (M_2 + m_{z,2})^2
\end{aligned}$$

Where  $\mathbf{h}$  is the driving field,  $\mathbf{M}_i$  the magnetisation,  $\mathbf{K}_i$  the anisotropy constant of layer  $i$  and  $D$  is the demagnetising tensor in the thin film limit. The effective field of each layer is given by

$$\mathbf{H}_{eff,i} = -\frac{1}{M_i} \nabla_{\mathbf{u}_i} E_i$$

This then allows one to write

$$\mathbf{H}_{eff,1} = \mathbf{i}[h_x - D_{xx}M_1u_{x,1}] + \mathbf{j}[h_y - D_{yy}M_1u_{y,1}] + \mathbf{k}[(H + h_z) - D_{zz}M_1(1 + u_{z,1}) + 2K_1(1 + u_{z,1})]$$

$$\mathbf{H}_{eff,2} = \mathbf{i}[h_x - D_{xx}M_2u_{x,2}] + \mathbf{j}[h_y - D_{yy}M_2u_{y,2}] + \mathbf{k}[(H + H_{exb} + h_z) - D_{zz}M_2(1 + u_{z,2}) + 2K_2(1 + u_{z,2})]$$

$$\begin{aligned}
(1 + \delta'_{11})\frac{\hat{\mathbf{a}}_1}{\alpha} - \delta'_{12}\frac{\hat{\mathbf{a}}_2}{\alpha} &= -|\gamma_1|\mathbf{u}_1 \times \mathbf{H}_{eff,1} - \beta_1|\gamma_1|M_2\mathbf{u}_1 \times \mathbf{u}_2 + \alpha_1^{(0)}\mathbf{u}_1 \times \frac{\hat{\mathbf{a}}_1}{\alpha} + \left( \alpha'_{11}\mathbf{u}_1 \times \frac{\hat{\mathbf{a}}_1}{\alpha} - \alpha'_{12}\mathbf{u}_2 \times \frac{\hat{\mathbf{a}}_2}{\alpha} \right) \\
&= -|\gamma_1|\mathbf{u}_1 \times \left\{ \mathbf{H}_{eff,1} + \beta_1M_2\mathbf{u}_2 - \frac{(\alpha_1^{(0)} + \alpha'_{11})}{|\gamma_1|} \frac{\hat{\mathbf{a}}_1}{\alpha} \right\} - \alpha'_{12}\mathbf{u}_2 \times \frac{\hat{\mathbf{a}}_2}{\alpha}
\end{aligned}$$

$$\begin{aligned}
(1 + \delta'_{22})\frac{\hat{\mathbf{a}}_2}{\alpha} - \delta'_{21}\frac{\hat{\mathbf{a}}_1}{\alpha} &= -|\gamma_2|\mathbf{u}_2 \times \mathbf{H}_{eff,2} - \beta_2|\gamma_2|M_1\mathbf{u}_2 \times \mathbf{u}_1 + \alpha_2^{(0)}\mathbf{u}_2 \times \frac{\hat{\mathbf{a}}_2}{\alpha} + \left( \alpha'_{22}\mathbf{u}_2 \times \frac{\hat{\mathbf{a}}_2}{\alpha} - \alpha'_{21}\mathbf{u}_1 \times \frac{\hat{\mathbf{a}}_1}{\alpha} \right) \\
&= -|\gamma_2|\mathbf{u}_2 \times \left\{ \mathbf{H}_{eff,2} + \beta_2M_1\mathbf{u}_1 - \frac{(\alpha_2^{(0)} + \alpha'_{22})}{|\gamma_2|} \frac{\hat{\mathbf{a}}_2}{\alpha} \right\} - \alpha'_{21}\mathbf{u}_1 \times \frac{\hat{\mathbf{a}}_1}{\alpha}
\end{aligned}$$

$$\begin{aligned}
& (1 + \delta_{11})\dot{\mathbf{u}}_1 - \delta_{12}\dot{\mathbf{u}}_2 = \\
& \left( \begin{array}{l}
-|\gamma_1 \left[ u_{y,1} \left( H_{eff1,z} + \beta_1 M_2 (1 + u_{z,2}) - \frac{(\alpha_1^0 + \alpha_{11})}{|\gamma_1|} \dot{\mathbf{u}}_{z,1} \right) - (1 + u_{z,1}) \left( H_{eff1,y} + \beta_1 M_2 u_{y,2} - \frac{(\alpha_1^0 + \alpha_{11})}{|\gamma_1|} \dot{\mathbf{u}}_{y,1} \right) \right] \\
-\alpha'_{12} (u_{y,2} \dot{\mathbf{u}}_{z,2} - (1 + u_{z,2}) \dot{\mathbf{u}}_{y,2}) \\
-|\gamma_1 \left[ (1 + u_{z,1}) \left( H_{eff1,x} + \beta_1 M_2 u_{x,2} - \frac{(\alpha_1^0 + \alpha_{11})}{|\gamma_1|} \dot{\mathbf{u}}_{x,1} \right) - u_{x,1} \left( H_{eff1,z} + \beta_1 M_2 (1 + u_{z,2}) - \frac{(\alpha_1^0 + \alpha_{11})}{|\gamma_1|} \dot{\mathbf{u}}_{z,1} \right) \right] \\
-\alpha'_{12} ((1 + u_{z,2}) \dot{\mathbf{u}}_{x,2} - u_{x,2} \dot{\mathbf{u}}_{z,2}) \\
-|\gamma_1 \left[ u_{x,1} \left( H_{eff1,y} + \beta_1 M_2 u_{y,2} - \frac{(\alpha_1^0 + \alpha_{11})}{|\gamma_1|} \dot{\mathbf{u}}_{y,1} \right) - u_{y,1} \left( H_{eff1,x} + \beta_1 M_2 u_{x,2} - \frac{(\alpha_1^0 + \alpha_{11})}{|\gamma_1|} \dot{\mathbf{u}}_{x,1} \right) \right] \\
-\alpha'_{12} (u_{x,2} \dot{\mathbf{u}}_{y,2} - u_{y,2} \dot{\mathbf{u}}_{x,2})
\end{array} \right)
\end{aligned}$$

At this point we linearise the equations of motion by assuming that

$$u_x, u_y \ll 1, \quad 1 + u_z = \sqrt{1 - u_x^2 - u_y^2} \approx 1 - \frac{1}{2} (u_x^2 + u_y^2) \approx 1$$

and then only retain 1<sup>st</sup> order terms

$$\begin{aligned}
& \left( \begin{array}{l}
(1 + \delta_{11})\dot{\mathbf{u}}_{x,1} - \delta_{12}\dot{\mathbf{u}}_{x,2} \\
(1 + \delta_{11})\dot{\mathbf{u}}_{y,1} - \delta_{12}\dot{\mathbf{u}}_{y,2} \\
0
\end{array} \right) = \left( \begin{array}{l}
-|\gamma_1 \left[ u_{y,1} (H_{eff1,z} + \beta_1 M_2) - \left( H_{eff1,y} + \beta_1 M_2 u_{y,2} - \frac{(\alpha_1^0 + \alpha_{11})}{|\gamma_1|} \dot{\mathbf{u}}_{y,1} \right) \right] + \alpha'_{12} \dot{\mathbf{u}}_{y,2} \\
-|\gamma_1 \left[ \left( H_{eff1,x} + \beta_1 M_2 u_{x,2} - \frac{(\alpha_1^0 + \alpha_{11})}{|\gamma_1|} \dot{\mathbf{u}}_{x,1} \right) - u_{x,1} (H_{eff1,z} + \beta_1 M_2) \right] - \alpha'_{12} \dot{\mathbf{u}}_{x,2} \\
-|\gamma_1 [u_{x,1} H_{eff1,y} - u_{y,1} H_{eff1,x}]
\end{array} \right) \\
& = \left( \begin{array}{l}
-|\gamma_1 \left[ u_{y,1} (H - D_{zz} M_1 + 2K_1 + \beta_1 M_2) - \left( h_y - D_{yy} M_1 u_{y,1} + \beta_1 M_2 u_{y,2} - \frac{(\alpha_1^0 + \alpha_{11})}{|\gamma_1|} \dot{\mathbf{u}}_{y,1} \right) \right] + \alpha'_{12} \dot{\mathbf{u}}_{y,2} \\
-|\gamma_1 \left[ \left( h_x - D_{xx} M_1 u_{x,1} + \beta_1 M_2 u_{x,2} - \frac{(\alpha_1^0 + \alpha_{11})}{|\gamma_1|} \dot{\mathbf{u}}_{x,1} \right) - u_{x,1} (H - D_{zz} M_1 + 2K_1 + \beta_1 M_2) \right] - \alpha'_{12} \dot{\mathbf{u}}_{x,2} \\
-|\gamma_1 [u_{x,1} (h_y - D_{yy} M_1 u_{y,1}) - u_{y,1} (h_x - D_{xx} M_1 u_{x,1})]
\end{array} \right)
\end{aligned}$$

$$(1 + \delta_{22}) \dot{\mathbf{u}}_2 - \delta_{21} \dot{\mathbf{u}}_1 = \left[ \begin{array}{l} -|\gamma_2 \left[ u_{y,2} (H + H_{exb} - D_{zz} M_2 + 2K_2 + \beta_2 M_1) - \left( h_y - D_{yy} M_2 u_{y,2} + \beta_2 M_1 u_{y,1} - \frac{(\alpha_2^0 + \alpha'_{22})}{|\gamma_2|} \dot{\mathbf{u}}_{y,2} \right) \right] \right. \\ \left. + \alpha'_{21} \dot{\mathbf{u}}_{y,1} \right. \\ -|\gamma_2 \left[ h_x - D_{xx} M_2 u_{x,2} + \beta_2 M_1 u_{x,1} - \frac{(\alpha_2^0 + \alpha'_{22})}{|\gamma_2|} \dot{\mathbf{u}}_{x,2} \right] - u_{x,2} (H + H_{exb} - D_{zz} M_2 + 2K_2 + \beta_2 M_1) \\ \left. - \alpha'_{21} \dot{\mathbf{u}}_{x,1} \right. \\ \left. -|\gamma_2 \left[ u_{x,2} (h_y - D_{yy} M_2 u_{y,2}) - u_{y,2} (h_x - D_{xx} M_2 u_{x,2}) \right] \right] \end{array} \right]$$

This then gives us 4 simultaneous equations of the form

$$\begin{aligned} \frac{(1 + \delta_{11})}{|\gamma_1|} \dot{\mathbf{u}}_{x,1} - \frac{\delta_{12}}{|\gamma_1|} \dot{\mathbf{u}}_{x,2} - \frac{\alpha'_{12}}{|\gamma_1|} \dot{\mathbf{u}}_{y,2} + (H + (D_{yy} - D_{zz}) M_1 + 2K_1 + \beta_1 M_2) u_{y,1} + \frac{(\alpha_1^0 + \alpha'_{11})}{|\gamma_1|} \dot{\mathbf{u}}_{y,1} \\ - \beta_1 M_2 u_{y,2} = h_y \\ - \frac{(\alpha_1^0 + \alpha'_{11})}{|\gamma_1|} \dot{\mathbf{u}}_{x,1} + \frac{(1 + \delta_{11})}{|\gamma_1|} \dot{\mathbf{u}}_{y,1} - \frac{\delta_{12}}{|\gamma_1|} \dot{\mathbf{u}}_{y,2} + \frac{\alpha'_{12}}{|\gamma_1|} \dot{\mathbf{u}}_{x,2} - (H + (D_{xx} - D_{zz}) M_1 + 2K_1 + \beta_1 M_2) u_{x,1} \\ + \beta_1 M_2 u_{x,2} = -h_x \\ \frac{(1 + \delta_{22})}{|\gamma_2|} \dot{\mathbf{u}}_{x,2} - \frac{\delta_{21}}{|\gamma_2|} \dot{\mathbf{u}}_{x,1} - \frac{\alpha'_{21}}{|\gamma_2|} \dot{\mathbf{u}}_{y,1} + (H + H_{exb} + (D_{yy} - D_{zz}) M_2 + 2K_2 + \beta_2 M_1) u_{y,2} + \frac{(\alpha_2^0 + \alpha'_{22})}{|\gamma_2|} \dot{\mathbf{u}}_{y,2} \\ - \beta_2 M_1 u_{y,1} = h_y \\ - \frac{(\alpha_2^0 + \alpha'_{22})}{|\gamma_2|} \dot{\mathbf{u}}_{x,2} + \frac{(1 + \delta_{22})}{|\gamma_2|} \dot{\mathbf{u}}_{y,2} - \frac{\delta_{21}}{|\gamma_2|} \dot{\mathbf{u}}_{y,1} + \frac{\alpha'_{21}}{|\gamma_2|} \dot{\mathbf{u}}_{x,1} - u_{x,2} (H + H_{exb} + (D_{xx} - D_{zz}) M_2 + 2K_2 + \beta_2 M_1) \\ + \beta_2 M_1 u_{x,1} = -h_x \end{aligned}$$

We then look for harmonic solutions to the above equations, of the form

$$h_x = h_{x0} \exp(-i\alpha t), \quad h_y = h_{y0} \exp(-i\alpha t), \quad u_{x,i} = u_{x0,i} \exp(-i\alpha t), \quad u_{y,i} = u_{y0,i} \exp(-i\alpha t)$$

$$\begin{aligned}
& \frac{-i\omega}{|\gamma_1|}(1+\delta_{11})u_{x0,1} + \frac{i\omega}{|\gamma_1|}\delta_{12}u_{x0,2} + \left( H + (D_{yy} - D_{zz})M_1 + 2K_1 + \beta_1M_2 - \frac{i\omega(\alpha_1^0 + \alpha'_{11})}{|\gamma_1|} \right) u_{y0,1} \\
& + \left( \frac{i\omega\alpha'_{12}}{|\gamma_1|} - \beta_1M_2 \right) u_{y0,2} = h_{y0} \\
& - \left( H + (D_{xx} - D_{zz})M_1 + 2K_1 + \beta_1M_2 - \frac{i\omega(\alpha_1^0 + \alpha'_{11})}{|\gamma_1|} \right) u_{x0,1} - \frac{i\omega}{|\gamma_1|}(1+\delta_{11})u_{y0,1} - \left( \frac{i\omega\alpha'_{12}}{|\gamma_1|} - \beta_1M_2 \right) u_{x0,2} \\
& + \frac{i\omega}{|\gamma_1|}\delta_{12}u_{y0,2} = -h_{x0} \\
& \left( \frac{i\omega\alpha'_{21}}{|\gamma_2|} - \beta_2M_1 \right) u_{y0,1} - \frac{i\omega}{|\gamma_2|}(1+\delta_{22})u_{x0,2} + \frac{i\omega}{|\gamma_2|}\delta_{21}u_{x0,1} \\
& + \left( H + H_{exb} + (D_{yy} - D_{zz})M_2 + 2K_2 + \beta_2M_1 - \frac{i\omega(\alpha_2^0 + \alpha'_{22})}{|\gamma_2|} \right) u_{y0,2} = h_{y0} \\
& - \left( \frac{i\omega\alpha'_{21}}{|\gamma_2|} - \beta_2M_1 \right) u_{x0,1} - \left( H + H_{exb} + (D_{xx} - D_{zz})M_2 + 2K_2 + \beta_2M_1 - \frac{i\omega(\alpha_2^0 + \alpha'_{22})}{|\gamma_2|} \right) u_{x0,2} \\
& - \frac{i\omega}{|\gamma_2|}(1+\delta_{22})u_{y0,2} + \frac{i\omega}{|\gamma_2|}\delta_{21}u_{y0,1} = -h_{x0}
\end{aligned}$$

We then rewrite the above as a matrix equation of the form

$$A \begin{pmatrix} u_{x0,1} \\ u_{y0,1} \\ u_{x0,2} \\ u_{y0,2} \end{pmatrix} = \begin{pmatrix} h_{y0} \\ -h_{x0} \\ h_{y0} \\ -h_{x0} \end{pmatrix}$$

$$A = \begin{pmatrix} \frac{-i\omega}{|\gamma_1|}(1+\delta_{11}), & H + (D_{yy} - D_{zz})M_1 + 2K_1 + \beta_1M_2 - \frac{i\omega(\alpha_1^0 + \alpha'_{11})}{|\gamma_1|}, & \frac{i\omega}{|\gamma_1|}\delta_{12}, & \frac{i\omega\alpha'_{12}}{|\gamma_1|} - \beta_1M_2 \\ - \left( H + (D_{xx} - D_{zz})M_1 + 2K_1 + \beta_1M_2 - \frac{i\omega(\alpha_1^0 + \alpha'_{11})}{|\gamma_1|} \right), & - \frac{i\omega}{|\gamma_1|}(1+\delta_{11}), & - \left( \frac{i\omega\alpha'_{12}}{|\gamma_1|} - \beta_1M_2 \right), & \frac{i\omega}{|\gamma_1|}\delta_{12} \\ \frac{i\omega}{|\gamma_2|}\delta_{21}, & \frac{i\omega\alpha'_{21}}{|\gamma_2|} - \beta_2M_1, & - \frac{i\omega}{|\gamma_2|}(1+\delta_{22}), & H + H_{exb} + (D_{yy} - D_{zz})M_2 + 2K_2 + \beta_2M_1 - \frac{i\omega(\alpha_2^0 + \alpha'_{22})}{|\gamma_2|} \\ - \left( \frac{i\omega\alpha'_{21}}{|\gamma_2|} - \beta_2M_1 \right), & \frac{i\omega}{|\gamma_2|}\delta_{21}, & - \left( H + H_{exb} + (D_{xx} - D_{zz})M_2 + 2K_2 + \beta_2M_1 - \frac{i\omega(\alpha_2^0 + \alpha'_{22})}{|\gamma_2|} \right), & - \frac{i\omega}{|\gamma_2|}(1+\delta_{22}) \end{pmatrix}$$

$$A = \begin{pmatrix} \frac{-i\omega}{|\gamma_1|}(1+\delta_{11}) & H_{a1} & \frac{i\omega}{|\gamma_1|}\delta_{12} & H_{c1} \\ -H_{b1} & \frac{-i\omega}{|\gamma_1|}(1+\delta_{11}) & -H_{d1} & \frac{i\omega}{|\gamma_1|}\delta_{12} \\ \frac{i\omega}{|\gamma_2|}\delta_{21} & H_{c2} & \frac{-i\omega}{|\gamma_2|}(1+\delta_{22}) & H_{a2} \\ -H_{d2} & \frac{i\omega}{|\gamma_2|}\delta_{21} & -H_{b2} & \frac{-i\omega}{|\gamma_2|}(1+\delta_{22}) \end{pmatrix}$$

$$H_{a1} = H + (D_{yy} - D_{zz})M_1 + 2K_1/M_1 + \beta_1 M_2 - \frac{i\omega(\alpha_1^0 + \alpha_{11})}{|\gamma_1|} \quad H_{c1} = \frac{i\omega\alpha'_{12}}{|\gamma_1|} - \beta_1 M_2$$

$$H_{b1} = H + (D_{xx} - D_{zz})M_1 + 2K_1/M_1 + \beta_1 M_2 - \frac{i\omega(\alpha_1^0 + \alpha_{11})}{|\gamma_1|} \quad H_{d1} = \frac{i\omega\alpha'_{12}}{|\gamma_1|} - \beta_1 M_2$$

$$H_{a2} = H + H_{exb} + (D_{yy} - D_{zz})M_2 + 2K_2/M_2 + \beta_2 M_1 - \frac{i\omega(\alpha_2^0 + \alpha_{22})}{|\gamma_2|} \quad H_{c2} = \frac{i\omega\alpha'_{21}}{|\gamma_2|} - \beta_2 M_1$$

$$H_{b2} = H + H_{exb} + (D_{xx} - D_{zz})M_2 + 2K_2/M_2 + \beta_2 M_1 - \frac{i\omega(\alpha_2^0 + \alpha_{22})}{|\gamma_2|} \quad H_{d2} = \frac{i\omega\alpha'_{22}}{|\gamma_2|} - \beta_2 M_1$$

$$\begin{pmatrix} u_{x0,1} \\ u_{y0,1} \\ u_{x0,2} \\ u_{y0,2} \end{pmatrix} = A^{-1} \begin{pmatrix} h_{y0} \\ -h_{x0} \\ h_{y0} \\ -h_{x0} \end{pmatrix}$$

$$\begin{aligned} u_{x0,1} &= (A_{11}^{-1} + A_{13}^{-1})h_{y0} - (A_{12}^{-1} + A_{14}^{-1})h_{x0} \\ u_{y0,1} &= (A_{21}^{-1} + A_{23}^{-1})h_{y0} - (A_{22}^{-1} + A_{24}^{-1})h_{x0} \\ u_{x0,2} &= (A_{31}^{-1} + A_{33}^{-1})h_{y0} - (A_{32}^{-1} + A_{34}^{-1})h_{x0} \\ u_{y0,2} &= (A_{41}^{-1} + A_{43}^{-1})h_{y0} - (A_{42}^{-1} + A_{44}^{-1})h_{x0} \end{aligned}$$

This finally allows us to write

$$\begin{aligned} \chi_{xx}^{(1)} &= m_{x0,1}/h_{x0} = -M_1 (A_{12}^{-1} + A_{14}^{-1}) & \chi_{xx}^{(2)} &= m_{x0,2}/h_{x0} = -M_2 (A_{32}^{-1} + A_{34}^{-1}) \\ \chi_{xy}^{(1)} &= m_{x0,1}/h_{y0} = M_1 (A_{11}^{-1} + A_{13}^{-1}) & \chi_{xy}^{(2)} &= m_{x0,2}/h_{y0} = M_2 (A_{31}^{-1} + A_{33}^{-1}) \\ \chi_{yx}^{(1)} &= m_{y0,1}/h_{x0} = -M_1 (A_{22}^{-1} + A_{24}^{-1}) & \chi_{yx}^{(2)} &= m_{y0,2}/h_{x0} = -M_2 (A_{42}^{-1} + A_{44}^{-1}) \\ \chi_{yy}^{(1)} &= m_{y0,1}/h_{y0} = M_1 (A_{21}^{-1} + A_{23}^{-1}) & \chi_{yy}^{(2)} &= m_{y0,2}/h_{y0} = M_2 (A_{41}^{-1} + A_{43}^{-1}) \end{aligned}$$

Hence it is possible to calculate components of the AC magnetic susceptibility tensor by calculating components of the inverse matrix. This was done numerically in Matlab.

## Bibliography

- <sup>1</sup> P. Langevin, “Magnétisme et Théorie de Électrons” Ann. Chim. Phys. **5**, 70 (1905).
- <sup>2</sup> P. Weiss, “L’Hypothèse du Cham Moléculaire et la Propriété Ferromagnétique”, J. de Phys. Rad. **6**, 661 (1907).
- <sup>3</sup> W. Heisenberg, “Zur Theorie des Ferromagnetismus”, Z. Phys. **49**, 619 (1928).
- <sup>4</sup> L.D. Landau and E.M. Lifshitz, “On the Theory of the Dispersion of Magnetic Permeability in Ferromagnetic Bodies”, Phys. Zs. der Sowjetunion. **8**, 153 (1935).
- <sup>5</sup> A. Aharoni, *Introduction to the Theory of Ferromagnetism*, Oxford University Press (2000).
- <sup>6</sup> A.H. Morrish, *The Physical Principles of Magnetism*, John Wiley & Sons (1965).
- <sup>7</sup> D.L. Mills, “Thermodynamic Properties of Ultrathin Magnetic Structures”, in *Ultrathin Magnetic Structures I*, Edited by B. Heinrich and J.A.C. Bland, Springer-Verlag, Berlin, 1994.
- <sup>8</sup> A. Hubert, R. Schaefer, *Magnetic Domains* (Springer, Berlin Heidelberg New York 1998).
- <sup>9</sup> G. Bertotti, *Hysteresis in Magnetism*, Academic Press, San Diego, 1998.
- <sup>10</sup> J.H. van Vleck, Rev. Mod. Phys. **17**,27 (1945).
- <sup>11</sup> J. H. Van Vleck, Phys. Rev. **52**, 1178 (1938)
- <sup>12</sup> U. Gradmann, J. Apply. Phys. **40**, 1182 (1969).
- <sup>13</sup> B. D. Cullity, *Introduction to Magnetic Materials* (Addison-Wesley, Reading, 1972).
- <sup>14</sup> V. V. Kruglyak PhD Thesis, University of Exeter (2004).
- <sup>15</sup> M. D. Stiles, R. D. McMichael, Phys. Rev. B **59**, 3622 (1999).
- <sup>16</sup> T.L. Gilbert, Phys. Rev. **100**, 1243 (1955).
- <sup>17</sup> J. C. Slonczewski, J. Magn. Magn. Mater. **159**, L1 (1996).
- <sup>18</sup> L. Berger, Phys. Rev. B **54**, 9353 (1996)
- <sup>19</sup> Prim Gangmei, PhD Thesis, University of Exeter (2012).
- <sup>20</sup> Y. Tserkovnyak, A. Brataas, and G. E. W. Bauer, Phys. Rev. Lett. **88**, 117601 (2002).

- <sup>21</sup> R.W. Damon and J.R. Eshbach, “Magnetostatic Modes of a Ferromagnetic Slab”, *J. Phys. Chem. Solids* **19**, 308 (1961).
- <sup>22</sup> S.O. Demokritov, B. Hillebrands, and A.N. Slavin, *Phys. Rep.* **348**, 442 (2001)
- <sup>23</sup> Charles Kittel, *Phys. Rev.* **73**, 155 (1948).
- <sup>24</sup> C. Kittel, *Introduction to Solid State Physics*, 5th ed., John Wiley & Sons (1976).
- <sup>25</sup> M. K. Marcham, P. S. Keatley, A. Neudert, R. J. Hicken, S. A. Cavill, L. R. Shelford, G. van der Laan, N. D. Telling, J. R. Childress, J. A. Katine, P. Shafer, and E. Arenholz, *J. Appl. Phys.* **109**, 07D353 (2011).
- <sup>26</sup> G. Schütz, W. Wagner, W. Wilhelm, P. Kienle, R. Zeller, R. Frahm, and G. Materlik, *Phys. Rev. Lett.* **58**, 737 (1987)
- <sup>27</sup> W. Kuch (edited by H. Hopster, H. P. Oepen), *Magnetic Microscopy of Nanostructures* (Springer-Verlag, Berlin Heidelberg, 2005).
- <sup>28</sup> U. Fano, *Phys. Rev. A* **178**, 131 (1969).
- <sup>29</sup> H. Ebert, *Rep. Prog. Phys.* **59**, 1665 (1996).
- <sup>30</sup> Y. U. Idzerda, C. T. Chen, H. -J. Lin, H. Tjeng, and G. Meigs, *Physica B* **208-209**, 746 (1995).
- <sup>31</sup> J. Stöhr and R. Nakajima, *IBM J. Res. Develop.* **42**, 73 (1998).
- <sup>32</sup> J. Wu, J.R. Moore, and R.J. Hicken, “Optical Pump-Probe Studies of the Rise and Damping of Ferromagnetic Resonance Oscillations in a Thin Fe Film”, *J. Magn. Magn. Mater.* **222**, 189 (2000).
- <sup>33</sup> A. Stankiewicz, W. K. Hiebert, G. E. Ballentine, K. W. Marsh, and M. R. Freeman, *IEEE Trans. Magn.* **134**, 1003 (1998).
- <sup>34</sup> M. R. Freeman, W. K. Hiebert, and A. Stankiewicz, *J. Appl. Phys.* **83**, 6217 (1998).
- <sup>35</sup> M. G. Pini, P. Politim A. Rettorim G. Carlotti, G. Gubbiotti, M. Madami, and S. Taacchi, *Phys. Rev. B* **70**, 094422 (2004).
- <sup>36</sup> M. Madami, S. Taacchi, G. Carlotti, G. Gubbiottim and R. L. Stamps, *Phys. Rev. B* **69**, 144408 (2004).
- <sup>37</sup> Y. Guan, W. E. Bailey, E. Vescovo, C.-C. Kao and D. A. Arena, *J. Magn. Magn. Mater.* **312** 374 (2007)
- <sup>38</sup> D. A. Arena, E. Vescovo, C.-C. Kao, Y. Guan, and W. E. Bailey, *Phys. Rev. B* **74**, 064409 (2006).
- <sup>39</sup> T. Martin, G. Woltersdorf, C. Stamm, H. A. Dürr, R. Maththeis, C. H. Back and G. Bayreuther, *J. Appl. Phys.* **105**, 07D310 (2009).

- <sup>40</sup> J. Goulon, A. Rogalev, F. Wilhelm, N. Jaouen, C. Goulon-Ginet, G. Goujon, J. Ben Youssef and M. V. Indendom JETP Lett. **82**, 696 (2005).
- <sup>41</sup> G. Boero, S. Rusponi, P. Bencok, R. S. Popovic, H. Brune, and P. Gambardella, Appl. Phys. Lett. **87**, 152503 (2005).
- <sup>42</sup> G. Boero, S. Mouaziz, S. Rusponi, P. Bencok, F. Nolting, S. Stepanow, and P. Gambardella, New J. Phys. **10**, 013011 (2008).
- <sup>43</sup> W. E. Bailey, L. Cheng, D. J. Keavney, C.-C. Kao, E. Vescovo, and D. A. Arena, Phys. Rev. B **70**, 172403 (2004).
- <sup>44</sup> I. Neudecker, G. Woltersdorf, B. Heinrich, T. Okuno, G. Gubbiotti, and C. H. Back, J. Magn. Magn. Mater. **307**, 148 (2006).
- <sup>45</sup> C. M. Schneider, A. Krasnyuk, A. Oelsner, D. Neeb, S. A. Nepijko, G. Schonehense, I. Monch, R. Kaltofen, J. Morais, C. De Nadai, and N. B. Brookes, Appl. Phys. Lett. **85**, 2562 (2004).
- <sup>46</sup> S.-B. Choe, Y. Acremann, A. Scholl, A. Bauer, A. Doran, J. Stohr, and H. A. Padmore, Science **304**, 420 (2003).
- <sup>47</sup> Paul Keatley PhD thesis, University of Exeter (2008).
- <sup>48</sup> J. Stohr, and H. C. Siegmann, *Magnetism From Fundamentals to Nanoscale Dynamics* (Springer, Berlin, 2006).
- <sup>49</sup> H. Wende, Rep. Prog. Phys. **67** (2004) 2105-2181
- <sup>50</sup> C. T. Cehn, Y. U. Idzerda, H. -J. Lin, N. V. Smith, G. Meigs, E. Chaban, G. H. Ho, E. Pellegrin, and F. Sette, Phys. Rev. Lett **75**, 152 (1995).
- <sup>51</sup> E. Beaurepaire, H. Bulou, F. Scheurer, J. P. Kappler, *Magnetism: A Synchrotron Radiation Approach* (Springer, Berlin, 2006).
- <sup>52</sup> D. M. Poznar, *Microwave Engineering* (Wiley, 2004).
- <sup>53</sup> S. Maat, N. Smith, M. J. Carey, and J. R. Childress, Appl. Phys. Lett. **93**, 103506 (2008).
- <sup>54</sup> W. Bailey, P. Kabos, F. Mancoff, and S. Russek, IEEE Trans. Magn. **37**, 1749 (2001).
- <sup>55</sup> S. G. Reidy, L. Cheng and W. E. Bailey, Appl. Phys. Lett. **82**, 1254 (2003).
- <sup>56</sup> A. Neudert, P. S. Keatley, V. V. Kruglyak, J. McCord and R. J. Hicken, IEEE, Trans. Mag. **44**, 3083 (2008).
- <sup>57</sup> E. Arenholz, and S. O. Prestemon, Rev. Sci. Instrum. **76**, 083908 (2005).
- <sup>58</sup> The IRM Quaterly, Fall 2000, Vol. **10**, No. 3, Institue of Rock Magnetism
- <sup>59</sup> C. T. Chen, N. V. Smith, and F. Sette, Phys. Rev. B **43**, 6785 (1991).

- <sup>60</sup> C. De Nadai, A. Mirone, S. S. Dhesi, P. Bencecock, N. B. Brookes, I. Marenne, P. Rudolf, N. Tagmatarchis, H. Shinohara, and T. J. S. Dennis, *Phys. Rev. B.* **69** 184421 (2004).
- <sup>61</sup> G. N. Iles, C. Binns, S. H. Baker, and M. Roy, *JMMM*, **322** 2509-2515 (2010).
- <sup>62</sup> E. B. Myers, D. C. Ralph, J. A. Katine, R. N. Louie, and R. A. Burnham, *Science* **285**, 867 (1999).
- <sup>63</sup> C. H. Back, R. Allenspach, W. Weber, S. S. P. Parkin, D. Weller, E. L. Garwin, and H. C. Siegmann, *Science* **285**, 864 (1999).
- <sup>64</sup> J.-E. Wegrowe, *Phys. Rev. B* **62**, 1067 (2000).
- <sup>65</sup> R. H. Silsbee, A. Janossy, and P. Monod, *Phys. Rev. B* **19** 4382 (1979).
- <sup>66</sup> B. Heinrich, Y. Tserkovnyak, G. Woltersdorf, A. Brataas, R. Urban, and G. E. W. Bauer, *Phys. Rev. Lett.* **90**, 187601 (2003).
- <sup>67</sup> G. Woltersdorf, O. Mosendz, B. Heinrich, and C. H. Back, *Phys. Rev. Lett.* **99**, 246603 (2007).
- <sup>68</sup> B. Kardasz, and B. Heinrich, *Phys. Rev. B.* **81**, 094409 (2010)
- <sup>69</sup> F. J. Jedema, A. T. Filip, and B. J. Van Wees, *Nature* **410**, 345 (2001).
- <sup>70</sup> B. Kardasz, O. Mosendz, B. Heinrich, Z. Liu, and M. Freeman, *J. Appl. Phys.* **103**, 07C509 (2008).
- <sup>71</sup> Y. Tserkovnyak, A. Brataas, G. E. W. Bauer, and B. I. Halperin, *Rev. Mod. Phys.* **77**, 1375 (2005).
- <sup>72</sup> T. L. Monchesky, A. Enders, R. Urban, K. Myrtle, B. Heinrich, X.-G. Zhang, W. H. Butler, and J. Kirschner, *Phys. Rev. B* **71**, 214440 (2005).
- <sup>73</sup> S. S. Kalarickal, P. Krivosik, M. Wu, C. E. Patton, M. L. Schneider, P. Kabos, T. J. Silva, and J. P. Nibarger, *J. Appl. Phys.* **99**, 093909 (2006). K. Kobayashi, N. Inaba, N. Fujita, Y. Sudo, T. Tanaka, M. Ohtake, M. Futamoto, and F. Kirino *IEEE. Trans. Mag.* **45**, 9464 (2009). P. S. Keatley, V. V. Kruglyak, P. Gangmei, and R. J. Hicken, *Phil. Trans. R. Soc.* **369**, 1948 (2011).
- <sup>74</sup> M. C. Weber, H. Nembach, B. Hillebrands, and J. Fassbender, *J. Appl. Phys.* **97**, 10A701, (2005).
- <sup>75</sup> T. Yoshino, K. Ando, K. Harii, H. Nakayama, Y. Kajiwara, and E. Saitoh, *J. Phys.: Conf. Ser.* **266**, 012115 (2011).
- <sup>76</sup> B. Heinrich, C. Burrowes, E. Montoya, B. Kardasz, E. Grit, Young-Yeal Song, Yiyan Sun, and Mingzhong Wu, *Phys. Rev. Lett.* **107**, 066604 (2011).

- <sup>77</sup> N. W. Ashcroft, and N. D. Mermin, *Solid State Physics* (Holt, Rinehart and Winston, Philadelphia, 1976).
- <sup>78</sup> J. Stohr, W. Yu, M. G. Samant, B. B. Hermsmeier, G. Harp, S. Koranda, D. Dunham and B. P. Tonner, *Science* **259**, 658 (1993).
- <sup>79</sup> W. Kuch, R. Fromter, J. Giles, D. Hartmann, Ch. Ziethen, C. M. Schneider, G. Schonhense, W. Swiech and J. Kirschner, *Surf. Rev. Lett.* **5**, 1241 (1998).
- <sup>80</sup> C. M. Schneider, K. Holldack, M. Kinzler, M. Grunze, H. P. Oepen, F. Schafers, H. Petersen, K. Meinel and J. Kirschner, *Appl. Phys. Lett.* **63**, 2432 (1993).
- <sup>81</sup> A. Dussaux, B. Georges, J. Grollier, V. Cros, A. V. Khvalkovisky, A. Fukushima, M. Konoto, H. Kubota, K. Yakushiji, S. Yuasa, K. A. Zvezdin, K. Ando and A. Fert, *Nature. Comms.* **1**, 8, (2010).
- <sup>82</sup> M. Weigand, B. Van Waeyenberge, A. Vansteenkiste, M. Curcic, V. Sackmann, H. Stoll, T. Tylizszczak, K. Kaznatcheev, D. Bertwistle, G. Woltersdorf, C. H. Back and G. Schutz, *Phys. Rev. Lett.* **102**, 7, (2009).
- <sup>83</sup> H. Hopster, H. P. Oepen, *Magnetic Microscopy of Nanostructures* (Springer, Berlin, 2005).
- <sup>84</sup> D. D. Awschalom, J.-M. Halbout, S. Von Molnar, T. Siegrist and F. Holtzberg, *Phys. Rev. Lett.* **55**, 1128 (1985).
- <sup>85</sup> A. Locatelli and E. Bauer, *J. Phys.: Condens. Matter* **20**, 093002 (2008).
- <sup>86</sup> R. Nakajima, J. Stohr and Y. U. Idzerda, *Phys. Rev. B* **59**, 6421 (1999).
- <sup>87</sup> S. Anders, H. A. Padmore, R. M. Duarte, T. Renner, Th. Stammner, A. Scholl, M. R. Scheinfein, J. Stohr, L. Seve and B. Sinkovic, *Rev. Sci. Instrum.* **70**, 3973 (1999).
- <sup>88</sup> B. Van Waeyenberge, A. Puzic, H. Stoll, K. W. Chou, T. Tylizszczak, R. Hertel, M. Fahnle, H. Bruckl, K. Rott, G. Reiss, I. Neudecker, D. Weiss, C. H. Back and G. Schutz, *Nature* **444**, 05240, (2006).
- <sup>89</sup> A. Vansteenkiste, K. W. Chou, M. Weigand, M. Curic, V. Sackmann, H. Stoll, T. Tylizszczak, G. Woltersdorf, C. H. Back, G. Schutz and B. Van Waeyenberge, *Nature Physics*, **5**, 1231, (2009).
- <sup>90</sup> A. Vansteenkiste, J. De Baerdemaeker, K. W. Chou, H. Stoll, M. Curcic, T. Tylizszczak, G. Woltersdorf, C. H. Back, G. Schutz and B. Van Waeyenberge, *Phys. Rev. B.* **77**, 144420, (2008).
- <sup>91</sup> I. E. Collier, *X-ray-induced Luminescence in Sapphire and Ruby* (Bowling Green, Ky, 1970).
- <sup>92</sup> K. H. Lee, and J. H. Crawford, Jr. *Journal of Luminescence* **20** (1979) 9-15.
- <sup>93</sup> J. Wu, J. S. Park, W. Kim, E. Arenholz, M. Liberati, A. Scholl, Y. Z. Wu, Chanyong Hwang, and Z. Q. Qiu *Phys. Rev. Lett.* **104**, 217204 (2010).

